

QUANTITATIVE PREDICTION OF ELASTIC AND
ANELASTIC PHENOMENA ON THE NANOMETER
SCALE

A Dissertation

Presented to the Faculty of the Graduate School

of Cornell University

in Partial Fulfillment of the Requirements for the Degree of

Doctor of Philosophy

by

Hande Üstünel

January 2006

© 2006 Hande Üstünel
ALL RIGHTS RESERVED

QUANTITATIVE PREDICTION OF ELASTIC AND ANELASTIC
PHENOMENA ON THE NANOMETER SCALE

Hande Üstünel, Ph.D.

Cornell University 2006

In the past two decades, nanometer scale devices have become increasingly important in various scientific and technological applications such as sensors, actuators and storage devices. This thesis presents a theoretical exploration of some of the vibrational properties of such devices, with an emphasis on *quality factor*, the fraction of energy lost per period of oscillation in a vibrating system.

The thesis introduces a new method for obtaining the ground state structure of defects by looking at their mechanical response. This method involves calculation of the *activation volume tensor* of the defect using reliable *ab initio* techniques. As an application, results are presented for the activation volume tensor Λ of a *divacancy* in silicon, a defect commonly introduced in the fabrication stages of silicon actuators. Comparison of the activation volume tensor to experimental values leads to an unambiguous identification of the ground state of this defect, which has proved elusive in the literature to date. Finally, the calculation of the mechanical energy loss caused by divacancies in a silicon oscillator is given.

The thesis then turns to the calculation of the electronic mean-free path in carbon nanotubes under high-bias. Electron-phonon interactions have been found to have a considerable effect in the determination of the electron mean-free path. We determine the mean-free path of the nanotubes in the presence of various phonon

modes that cause scattering of electrons. The thesis concludes with a consideration of the vibrations of suspended nanotubes, exploring first the dependence of the vibration frequencies on such factors as downward force and built-in slack in the nanotube and then turning to a fundamental loss mechanism intrinsic to any system, namely loss due to phonon-phonon interactions.

BIOGRAPHICAL SKETCH

The author was born in Ankara, Turkey in 1977. After obtaining her Bachelor of Science degree in Physics from Orta Doğu Teknik Üniversitesi (Middle East Technical University) in Ankara in 1999, she started her PhD degree at Cornell University. She joined the group of Professor Tomás Arias in the summer of 2000, where she conducted research in theoretical condensed matter until graduation.

Anneme ve babama

To my parents

ACKNOWLEDGEMENTS

First and foremost, I would like to express my endless thanks and gratitude to my parents, Nilgün and Altan Üstünel for undertaking the very difficult task of letting their only child go so far away from them for so long. Without their love, patience and limitless support in all I undertook, none of what I have achieved would have been even remotely possible.

I have also much to thank for to my advisor, Professor Tomás Arias. Even in the beginning when I just barely knew how to type, he was infinitely patient and encouraging without ever making me feel inadequate. In the later years, he provided me with guidance when I needed it at the same time letting me explore and learn by myself. He has witnessed and shaped my development as a scientist-in-training and I am much grateful to him for all he has done for me. It is through his guidance, his enthusiasm for science and talent for picking and assigning the right project that this thesis has been possible.

During the last two years, I have been fortunate enough to have a brilliant second mentor, from whom I've learnt a great deal. Among many other things, I would like to thank David Roundy for having an almost impossible amount of patience, for being always (and I mean always) ready to help, for listening to me when I've had my moments of concern about many different issues, for sharing with me his insightful views about research, for being so completely selfless, and for being a good friend.

I would also like to thank Professor Paul McEuen and Professor Piet Brouwer for serving on my committee, all the collaboration and many useful discussions throughout my time at Cornell. I would like to thank Dr Cyrus Umrigar, whom, even though I haven't interacted academically with, I have been very fortunate to

know and be inspired by.

I acknowledge and thank my collaborators in many projects, Stephan Braig, Vera Sazonova, Lidija Sekaric, Arend van der Zande and Yuval Yaish.

I cannot pass without mentioning my teachers back home in Turkey who have all taken a large part in shaping my career. This thesis is also unofficially dedicated to the memory of Professor Ordal Demokan, who was not only my first Physics professor in METU but a great scientist and teacher. His untimely loss has affected me deeply and he is greatly missed. I would also like to give my many thanks to Professor Sinan Bilikmen for encouraging me constantly starting from before I entered the Physics department in METU all the way up till now. For the same reasons, I would like to thank Professor Şakir Erkoç, whose hardworking and thorough scientific personality I will always greatly admire. I am very fortunate to have the possibility of working with him in the future. My warmest regards and many thanks also to one of the best teachers I've ever had, Patricia Bilikmen, who for many years tutored me in English and made my foreign adventure possible.

The best gift that Ithaca has given me is undoubtedly all the great people I'm fortunate enough to call my friends. Especially close to me are Connie Chang, Maurizio Chinchio, Ivan Daykov and Matija Čuk, whom I've known almost from the first day. Their absence will create a huge void in my life, which I don't know if I can ever fill. Friday dinners wouldn't have been the same without Steve Drasco, Sean Garner, Bill Silveira, and Etienne Racine. Even though they are not a part of the old crowd, Jean-François Briere and Catherine Baron have also become very important to me in a very short time. Only makes me wish they had come earlier. I would also like to thank David Roundy, Ivan Daykov, Jean-François Briere, Daniel Freedman and Sahak Petrosyan for making both of our windowless offices infinitely

more bareable with their friendship.

Last but definitely not least, I have learnt here that it is possible to have a second family away from one's own. All my love to my Niki, Nancy, Miltos, Yeşim, Onur and Ömer, without whom nothing would have been the same.

It goes without saying of course that I've had many many other great friends over the years whose names aren't here. They have all made me rather be in Ithaca than anywhere else during the long and harsh winters and that's saying a lot!

TABLE OF CONTENTS

1	Introduction	1
1.1	Theoretical exploration of small scale systems	1
1.2	Computational tools and theoretical techniques	4
1.2.1	Interatomic potentials	5
1.2.2	The tight-binding method	7
1.2.3	Density functional theory	12
1.3	Thesis layout	18
	Bibliography	19
	Bibliography	19
2	<i>Ab initio</i> study of defect-related losses	21
2.1	Mechanical response of defects	22
2.2	Application to divacancy in silicon	28
2.3	Calculations and results	32
2.3.1	Divacancy ground state	32
2.3.2	Q^{-1} and prediction of defect concentration	36
2.4	Conclusion	37
	Bibliography	38
	Bibliography	38
3	Electron-Phonon Interactions in Metallic Carbon Nanotubes	40
3.1	Introduction	40
3.2	Electronic structure of nanotubes	42
3.3	Fermi's Golden Rule	43
3.4	Calculation of matrix elements	46
3.4.1	Optic phonons	46
3.4.2	Zone-edge phonons	51
3.5	Results	54
3.6	Conclusion	56
	Bibliography	57
	Bibliography	57
4	Mechanical loss due to phonon-phonon interactions in suspended carbon nanotubes	58
4.1	Introduction	58
4.2	Akhieser Limit($\lambda \gg \ell_{ph}$)	60
4.3	Landau-Rümer Limit($\lambda \ll \ell_{ph}$)	64
4.3.1	Phonon Green's functions	64
4.3.2	Feynman rules	67

4.3.3	Renormalization, polarization and quality factor	72
4.3.4	Experimental conditions, impact of symmetry	74
4.3.5	Three-phonon processes	76
4.3.6	Four-phonon processes	82
4.4	Methods	85
4.4.1	Calculation of γ_q and $\frac{\partial M_x}{\partial \rho^2}$	85
4.4.2	Bloch's theorem and calculations in nanotori	86
4.5	Results	88
4.6	Conclusion	89
	Bibliography	93
Bibliography		93
5	Modelling a Suspended Nanotube	94
5.1	Introduction	94
5.2	Analytic model and computational techniques	96
5.3	Dimensionless parameters	98
5.4	Numerical results and discussion	99
5.4.1	Small V regime	102
5.4.2	Intermediate V regime	102
5.4.3	Large V regime	106
5.5	Comparison with experiment	108
5.6	Conclusion	110
	Bibliography	113
Bibliography		113

LIST OF TABLES

1.1	Atomistic empirical potentials used throughout this work: EDIP [19] and Tersoff-Brenner [20].	8
1.2	Parameterization of the transfer integrals	11
2.1	Activation-volume and anelastic tensors for competing ground-state structures of singly negatively charged divacancy in silicon	35
3.1	Results from tight binding calculations. We present band gaps and coupling matrix element, M_{kq} corresponding to each of the two optic and four zone-edge phonons.	55
4.1	Feynman rules. Representations, numbers and contributions of the different elements constituting a Feynman diagram.	71

LIST OF FIGURES

1.1	Components of s and p orbitals along and perpendicular to the bond direction in graphene. The integrals depicted on the left hand side are non-zero and their parameterization is given below in Table 1.2.2. Those on the right hand side are zero by symmetry. The hashed halves of the orbitals differ from the empty halves by a sign.	11
2.1	Divacancy shown along the $\langle 110 \rangle$ defect axis. The two black spheres represent the missing atoms and the gray spheres represent the silicon atoms. The large gray spheres are the six nearest neighbors that are left with dangling bonds after the divacancy is created.	29
2.2	Projection of divacancy structure along $\langle 111 \rangle$ symmetry axis: missing atoms (dashed circles), atoms in plane closer to observer (larger solid circles), atoms in plane further from observer (smaller solid circles).	31
2.3	LDA results and comparison to experiment of $\Delta\Lambda_\alpha$, $\Delta\Lambda_\beta$ and B_{33} . For each data set the black bar corresponds to the experimental data, the white bar to our LDA results for the pairing configuration and the gray to those for the resonant configuration. B_{33} has been scaled by C_{11} for display purposes.	35
3.1	Wavevector selection rules and tight-binding band structure of (a) a metallic single-walled nanotube and (b) a semiconducting single-walled nanotube	44
3.2	Band gap in the presence of (a) a longitudinal optic phonon and (b) a transverse optic phonon.	47
3.3	Electron momentum transfer upon emission of a zone-edge phonon(left). The transition takes place between two distinct Fermi points, with a phonon momentum of $\vec{q} = \vec{k}_F$. The reciprocal vectors are labeled \vec{b}_1 and \vec{b}_2 and the hexagonal area is the first Brillouin zone. For reference, the real space orientation corresponding to the reciprocal space picture on the left is also shown (right) with lattice vectors labeled \vec{a}_1 and \vec{a}_2 .	48
3.4	The unperturbed 12-atom graphene supercell (a) and the four in-plane zone-edge modes in the supercell (b)-(e). The displacements in the phonon modes are magnified for ease of vision.	48
4.1	Feynman diagram for a general interaction. The shaded bubbles denote a repeating subset of diagrams.	74
4.2	Feynman diagrams corresponding to three-phonon processes	77
4.3	Polarization diagram for the three-phonon Dyson sum.	77
4.4	Dispersion relation for (12,0) and (18,0) nanotubes	79
4.5	Polarization diagram for the four-phonon Dyson sum.	82

4.6	Coordinate transform in nanotori. (a) Before transform. Bloch's theorem does not apply due to lack of symmetry. (b) After transform. Each point on the nanotube has a set of coordinate axes that are aligned with the radius. Bloch's theorem can be used.	85
4.7	Nanotorus. We use nanotori in our calculations of γ_q and $\frac{\partial^2 M_\times}{\rho^2}$ because it provides an approximation to a nanotube with a large wavelength disturbance.	87
4.8	Dependence of M_\times on ρ . (a) extrapolated to zero (b) close-up . . .	87
4.9	Q^{-1} and Q versus temperature for three-phonon processes in the Landau-Rümer limit for (a) a (12,0) nanotube and (b) an (18,0) nanotube.	90
4.10	Q^{-1} and Q versus temperature for four-phonon processes in the Landau-Rümer limit for (a) a (12,0) nanotube and (b) an (18,0) nanotube.	91
5.1	(a) suspended nanotube under the action of a gate voltage V , (b) <i>jump-rope</i> mode	95
5.2	Discretization of the continuous nanotube into discrete <i>beads</i> . Each bead corresponds to one of the portions of equal length. The position, \vec{r}_i vectors of the beads, which the discrete form of the energy is written in terms of, are indicated with respect to a chosen origin, O	98
5.3	Frequency versus slack at zero force control parameter: classic solution for zero slack (points on vertical axis), numerical results for non-zero slack (curves). The dimensionless frequency $\tilde{\nu} = \nu\sqrt{\mu L^4/F}$ applies to a general system. The modes are doubly-degenerate and odd (solid curves), out-of-plane and even (dashed curves) or in-plane and even (dotted curves). Arrows indicate mode crossings. .	100
5.4	(a) Dimensionless frequency versus force control parameter: in-plane modes (dashed curves), out-of-plane modes (dotted curves), degeneracy of in- and out-of- plane modes (solid curves). (b) Dimensionless frequency versus force control parameter scaled by fourth-root of slack ($v/\sqrt[4]{s/1\%}$) for three values of slack s : 0.25% ('+'), 1% (curves), 2% ('⊙'). Frequency in MHz and voltage in V refer to the nanotube example described in the text. The scaled frequency $\tilde{\nu} = \nu\sqrt{\mu L^4/F}$ and the force control parameter $\tilde{v} = \sqrt{fL^3/F}$ apply to a general system.	101

5.5	The three regimes in which nanotube behavior simplifies, as a function of voltage and slack. The dashed line between the “hanging spring” and “hanging chain” regimes is the crossing between the second even in-plane mode and the second odd in-plane mode. The dotted line separating the “buckled beam” regime from the “hanging chain” regime is the contour on which the derivative $\frac{d \log \omega}{d \log s}$ has a value of $-1/8$. The axis on the right shows the force control parameter, $\tilde{V} = \sqrt{fL^3/F}$	103
5.6	Nanotube in the <i>hanging chain</i> regime, forming a <i>catenary</i> . In this limit, it can be treated as a parabola with width W and depth H , with a tension T at angle θ	106
5.7	Comparison of numerical results to experimental data. We reproduce here the ν versus V plot (left) from Figure 5.4 for ease of comparison to experimental results from [12] (right)	109
5.8	Histograms for the two lowest frequencies in the presence of asymmetry in clamping. The plots show distributions of the two lowest frequencies of the nanotube dispersion relation for ~ 100 calculations. The results in the top plot were obtained by constraining the clamps to point in the same direction, whereas the results in the bottom plot were obtained for clamps pointing in different directions. On the left hand of this figure, we show the relaxed profiles from two example runs corresponding to these situations. Note that the vertical coordinate of the profiles has a different scale than the horizontal coordinate for ease of vision.	111

Chapter 1

Introduction

1.1 Theoretical exploration of small scale systems

In the last two decades micro- and nano-scale devices have gained increasingly more importance in interdisciplinary research. Their small size and often extraordinary mechanical, electrical and vibrational properties have opened up endless possibilities of using these devices in many applications. To give a few examples of these applications, we mention here chemical and biological sensors [1], flat screen displays [2], attogram mass detectors [3], parametric amplifiers [4], actuators [5, 6], diodes [7], hydrogen storage devices [8] and band gap engineering [9]. A very extensive review and many more illustrative examples of application is given in [10].

Small scale devices exhibit properties that are significantly different from bulk materials. As the system size decreases these properties increasingly deviate from what can be extrapolated by scaling down a macroscopic material. It is therefore of great importance to supplement this immense body of experimental work with theoretical studies in predicting and explaining the new physics that emerges at these small scales. A large number of theoretical studies have already been made to this end [11, 12, 13, 14, 15]. In addition to explaining the phenomena behind the observations, theoretical work in the field of small scale systems plays a key role in helping select appropriate systems to study and design successful experiments.

Some of the most important nano- and micro-scale devices, such as mass detectors and actuators, rely on the excitation of vibrations capacitively or by means of passing an electrical current through the system. Such devices are referred to

as *nano-* and *micro-electromechanical systems* (NEMS and MEMS respectively). NEMS and MEMS make up a large subset of small-scale devices and are used in many scientific and technological applications, in particular as sensors.

Due to their small mass, NEMS and MEMS, in principle, have the ability to detect very small changes in frequency when a relevant variable, such as the applied force, is changed. This sensitivity to small changes however can only be utilized if the resonance frequencies are well-defined. The frequency response of an ideal oscillator in the absence of any kind of friction is a collection of infinitely sharp peaks located at its resonant frequencies. When a loss mechanism is introduced, causing dissipation of energy, the resonance peak broadens making it harder to detect small changes in frequency. A commonly used measure of dissipation is the *quality factor*. The quality factor is defined as the fraction of energy lost per cycle per radian in a vibrating system and is usually described by the following general expression

$$Q^{-1} = \frac{1}{2\pi} \frac{\Delta E}{E} \quad (1.1)$$

where ΔE is the energy lost per cycle and E is the total energy in the oscillator. It follows that the precision of a device relies heavily on a high quality factor, and it is therefore important to understand the causes of mechanical loss in a system in order to maximize the quality factor.

In NEMS and MEMS, it proves more difficult to identify the dominant mechanisms that cause mechanical loss than in bulk systems. The fabrication mechanisms involved are complicated and may introduce uncontrolled sources of loss into the devices. The mechanisms that introduce mechanical loss can be divided into two classes: *intrinsic* and *extrinsic*.

Intrinsic losses exist in any given system and result from fundamental processes

in the system such as electron-phonon interactions, phonon-phonon scattering and thermoelasticity. The losses due to these effects cannot be eliminated and therefore it is very important to understand the effect of such processes to establish the theoretical limitations on the performance of a device.

Extrinsic losses on the other hand are mechanisms introduced by external factors. Examples to extrinsic losses are interactions with ambient gas, clamping, defects, surfaces and impurities introduced by chemical treatment during fabrication. Such mechanisms can, at least in principle, be eliminated to a certain extent by techniques such as improving the vacuum, making better contacts, annealing and chemical treatment. Which of these techniques to use of course depends on the mechanism in question. It is therefore very important to identify which mechanism is dominant in the device.

This thesis includes the study of an intrinsic and an extrinsic mechanism in NEMS and MEMS devices. In Chapter 2, we study the energy loss due to reorientation between different configurations of *divacancies* in silicon. In Chapter 4, we perform calculations to determine the contribution to the quality factor caused by phonon-phonon interactions in suspended nanotube devices. We emphasize that for NEMS and MEMS devices, there are several loss mechanisms, each of which are equally important to identify and study. Exploring the relative magnitude of a given loss mechanism for a particular system requires both experimental data and theoretical understanding. This subject therefore stimulates close collaboration between the two fields.

1.2 Computational tools and theoretical techniques

Nanoscience is both interesting and challenging because it involves simultaneously quantum mechanical behavior and practical issues. Theoretical work in this field must deal appropriately with many-body quantum mechanics and be able to make specific quantitative predictions. This thesis thus combines a number of theoretical methods ranging from continuum theory (Chapter 5) through standard quantum mechanics (Chapter 3) to quantum many-body perturbation theory (Chapter 4) with a number of computational techniques for quantitative prediction of materials properties. The computational techniques that we use range from atomistic potentials (Chapter 4) through tight-binding methods (Chapter 3) to density functional theory (Chapter 2). Combining these two groups of methods, which are often practiced in isolation, required some of the greatest care in this work. Because the theoretical methods used are so tightly coupled to the problems addressed, we defer the description of these methods to the relevant chapters. We shall, however, review here the computational techniques, which are more independent of the type of problem at hand.

Each section of this thesis employs a different computational technique for calculating the quantities needed in the various theories which we use. In computational science, an increase in the accuracy of methods is usually accompanied by a decrease in speed and in simplicity. However, this does not mean that methods with lower accuracy can not be used in predictive calculations. With a careful choice of the problem to which these methods are applied, they can prove very useful, especially for large system sizes due to their speed. For example in [15], a Lennard-Jones potential is used to model the weak van der Waals interaction between a nanotube cantilever and the gate over which it is suspended. The Lennard-Jones

potential [16] is perhaps the simplest model for interatomic interaction with only two parameters and therefore requires minimal computational effort. In spite of this simplicity, in certain cases such as in [15], it can prove very useful in predicting key properties of large systems. It can not, however, be expected to give accurate results for calculation of more detailed quantities such as phonon-phonon coupling constants.

The Lennard-Jones potential is a very elementary example of one of the tools that we use in this thesis, namely *empirical interatomic potentials*. In this thesis we make extensive use of these potentials for certain properties of the systems we study. For more accurate calculations, we resort to more sophisticated but computationally more demanding techniques. These well-known techniques are *tight-binding approximation* and *density functional theory*. Below, we present a brief description of each of these methods in order of increasing accuracy and detail.

1.2.1 Interatomic potentials

An interatomic potential is a description of the energy of a system of atoms in terms of only the ionic positions. The electrons in the system are not treated explicitly but rather are taken into account through the two-, three- or many-body interaction terms in the potential. Although many different methods are employed in developing interatomic potentials, in general terms such potentials have the form

$$E = V(\vec{r}_1, \vec{r}_2, \dots, \vec{r}_N; \alpha_1, \alpha_2, \dots, \alpha_M). \quad (1.2)$$

where \vec{r}_i are the positions of the N atoms and α_i are the M adjustable parameters included so as to give an accurate description of some chosen properties.

A common method for developing such interatomic potential models is to truncate the real, many-body interaction of the system by including only two- and three-body terms,

$$E = \frac{1}{2} \sum_{i,j} V_2(r_{ij}) + \sum_{ijk} V_3(r_{ij}, r_{jk}, r_{ik}), \quad (1.3)$$

such potentials are termed *cluster potentials* in [17]. These potentials mimic well the dependence of the energy on the interatomic separation as well as the bond configuration. Lennard-Jones [16] and Stillinger-Weber [18] potentials are examples of cluster potentials.

A more sophisticated class of interatomic potentials consist of the *cluster functionals* [17], which take into account the local environment of each atom in addition to the two- and three-body terms. The interatomic potentials, EDIP [19] for silicon and Tersoff-Brenner [20] for carbon, that we use in the chapters below both belong to this category. Although these functions achieve better *transferability* in that they describe well a wider range of structures, they are usually more complicated in terms of functional form, number of fitting parameters and computational expense. The functional form is usually [17]

$$E = \frac{1}{2} \sum_{ij} f_c(r_{ij}) [A_1 \phi_1(r_{ij}) - A_2 \phi_2(r_{ij}) p(\zeta_{ij})] \quad (1.4)$$

where p is a measure of *bond-order*, which is an indicator of the degree of bonding for a pair of atoms, ζ_{ij} is an effective coordination number, and A_1 and A_2 are adjustable parameters.

There are other methods of determining functional forms such as embedded-atom method for metals [21] and the force-matching method [22] but the two methods discussed above are the ones we employ in this thesis.

In the second stage of the development of an interatomic potential, the parameters are fitted to a set system properties. Some of the properties commonly used are bulk modulus, lattice constants, elastic constants and crystal structure in different phases of the material. The fits can either be made to experimental data as in the case of the Stillinger-Weber potential or, as in EDIP, to numerical results with higher levels of detail obtained through such methods as density- functional theory.

As mentioned earlier in this section, care must be taken in using interatomic potentials. Since these potentials are usually fit to elastic properties and equilibrium crystal structures, they give fairly reliable results for these quantities. We emphasize that it is only for such quantities that we rely on such simple potentials in this thesis. In all of the four chapters in this thesis, interatomic potentials have been employed in either directly calculating elastic properties, vibration spectra and configurations or checking convergence of the result of a more accurate calculation in a smaller system. Table 1.1 maps out the instances where we employ these potentials, specifying the particular potential used.

1.2.2 The tight-binding method

In Chapter 3, we study the interaction between electrons and phonons. With the involvement of electronic effects, we can no longer use interatomic potentials, because they only treat the effects of electrons indirectly. Instead, we use *the tight-binding approximation*, which describes the band structure of semiconductors with reasonable accuracy.

The tight-binding method was first introduced by Slater and Koster in their original paper in 1954 [23]. It is an approximation that deals with the class of

Table 1.1: Atomistic empirical potentials used throughout this work: EDIP [19] and Tersoff-Brenner [20].

Usage	Chapter	Potential
Structural relaxation of a defect	2	EDIP
Convergence of defect activation tensor	2	EDIP
Elastic moduli needed in continuum theory	5	Brenner
Structural relaxation of nanotubes with curvature	4	Brenner
Phonon dispersion relation in nanotubes	4	Brenner
Phonon dispersion relation in graphene supercell	3	Brenner

solids where the atoms are separated by a distance large enough that the electronic wavefunctions can be described as being built from atomic orbitals, but not so far away that one can completely ignore the overlap between wavefunctions localized on neighboring atoms. This approximation works best when describing the partially-filled d -bands of transition metals and the electronic structure of semiconductors [24].

In this framework, the Bloch wavefunction of each electron is given by

$$\Psi_{\alpha}(\vec{r}) = N_{cell}^{-1/2} \sum_{\vec{R}_i} \exp(i\vec{k} \cdot \vec{R}_i) \phi_{i\alpha}(\vec{r} - \vec{R}_i), \quad (1.5)$$

where i refers to the atomic site and α to the atomic orbital, N_{cell} is the number of unit cells in the system and $\phi_{i\beta}(\vec{r} - \vec{R}_i)$ is the atomic orbital β localized on an atom at location \vec{R}_i , and \vec{R}_i runs over the atoms in the unit cell. With this

wavefunction, the matrix elements of the electronic Hamiltonian are

$$H_{\alpha\beta,\vec{k}}(\vec{r}) = \varepsilon_\beta \delta_{\alpha\beta} + \sum_{\vec{R}_i, \vec{R}_j \in \text{NN}} \exp\{i\vec{k} \cdot (\vec{R}_i - \vec{R}_j)\} \int \phi_{j\alpha}^*(\vec{r} - \vec{R}_j) H(\vec{r}) \phi_{i\beta}(\vec{r} - \vec{R}_i) d\vec{r}, \quad (1.6)$$

where ε_β is the *on-site* energy, which describes the energy of an atomic orbital on a given atom, and \vec{R}_i and \vec{R}_j generally vary over the nearest and second nearest neighbors.

According to the review given in [25], the idea common to all tight-binding schemes is to replace the integral in (1.6) by a suitable parameter, which depends only on the relative atomic positions, $\vec{R}_i - \vec{R}_j$, and the symmetry of the atomic orbitals. In order to facilitate this replacement, we make the well-known *two-center integral approximation*, which replaces H in Equation 1.6, which consists of the sum of contributions from all the atoms in the system by the contributions of just the atoms i and j in which the orbitals in question are centered.

The next step in parameterization is expanding the atomic orbitals $\phi_{i\alpha}(\vec{r} - \vec{R}_i)$ in terms of orbitals with well defined angular momenta. Interpreted geometrically for the graphene system that we study in Chapter 3, this breakdown of the atomic orbital corresponds to a projection of p_x and p_y orbitals along and perpendicular to the bonds as demonstrated in Figure 1.2.2. In its parameterized form, then the value of the integrals can be written as a constant depending on the atomic separation and an angular part. The Hamiltonian can be written in terms of these constant parameters as

$$H_{i\alpha j\beta,\vec{k}} = \varepsilon_\beta \delta_{\alpha\beta} + N^{-1} \sum_{\vec{R}_i, \vec{R}_j \in \text{NN}} \exp\{i\vec{k} \cdot (\vec{R}_i - \vec{R}_j)\} h_{\alpha\beta J}(|\vec{R}_i - \vec{R}_j|) G_{\alpha\beta J}(\theta_{ij}), \quad (1.7)$$

where H is now given in a fully discrete form in contrast to Equation 1.6, $h_{\alpha\beta J}$ is the parameter for this integral corresponding to the projection of the atomic orbitals

with angular momentum J and $G_{\alpha\beta J}(\theta_{ij})$ is the angular dependence, which can be obtained from [23]. The parameters of the tight-binding model of Goodwin [26], which we use in this thesis is tabulated in Table 1.2.2.

Notice that $h_{\alpha\beta J}$ depends on the separation $|\vec{R}_i - \vec{R}_j|$. Tight-binding models differ not only in their parameterization of the integral but also in the particular form for this separation dependence. In Goodwin's model, this dependence is taken to be

$$h_{\alpha\beta J}(r) = h_{\alpha\beta J}(r_0) \left(\frac{r_0}{r}\right)^{2.796} \exp \left[-2.796 \left(\frac{r}{2.32 \text{ \AA}}\right)^{22} + 2.796 \left(\frac{r_0}{2.32 \text{ \AA}}\right)^{22} \right], \quad (1.8)$$

where $h_{\alpha\beta J}(r_0)$ is given in eV and tabulated in Table 1.2.2 for various orbitals. r_0 is the equilibrium nearest-neighbor of carbon in the graphene phase and is given as $r_0 = 1.41 \text{ \AA}$ in [26]. By diagonalizing the Hamiltonian in Equation 1.7, we obtain the band structure of the system. In general, the eigenstates are not explicitly constructed in the tight-binding Hamiltonian. We sum up all the eigenstates with the appropriate Fermi weights at finite temperature to obtain a band energy, E_{band} . The total energy is given by

$$E = E_{band} + E_{rep}, \quad (1.9)$$

where E_{rep} is a pairwise repulsive energy making up for all the contributions unrelated to the band energy. E_{rep} in general is parameterized in a similar manner to the separation dependence of the transfer integrals. In this thesis, we only deal with the band structure of graphene. We shall therefore not discuss total energy calculations in detail.

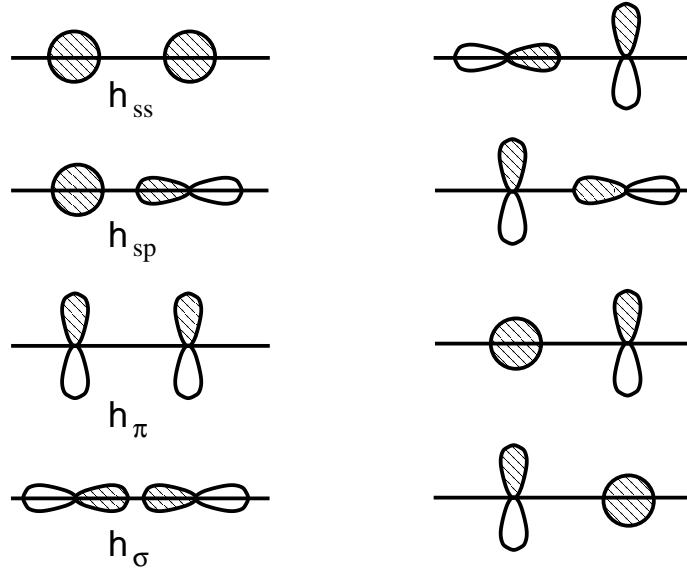


Figure 1.1: Components of s and p orbitals along and perpendicular to the bond direction in graphene. The integrals depicted on the left hand side are non-zero and their parameterization is given below in Table 1.2.2. Those on the right hand side are zero by symmetry. The hashed halves of the orbitals differ from the empty halves by a sign.

Table 1.2: Parameterization of the transfer integrals

Matrix element	Value (eV)
h_{ss}	-6.769
h_{sp}	-5.580
h_{σ}	-5.037
h_{π}	-3.033
ϵ_{2s}	-8.868
ϵ_{2p}	0.0

1.2.3 Density functional theory

Density functional theory belongs to a class of numerical methods known as *ab initio* methods. As their name implies, the only input to such methods are the fundamental constants of nature and the atomic numbers of the nuclei in the system. Unlike the previously discussed methods, *ab initio* techniques aim to take into account all the interactions involving atoms and electrons of the system. Since it quickly becomes an impossible task to describe the $3N$ degrees in terms of many-body wavefunctions as the system size increases, density functional theory uses a different variable, namely, the *electronic density* of the system, which depends only on the three Cartesian coordinates. The electronic density of a system is given by

$$n(\vec{r}) = \sum_i f_i |\psi_i(\vec{r})|^2, \quad (1.10)$$

where $\psi_i(\vec{r})$ are the electronic Kohn-Sham orbitals of the system and f_i are the fillings corresponding to these orbitals. The Hamiltonian of a system of electrons evolving under the mutual Coulomb interaction and an arbitrary external potential is

$$H = \hat{T} + \hat{V}_{ext} + \hat{V}_{ee}, \quad (1.11)$$

where \hat{T} is the kinetic energy operator, \hat{V}_{ext} is the external potential and \hat{V}_{ee} is the interaction between the electrons. The total energy of such a system can be written as a *functional* of the orbitals as

$$E_{tot}[\psi_i] = \frac{1}{2} \sum_i f_i \int \nabla \psi_i^*(\vec{r}) \nabla \psi_i(\vec{r}) d\vec{r} + \int v_{ext}(\vec{r}) n(\vec{r}) d\vec{r} + \frac{1}{2} \int \int \frac{n(\vec{r}) n(\vec{r}')}{|\vec{r} - \vec{r}'|} d\vec{r} + E_{xc}[n(\vec{r})], \quad (1.12)$$

where $E_{xc}[n]$ is the *exchange-correlation energy* which contains all the electron-electron interaction effects that the Coulomb potential does not capture. Note

that here and in the rest of this section we use atomic units, where $\hbar = m = e = 1$. The foundation of density functional theory was established by a very simple yet powerful theorem proven by Hohenberg and Kohn in 1964 [27]. This theorem states that in the ground state of the system $v_{ext}(\vec{r})$ is a unique functional of $n(\vec{r})$. Since $v(\vec{r})$ fixes $E_{tot}[n]$, $E_{tot}[n]$ is also a unique functional of $n(\vec{r})$. Kohn and Sham [28] later generalized this result to include the above formulation in terms of the orbitals ψ_i and by similar reasoning showed the exchange-correlation energy to be a unique functional of $n(\vec{r})$, $E_{xc}[n(\vec{r})]$.

A second, equally powerful theorem by Hohenberg and Kohn [27], is the variational principle for the density of the system, which states that for electronic densities that obey the particle conservation constraint,

$$N[n(\vec{r})] = \int n(\vec{r})d\vec{r} = N, \quad (1.13)$$

the energy functional E_{tot} is minimized for the ground state density. This, together with the uniqueness theorem leads us to the elegant result that if all the terms in the energy functional are known exactly, we can simply minimize E_{tot} with respect to $\psi_i(\vec{r})$ to find the ground state density and energy of any system. However, $E_{xc}[n(\vec{r})]$ is not known exactly for a general system and in practice is replaced with various approximations. Development of approximate exchange-correlation functionals is an active area of research and there are many examples in literature. One of the most common approximations used is the *local density approximation* (LDA), which states that [28] for sufficiently slowly-varying $n(\vec{r})$, E_{xc} is well-approximated by

$$E_{xc} = \int n(\vec{r})\epsilon_{xc}(n(\vec{r}))d\vec{r}, \quad (1.14)$$

where $\epsilon_{xc}(n(\vec{r}))$ is the exchange and correlation energy per electron of a uniform electron gas. Several parameterizations of local density approximation are given

in literature [29, 30, 31] as well as approximations beyond local density approximation such as *generalized gradient approximation* [32] and *optimized potential method* [33]. In our calculations in Chapter 2, we use the spin-polarized version of the local density approximation functional, called *spin local density approximation* [34].

Due to the variational principle mentioned above, the energy of the system is invariant under small perturbations in the orbitals around the ground state. In other words, for an infinitesimal perturbation, δn , to the electronic density,

$$\int \delta\psi_i(\vec{r}) \left\{ -\frac{1}{2}\nabla^2 + \phi(\vec{r}) + \mu_{xc}(n(\vec{r})) \right\} \psi_i(\vec{r}) d\vec{r} = 0, \quad (1.15)$$

where

$$\mu_{xc} = \frac{d[n\epsilon_{xc}(n)]}{dn} \quad \text{and} \quad \phi(\vec{r}) = v_{ext}(\vec{r}) + \int \frac{n(\vec{r}')}{|\vec{r} - \vec{r}'|} d\vec{r}'. \quad (1.16)$$

For given $\phi(\vec{r})$, we can obtain orbitals, $\psi_i(\vec{r})$ that satisfies Equation 1.15 by solving the following one-particle set of equations for a given $\phi(\vec{r})$ and $\mu_{xc}(\vec{r})$:

$$\left\{ -\frac{1}{2}\nabla^2 + \phi(\vec{r}) + \mu_{xc}(n(\vec{r})) \right\} \psi_i(\vec{r}) = \epsilon_i \psi_i(\vec{r}). \quad (1.17)$$

These equations were first written down by Kohn and Sham in 1965 [28] and are commonly referred to as *Kohn-Sham equations*. The Kohn-Sham equations, although seemingly simple need, in fact, to be solved in a self-consistent scheme since $n(\vec{r})$ that creates the effective potential depends on the Kohn-Sham orbitals, $\psi_i(\vec{r})$, which in turn depend on the effective potential.

After self-consistency is achieved, the total energy can be found by

$$E_{tot} = \sum_i f_i \epsilon_i - \frac{1}{2} \int \int \frac{n(\vec{r})n(\vec{r}')}{|\vec{r} - \vec{r}'|} d\vec{r}d\vec{r}' + \int n(\vec{r})[v_{xc}(n(\vec{r})) - \mu_{xc}(n(\vec{r}))] d\vec{r}. \quad (1.18)$$

Up to this point, we have given an exact recipe for calculation of the total energy of a system of electrons with the exception of the local density approximation used in calculating the exchange-correlation energy. In practice, however, it

is still a prohibitively large task to perform the self-consistent solution of Equation 1.17 for an arbitrary system. Therefore, a few well-controlled approximations are needed in order to calculate the energy in a reasonable amount of time. An extensive review of practical issues involved in a density functional calculation is given in [35]. In the numerous implementations of density functional theory in literature, the approximations used vary depending on the system and the particular implementation.

1. **Basis set truncation :** The Kohn-Sham orbitals, ψ_i , are usually expanded in terms of a convenient basis set [36] as,

$$\psi_i(\vec{r}) = \sum_{\alpha} b_{\alpha}(\vec{r})C_{\alpha i}, \quad (1.19)$$

where $b_{\alpha}(\vec{r})$ are the basis functions and $C_{\alpha i}$ are the expansion coefficients. Among the bases usually chosen in calculations are plane-waves [35], Gaussian orbitals [37] and wavelets [38]. The choice of the particular basis depends on the system being studied. In our calculations, we work with a plane wave basis. The wavefunctions of the systems are represented exactly for an infinite set of plane-waves. To make computations possible, we truncate the above sum over basis functions and only work with those plane-waves whose energies are below a certain cutoff, on the premise that wavefunctions are sufficiently smooth to be represented accurately by low-frequency planewaves. When calculating E_{tot} for a system, a convergence study with respect to the energy cutoff must be made and truncation must be only after the energy is fully converged.

2. **Supercell representation :** In calculating properties of infinite systems such as solids, we make use of the periodicity of the system and divide it

into identical units, which are termed *supercells*. Making use of Bloch's theorem computations in the unit cell become plausible. An ideal crystal has full translational symmetry and the smallest repeating unit is actually the unit cell of the system. In contrast, for a crystal in which the translational symmetry is broken by a given defect, the supercell description is no longer appropriate. In practice however, a suitable choice of a supercell is often made by embedding the defect in a large amount of bulk material. This supercell approach has been applied successfully to a wide range of defects such as point defects [39], surfaces [40], dislocations [41] and even isolated clusters [42].

As an example in this thesis we use the supercell description of a point defect. This description represents not a single, isolated point defect but a repeated array of defects with the periodicity of the supercell. The supercell, then, must be taken large enough that long range defect-defect interactions are small. In Chapter 2, we study a *divacancy* in silicon in a 62-atom supercell. To make sure that the energy is well-converged with respect to supercell size, we use EDIP, which is a reliable interatomic potential for capturing long range stress-induced defect-defect interactions to calculate the energy of the defect for larger supercell sizes. Results for this study are presented in Chapter 2.

3. **Pseudopotentials :** In most systems, especially in covalently bonded solids, most properties can be explained in terms of valence states, with the effects of the core states being small. This physical fact provides a motivation for yet another approximation that decreases the computational effort needed to compute system properties, namely the *pseudopotential approxi-*

mation [35].

Due to the strong interaction around atomic cores, wavefunctions exhibit high-frequency spatial oscillations in these regions that require the inclusion of high-frequency planewaves in the basis set. To circumvent the problem of such a large basis set, the pseudopotential approximation replaces the ionic potential within a cutoff radius around the ions by a smoother potential. The oscillatory behavior of the valence wavefunctions near cores are also smoothed out at the end of this procedure. The new potential is generated to mimic exactly the scattering properties of the true potential outside of the cutoff. Pseudopotential theory is a broad area of research in itself. Examples of the most commonly used pseudopotentials are Kleinman-Bylander [43] and ultrasoft potentials [44]. In our calculations in Chapter 2, we use a Kleinman-Bylander pseudopotential.

The various approximations listed above make the computational effort needed to carry out density functional theory calculations feasible. Even with these approximations, it still remains quite challenging to solve the coupled set of Kohn-Sham equations of Equation 1.17 by direct diagonalization in the basis set chosen for the problem. However, due to the knowledge that the wavefunctions must minimize the total energy in the ground state, we can cast the coupled set of equations into a minimization problem with respect to the expansion coefficients in Equation 1.19. We can then perform a constrained minimization using one of the many well-known algorithms in literature. In our calculations, we use the analytically-continued *preconditioned conjugate gradients* algorithm [45].

1.3 Thesis layout

In chapter 2, we introduce a new method for obtaining the ground state structure of defects by looking at their mechanical response. This method involves calculation of the *activation volume tensor* of the defect using reliable *ab initio* techniques. As an application, we calculate the activation volume tensor Λ of a *divacancy* in silicon, which is a commonly encountered defect introduced in the fabrication stages of silicon actuators. By comparison of the activation volume tensor to experimental values, we identify the ground state of this defect, which has proved controversial in the literature. In addition, we calculate the mechanical energy loss caused by divacancies in a silicon oscillator.

In chapter 3 presents the calculation of electronic mean-free path in carbon nanotubes under high-bias. Electron-phonon interactions have been found to have a considerable effect in the determination of the electron mean-free path. We determine the mean-free path of the nanotubes in the presence of various phonon modes that cause scattering of electrons.

In chapter 4, we explore a fundamental loss mechanism intrinsic to any system, namely loss due to phonon-phonon interactions. In particular, we study the contribution of phonon-phonon interaction to loss in suspended nanotubes for various scattering mechanisms.

Chapter 5 concludes this thesis with results from our continuum mechanics calculations for a suspended nanotube, which has recently become an exciting possibility for a device application. We explore the dependence of the vibration frequencies on such factors as downward force and built-in slack in the nanotube.

Bibliography

- [1] C. Wang and M. Madou, Phys. Rev. Lett. **20**, 2181 (2005).
- [2] C.-C. Zhu, W. Liu, and L. Huangfu, J. Vac. Sci. Technology. B. **19(5)**, 1691 (2001).
- [3] R. Ilic *et al.*, J. Appl. Phys. **95**, 3694 (2003).
- [4] D. W. Carr *et al.*, Appl. Phys. Lett. **77**, 1545 (2000).
- [5] A. Husain *et al.*, Appl. Phys. Lett. **83**, 1240 (2003).
- [6] V. Sazonova *et al.*, Nature **431**, 284 (2004).
- [7] Z. Yao, H. C. Postma, L. Balents, and C. Dekker, Nature **402**, 273 (1999).
- [8] T. Yildirim and S. Ciraci, Phys. Rev. Lett. **94**, 175501 (2005).
- [9] E. D. Minot *et al.*, Phys. Rev. Lett. **90**, 156401 (2003).
- [10] R. H. Baughman, A. A. Zakhidov, and W. A. de Heer, Science **297**, 787 (2002).
- [11] S. Sapmaz, Y. M. Blanter, L. Gurevich, and H. S. J. van der Zant, PRB **67**, 235414 (2003).
- [12] W.-Q. Deng, X. Xu, and W. A. Goddard, Phys. Rev Lett. **92**, 166103 (2004).
- [13] S. Peng and K. Cho, Nano Lett. **3(4)**, 513 (2003).
- [14] A. Maiti, Phys. Stat. Sol.(b) **1**, 87 (2001).
- [15] M. Dequesnes, S. V. Rotkin, and N. R. Aluru, Nanotechnology **13**, 120 (2002).
- [16] J. E. Lennard-Jones, Proc. R. Soc. A **129**, 598 (1930).
- [17] H. B. an T. Halicioglu and W. A. Tiller, Phys. Rev B **46**, 2250 (1992).
- [18] F. H. Stillinger and T. A. Weber, Phys. Rev. B **31**, 5262 (1985).
- [19] J. F. Justo *et al.*, Phys. Rev. B **58**, 2539 (1998).
- [20] D. W. Brenner *et al.*, J. Phys.: Condens. Matter **14**, 783 (2002).
- [21] M. S. Daw and M. I. Baskes, Phys. Rev. B **29**, 6443 (1984).
- [22] F. Ercolessi and J. B. Adams, Europhys. Lett. **26(8)**, 583 (1994).
- [23] J. C. Slater and G. F. Koster, Phys Rev **94**, 1498 (1954).

- [24] N. W. Ashcroft and N. D. Mermin, *Solid State Physics* (Saunders College Publishing, New York, 1976).
- [25] C. M. Goringe, D. R. Bowler, and E. Hernández, *Rep. Prog. Phys* **60**, 1447 (1997).
- [26] L. Goodwin, *J. Phys. Condens. Matter* **3**, 3869 (1991).
- [27] P. Hohenberg and W. Kohn, *Phys Rev* **136**, B864 (1964).
- [28] W. Kohn and L. J. Sham, *Phys. Rev.* **140**, A1133 (1965).
- [29] J. P. Perdew and A. Zunger, *Phys. Rev. B* **23**, 5048 (1981).
- [30] S. H. Vosko, L. Wilk, and M. Nusair, *Can. J. Phys.* **58**, 1200 (1980).
- [31] O. Gunnarsson and B. I. Lundqvist, *Phys. Rev B* **13**, 4274 (1976).
- [32] J. P. Perdew, K. Burke, and M. Ernzerhof, *Phys. Rev. Lett.* **77**, 3865 (1996).
- [33] V. Sahni, J. Gruenebaum, and J. P. Perdew, *Phys. Rev. B* **26**, 26 (4371).
- [34] A. D. Becke, *J. Chem. Phys.* **96**, 1992 (2155).
- [35] M. C. Payne *et al.*, *Rev. Mod. Phys.* **64**, 1045 (1992).
- [36] S. Ismail-Beigi and T. A. Arias, *Computer Physics Communications* **128**, 1 (2000).
- [37] M. D. Towler, A. Zupan, and M. Causà, *Computer Phys. Comm.* **98**, 181 (1996).
- [38] T. A. Arias, *Rev. Mod. Phys.* **71**, 267 (1999).
- [39] G. Lu and E. Kaxiras, *Phys. Rev. Lett.* **94**, 155501 (2005).
- [40] S. J. Hashemifar, P. Kratzer, and M. Scheffler, *Phys. Rev. Lett.* **94**, 096402 (2005).
- [41] G. Csányi, T. D. Engeness, S. Ismail-Beigi, and T. A. Arias, *J. Phys. Condes. Matter* **12**, 10029 (2000).
- [42] O. Diéguez *et al.*, *Phys. Rev. B* **63**, 205407 (2001).
- [43] L. Kleinman and D. M. Bylander, *Phys. Rev. Lett.* **4**, 1425 (1982).
- [44] D. Vanderbilt, *Phys. Rev. B* **41**, 7892 (1990).
- [45] T. A. Arias, M. C. Payne, and J. D. Joannopoulos, *Phys. Rev. Lett* **69**, 1077 (1992).

Chapter 2

Ab initio study of defect-related losses

Among the most powerful applications of first principles *ab initio* approaches in condensed matter systems is the interpretation of experimental signatures from defects. The extremely efficient, albeit approximate, functionals available for density-functional theory have given this approach wide application in conjunction with experimental probes such as scanning tunneling microscopy, electron paramagnetic resonance, electron-nuclear double resonance, and nuclear magnetic resonance[1, 2, 3, 4, 5, 6, 7, 8, 9, 10, 11]. Macroscopic mechanical response experiments also have proved an extremely valuable tool in the study of defects in solid-state systems[12, 13, 14, 15, 16], providing key information on such issues as defect symmetries and concentrations. However, mechanical response studies remain largely ignored by the *ab initio* community to date.

Despite their successes, the aforementioned density-functional studies suffer a fundamental flaw: no underlying theorem ensures that density-functional theory provides the energy- or angular-momentum- resolved densities probed in the experiments involved in the application. Beyond this matter of principle, such quantities are not among those which available approximate functionals predict most reliably. This chapter notes that the most reliable quantities which density-functional theory predicts (bond lengths, bond angles, and lattice parameters) relate directly to the key coupling parameter in macroscopic mechanical response experiments, the full activation-volume *tensor*. We thus propose *ab initio* study of mechanical response functions associated with this tensor as a powerful and particularly reliable new tool in the study of defects in condensed matter systems.

One such response function, internal friction, is a topic of current interest both experimentally and theoretically[17, 18, 19, 20, 21, 22]. Below we develop the theory of internal friction as applied to divacancy defects to provide the first parameter-free *ab initio* determination of friction from a point defect, in this case the singly negatively charged divacancy in silicon (Si-V_2^-). Although the structure of this defect has been inferred through a combination of experimental signatures and symmetry of electronic states[23], *ab initio* work to confirm the structure has resulted in an ongoing debate[6, 24, 25, 26] which has arisen ultimately from a focus on delicate energy differences at or beyond the limits of accuracy of current density functionals. Here, we demonstrate the power of working with mechanical response functions by providing a clear signature which resolves the debate.

2.1 Mechanical response of defects

Within linear response, the stress-dependent part of the energy of a point defect ΔE has the form

$$\Delta E = -\Lambda_{ij}\sigma_{ij}, \quad (2.1)$$

where we employ repeated index summation notation here and throughout this chapter and where σ and Λ are, respectively, the externally applied stress tensor and the *defect activation-volume tensor*. After a defect is created, the lattice around it undergoes configurational relaxation to relieve the stress caused by the defect. Λ is a measure of this distortion in the lattice around the defect. The extent of this distortion determines the magnitude of coupling of the defect to an externally applied stress.

From a practical point of view, the strain u induced in a crystal containing a concentration n of defects with activation volume tensor Λ is $u_{ij} = n\Lambda_{ij}$, a result

of minimizing the sum of the bulk and defect elastic energies. We can easily see this by observing that the total energy,

$$E_{\text{tot}} = \frac{1}{2}\sigma \cdot S \cdot \sigma - \Lambda\sigma, \quad (2.2)$$

is minimized when $S \cdot \sigma = \Lambda$. But we immediately recognize that $S \cdot \sigma$ is equal to the strain u , which completes the proof of the statement that Λ indeed minimizes the total elastic energy of the bulk and defect.

If we employ a periodic description of the crystal in terms of *supercells*, we may determine Λ simply by creating a supercell containing a single defect and relaxing the defect structure along with the supercell lattice vectors. This provides a very reliable way of accessing Λ since equilibrium supercell lattice constants are among the quantities most reliably determined within density-functional theory.

In the absence of external stress, most defects have more than one equivalent orientation with respect to the symmetry directions of the crystal. This could be determined, for example, by a symmetry axis of the defect. Under applied stress, some of these orientations are energetically preferred over others and defects with lower symmetry than the host crystal tend to reorient so as to minimize the energy. Experimental stress-alignment studies, which observe the relative thermalized populations of different orientations of specific defect types as a function of applied stress, thus allow direct access to certain linear combinations of Λ_{ij} for each type [23]. Such thermalization of defect populations under *time-varying* external stress $\sigma_{ij}(t)$ provide a mechanism for internal friction, dissipation of mechanical energy throughout the bulk of a material.

We review the determination of the friction associated with this process here in some depth because, although our overall logic is the same, the final result for the divacancy differs from the oft-quoted result [27], which assumes that all defect

orientations relax among each other at equal rates and hence does not apply to divacancies.

From Equation (2.1), the total energy per unit volume stored at time t among all defect orientations m of a specific defect type is

$$\Delta E(t) = -n \sum_m P^m(t) \Lambda_{ij}^m \sigma_{ij}(t), \quad (2.3)$$

where n is the total number density of defects of this type, and P^m and Λ_{ij}^m are the probability and activation volume tensor associated with each orientation. In the case of a driven oscillator, the externally applied stress varies harmonically in time as

$$\sigma_{ij}(t) = \tilde{\sigma}_{ij} e^{i\omega t} \quad (2.4)$$

where here and in the rest of this chapter, it has been explicitly assumed that the real parts of $P^m(t)$ and $\sigma_{ij}(t)$ are implied whenever they are mentioned unless stated otherwise.

Dissipation results from energy lost irreversibly to the heat bath through transitions among defect orientations and thus occurs at the rate

$$\frac{dE}{dt} = n \sum_m \frac{dP^m}{dt} \Lambda_{ij}^m \sigma_{ij}(t). \quad (2.5)$$

Only the term involving the derivative of the probability appears in energy loss since only transitions among orientations involve dissipation of energy irreversibly in the form of heat. Taking the transitions from orientation m to m' to be thermally activated, with rate $\nu_{mm'}$ in the absence of external stress, we write the following detailed balance equation for the probability of having a defect in orientation m

$$\frac{dP^m}{dt} = - \sum_{m' \neq m} P^m \nu_{mm'} e^{\beta \Lambda_{ij}^m \sigma_{ij}} + \sum_{m' \neq m} P^{m'} \nu_{m'm} e^{\beta \Lambda_{ij}^{m'} \sigma_{ij}} \quad (2.6)$$

The first term in Equation (2.6) is the transition rate *out of* configuration m into all other configurations and the second term is the transition *into* configuration m from all other configurations m' . The probability for the defect to undergo a transition from configuration m to m' depends only on the relative energy of m with respect to the ground state. This is because once the defect overcomes the barrier between states m and m' , the probability of going into state m' does not depend on the energy of state m' , but is a fixed probability that we include in $\nu_{mm'}$.

Linearizing the exponentials in Equation (2.6) in the small stress limit and rearranging terms gives us a simpler expression for the rate,

$$\frac{dP^m}{dt} \approx \sum_{m'} \left(P^{m'} \nu_{m'm} - P^m \nu_{mm'} \right) + \beta \sum_{m'} \left(P^{m'} \nu_{m'm} \Lambda_{ij}^{m'} - P^m \nu_{mm'} \Lambda_{ij}^m \right) \sigma_{ij}. \quad (2.7)$$

For many defects including divacancies [27], the zero-stress transition rates among different orientations of a defect type are equal by symmetry, $\nu_{mm'} = \nu$. In such cases, the set of coupled equations in Equation (2.7) can be solved analytically. To do this, we separate the time-dependent part of $P^m(t)$ from the stationary part

$$P^m(t) = \frac{1}{g} + \Delta P^m e^{i\omega t}, \quad (2.8)$$

where g is the number of possible orientations m of the defect, which are equivalent in the absence of stress. We assume the same harmonic time dependence for $P^m(t)$ as the externally applied stress with the phase lag information contained in the complex amplitude ΔP^m . It is this phase lag that gives rise to the mechanical loss.

Substituting Equation (2.8) into Equation (2.7) gives a coupled set of equations involving the probability of having defects in all the orientations, which can be written in terms of a matrix equation as follows

$$\frac{i\omega \Delta P^m}{\nu} \approx \sum_{m'} (\Delta P^{m'} - \Delta P^m) + \frac{\beta}{g} \sum_{m'} (\Lambda_{ij}^{m'} - \Lambda_{ij}^m) \tilde{\sigma}_{ij} \quad (2.9)$$

In Equation (2.9), we can identify the first term as the term that causes the decay from m' to m and the second term as the driving force. In obtaining this equation, we have omitted terms that involve a product of ΔP^m and $\tilde{\sigma}_{ij}$ since both are assumed to be small.

We notice in Equation (2.9) that by Equation (2.8)

$$\sum_{m'} \Delta P^{m'} = 0 \quad (2.10)$$

due to the fact that all probabilities should add up to one. Using this identity, we easily solve Equation (2.9) for ΔP^m

$$\Delta P^m = \frac{\beta}{g^2} \frac{1 - i\frac{\omega}{g\nu}}{1 + \left(\frac{\omega}{g\nu}\right)^2} \sum_{m'} (\Lambda_{ij}^{m'} - \Lambda_{ij}^m) \tilde{\sigma}_{ij} \quad (2.11)$$

which we see indeed satisfies Equation (2.10).

In order to find the energy dissipated in one cycle of oscillation, Equation (2.5) must be integrated over a period. Keeping in mind that we should use the real parts of the terms forming the product in Equation (2.5), we find that this integral gives

$$\Delta E_{\text{cycle}} = \pi n \text{Re} \left[\tilde{\sigma}_{ij}^* \sum_m \Lambda_{ij}^m \Delta P^m \right] \quad (2.12)$$

Substituting Equation (2.11) into Equation (2.12), we have

$$\Delta E_{\text{cycle}} = \frac{\pi n \beta}{g} \frac{1}{1 + \left(\frac{\omega}{g\nu}\right)^2} \text{Re} \left[\left(i + \frac{\omega}{g\nu} \right) \tilde{\sigma}_{ij}^* \sum_m \Lambda_{ij}^m \left(\frac{1}{g} \sum_{m'} \Lambda_{kl}^{m'} - \Lambda_{kl}^m \right) \tilde{\sigma}_{kl} \right]. \quad (2.13)$$

To make the expression more symmetric, we use the following identity

$$\sum_m \sum_{m'} \Lambda_{ij}^{m'} \left(\frac{1}{g} \sum_{m''} \Lambda_{kl}^{m''} - \Lambda_{kl}^m \right) = 0. \quad (2.14)$$

Equation (2.14) can be easily seen to hold due to the interchangeability of the indices m' and m'' in the second terms. Thus, using Equation (2.12), Q^{-1} is given

by

$$Q^{-1} = n\beta \frac{\frac{\omega}{\nu g}}{1 + \left(\frac{\omega}{\nu g}\right)^2} \frac{\tilde{\sigma}_{ij}^* L_{ij;kl} \tilde{\sigma}_{kl}}{\tilde{\sigma}_{ij}^* S_{ij;kl} \tilde{\sigma}_{kl}}, \quad (2.15)$$

where $\tilde{\sigma}_{ij}^* S_{ij;kl} \tilde{\sigma}_{kl}$ is the total energy in the oscillator in the absence of loss and the four-tensor $L_{ij;kl}$ is defined as

$$L_{ij;kl} \equiv \frac{1}{g} \sum_m \Delta \Lambda_{ij}^m \Delta \Lambda_{kl}^m.$$

Here $\Delta \Lambda_{ij}^m \equiv \Lambda_{ij}^m - \frac{1}{g} \sum_{m'} \Lambda_{ij}^{m'}$ and $S_{ij;kl}$ is the standard elastic compliance four-tensor, and $L_{ij;kl}$ is an *anelastic four-tensor* sharing the symmetry of the full set of defect orientations.

To place the above result in context, it can be intuitively understood that when the stress is applied at a frequency much larger than $\nu_{mm'}$, there isn't sufficient time for defect reorientation and therefore there is little loss. If stress is applied at a lower rate, the defects reorient adiabatically, always maintaining an equilibrium distribution and thus again causing small amount of loss. The maximum loss occurs when $\omega/2\pi \approx \nu$ as shown below.

In a system with more than one type of defect, the inverse quality factors for each type add. If the transition rate ν_s associated with each type s has the same value ν , then Q^{-1} can be written as Equation (2.15) with

$$L_{ij;kl}^{tot} \equiv \sum_s \frac{n_s}{n} L_{ij;kl}^s \quad (2.16)$$

replacing $L_{ij;kl}$, where n_s is the number density for each type of defect so that $\sum_s n_s \equiv n$. Below we show how to apply Equation ((2.15) and Equation ((2.16)) to find the correct result for divacancies.

We also note here that there is a simple, exact relationship between the anelastic four-tensor and the results from experimental studies of the inverse quality factor of

a mechanical oscillator as a function of temperature, which generally show a peak when the thermally activated, and thus temperature-dependent, transition rate $\nu(T)$ corresponds to the oscillator frequency [12]. In particular, from (2.15,2.16) we have that the experimentally accessible quantity $k_B T Q^{-1}$, where k_B is Boltzmann's constant, has a maximum at precisely $\nu(T) = \omega/g$ (as discussed in the intuitive argument above) with value

$$\max(k_B T Q^{-1}) = \frac{n \tilde{\sigma}_{ij}^* L_{ij;kl}^{tot} \tilde{\sigma}_{kl}}{2 \tilde{\sigma}_{ij}^* S_{ij;kl} \tilde{\sigma}_{kl}}. \quad (2.17)$$

Ab initio determination of $L_{ij;kl}^{tot}$ thus gives a parameter-free relationship between the maximum temperature-internal friction product and the defect concentration, thereby allowing mechanical response experiments to provide a direct, parameter-free measure of absolute defect concentrations for the first time.

2.2 Application to divacancy in silicon

Divacancies are among the most prevalent defects in silicon devices. They are created during stages of device fabrication such as irradiation with dopants [12]. As seen in Figure 2.1, a divacancy in silicon consists of two neighboring atoms removed from the perfect diamond structure, leaving behind six under-coordinated nearest neighbors. The importance of the divacancy in silicon has led to its extensive study, both theoretically and experimentally[6, 23, 24, 28, 29, 30, 31].

In contrast to single vacancies, which are quite mobile and thus anneal readily, divacancies have low mobility and are among the most common stable defects in silicon at room temperature. The defect has four charge states, singly positively charged, neutral, singly and doubly negatively charged, with the singly charged defect (Si-V_2^-) playing an important role in carrier recombination [32].

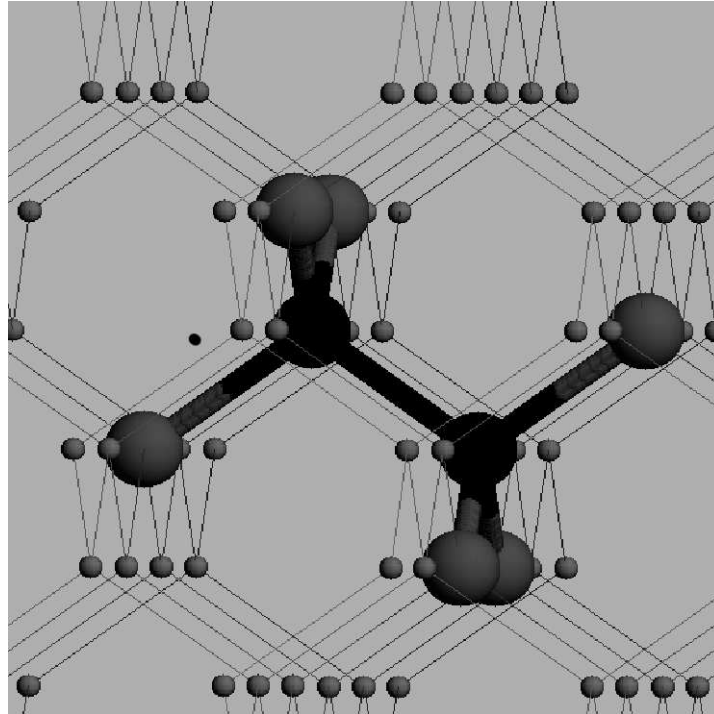


Figure 2.1: Divacancy shown along the $\langle 110 \rangle$ defect axis. The two black spheres represent the missing atoms and the gray spheres represent the silicon atoms. The large gray spheres are the six nearest neighbors that are left with dangling bonds after the divacancy is created.

Since the publication of Watkins and Corbett’s pioneering study [23], the *ab initio* determination of the precise nature of the ground-state structure of Si-V_2^- has become the subject of debate[6, 24, 25, 26]. The idealized defect has D_{3d} symmetry along the $\langle 111 \rangle$ axis connecting the sites of the neighboring vacant atoms. The defect also introduces partially filled degenerate electronic states into the gap and thus undergoes a Jahn-Teller distortion which ultimately lowers the symmetry to C_{2h} . The debate arises because two stable structures, termed *pairing* and *resonant*, with very similar energies are consistent with the C_{2h} symmetry of the defect.

Figure 2.2 shows the two competing ground-state structures as projected along the $\langle 111 \rangle$ *defect axis* connecting the sites of the two vacant atoms. The pairing configuration breaks symmetry by moving two pairs of atoms (ab and $a'b'$ in the figure) toward each other along a $\langle 110 \rangle$ *reconstruction axis* to form stronger bonds at the expense of strain energy. In the resonant structure, the same pairs of atoms move away from each other to form a less favorable bonding configuration at a nearly correspondingly lower cost in strain. The convention used in this section takes $[111]$ as the *defect axis* and $[1\bar{1}0]$ as the *bonding axis*. The ab and ac distances respectively are 2.9Å and 3.4Å in the pairing configuration, and 3.5Å and 3.2Å in the resonant configuration.

The literature reports a number of density-functional values for the energy difference $\Delta E \equiv E_{\text{pair}} - E_{\text{res}}$ between the two competing configurations: 0.0024 eV[24], ~ 0 eV[29], -0.12 eV[6], -0.18 eV (present work). The fact that these differences are all quite small and of the order of the uncertainties due to the approximate density functionals which these works employ underscores the difficulty of using total energies to resolve the ground state structure of the Si-V_2^- defect and indicates that previous studies are inconclusive. We propose instead to use the considerably

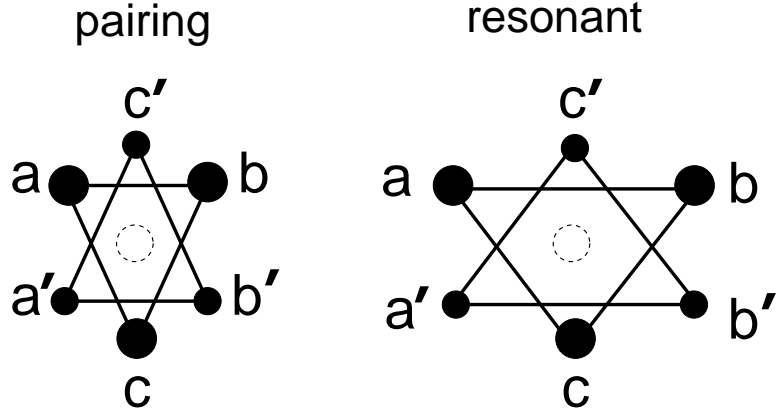


Figure 2.2: Projection of divacancy structure along $\langle 111 \rangle$ symmetry axis: missing atoms (dashed circles), atoms in plane closer to observer (larger solid circles), atoms in plane further from observer (smaller solid circles).

different activation volume tensors of the competing reconstructions as a more appropriate signature to confirm the ground state.

Experimentally, Watkins and Corbett [23] explored the activation volume tensor of the Si-V_2^- defect in depth using electron spin resonance to study thermal alignment of defect subpopulations under external $\langle 110 \rangle$ stresses. These experiments, as do also internal friction experiments, take place under conditions where $\langle 110 \rangle$ reconstruction axes have time to thermalize while $\langle 111 \rangle$ defect axes do not. This is another manifestation of the immobility of the divacancy.

Although there are four equivalent $\langle 111 \rangle$ directions a defect axis can lie in, there are only two *relative* orientations a defect axis can have with respect to a $\langle 110 \rangle$ stress. Namely, it can either be perpendicular or at an approximate angle of 35.2° to the stress. Therefore such $\langle 110 \rangle$ stresses split divacancies into two classes, which we term α and β , according to the orientation of the defect axis, with α corresponding to the defect axis being perpendicular to the stress. Within each

of these classes there is an additional degree of freedom which is the orientation of the *bond* axis, which we use to refer to the uneven side of the isosceles triangle formed by interatomic distances ab , ac and bc as defined in Figure 2.2. Thus, there is a further splitting of the energy into two distinct values, for a total of four energetically different states [33].

As thermalization occurs only among choices of reconstruction axis, the quantities which stress-alignment experiments actually access are the energy splittings within each class, ΔE_α and ΔE_β , respectively, each of which relates directly to certain linear combinations of components the defect activation-volume tensor,

$$\begin{aligned}\Delta E_\alpha &= -\frac{\sigma}{2} (\Lambda_{11} + 2\Lambda_{12} - 2\Lambda_{13} - \Lambda_{33}) \equiv -\sigma\Delta\Lambda_\alpha \\ \Delta E_\beta &= -\frac{\sigma}{2} (\Lambda_{11} - 2\Lambda_{12} + 2\Lambda_{13} - \Lambda_{33}) \equiv -\sigma\Delta\Lambda_\beta,\end{aligned}\tag{2.18}$$

where σ is the magnitude of the external $\langle 110 \rangle$ stress and Λ_{ij} are the Cartesian components of the activation volume tensor in the cubic coordinate system defined above.

2.3 Calculations and results

2.3.1 Divacancy ground state

The *ab initio* electronic structure calculations below employ the total-energy plane-wave density-functional pseudopotential approach [34] within the local spin-density approximation (LSDA) using a pseudopotential of the Kleinman-Bylander form [35] with p and d non-local corrections. The calculations expand the Kohn-Sham orbitals in a plane-wave basis set with a cutoff energy of 6 Hartrees within a cubic sixty-four atom supercell, sampling the Brillouin zone at eight k-points, reduced

to four by time reversal symmetry. Finally, we employ the analytically continued functional approach [36] to minimize the Kohn-Sham energy with respect to the electronic degrees of freedom.

We determine Λ one element at a time by applying a strain ϵ_{ij} such that $C_{ij;kl}\epsilon_{kl} \propto \delta_{ij}$, and relaxing all internal atomic coordinates. The strain which minimizes the total energy is then equal to the component Λ_{ij} . Alternatively, a single relaxation of both strain and internal coordinates could be performed, which would determine all components of Λ simultaneously. To see that the two approaches are equivalent, we present the following proof. The total energy of the system in the presence of the defect is

$$E_{\text{tot}} = \frac{1}{2}u_{ij}C_{ij;kl}u_{kl} - \Lambda_{ij}C_{ij;kl} \quad (2.19)$$

where u_{ij} is the external strain, $C_{ij;kl}$ is the elastic constants tensor and Λ_{ij} is the activation-volume tensor. The first term is the bulk strain energy and the second term is the energy associated with the strain field of the defect. In this work, for each direction, we apply an external stress so that

$$C_{ij;kl}u_{kl} = c\delta_{ij} \quad (2.20)$$

where c is a constant related to the elastic moduli.

$$E_{\text{tot}} = c \left(\frac{u_{ij}^2}{2} - \Lambda_{ij}u_{ij} \right) \quad (2.21)$$

Minimizing Equation (2.21), we obtain

$$u_{ij}^{\text{min}} = \Lambda_{ij} \quad (2.22)$$

which proves that our method is indeed equivalent to a total relaxation of the strain and internal coordinates.

For accurate calculations of defect *energy differences*, Ögüt and Chelikowsky[6] state that it is necessary to tailor supercell shape to accommodate the relaxation pattern of V_2^- . We explore supercell-size effects on calculation of the *activation-volume tensor*, Λ , using the environment-dependent interatomic potential (EDIP) for silicon[37], and find that supercell size has a much smaller effect on Λ than on energy differences. We calculated $\Delta\Lambda_\alpha$ and $\Delta\Lambda_\beta$ from (2.18) using cubic supercells of lattice constant from $2a_0$ through $6a_0$, where a_0 is the lattice constant of the “primitive” eight-atom cubic cell. Over this range of cell sizes, we observe a total change of only 12.5% (6.3%) in $\Delta\Lambda_\alpha$ ($\Delta\Lambda_\beta$), with 70% (86%) of the change occurring between $2a_0$ and $3a_0$. We thus conclude that Λ is not a particularly sensitive function of cell size and that a supercell of 64 atoms suffices to give *ab initio* values with an uncertainty on the order of 10%.

Table 2.1 summarizes our *ab initio* results for the activation volume tensors of the two candidate defect structures, and Figure 2.3 compares our predictions directly with the experimentally available linear combinations, $\Delta\Lambda_\alpha$ and $\Delta\Lambda_\beta$ [23]. Our predictions for the resonant configuration are clearly inconsistent with the measurements, whereas our results for the pairing configuration show good agreement with errors (+20% and -6% for $\Delta\Lambda_\alpha$ and $\Delta\Lambda_\beta$, respectively) consistent with supercell-convergence uncertainty we estimate above. The figure also compares our *ab initio* prediction of another linear combination of components of the activation volume tensor, $B_{33} \equiv C_{33;ij}\Lambda_{ij}$ where $C_{ij;kl}$ is the elastic constant four-tensor, with an *estimate* of this quantity from [23].

Table 2.1: Activation-volume and anelastic tensors for competing ground-state structures of singly negatively charged divacancy in silicon

$\Lambda_{\text{pair}} (\text{\AA}^3)$	$\Lambda_{\text{res}} (\text{\AA}^3)$	$L^{\text{tot}}(\text{\AA}^6)$	<i>pair</i>	<i>res</i>
$\begin{bmatrix} -11 & 18 & 1.5 \\ 18 & -11 & 1.5 \\ 1.5 & 1.5 & 10 \end{bmatrix}$	$\begin{bmatrix} 0.6 & -1.5 & 10 \\ -1.5 & 0.6 & 10 \\ 10 & 10 & -13 \end{bmatrix}$	L_{11}	100	38
		L_{12}	-50	-19
		L_{44}	293	279

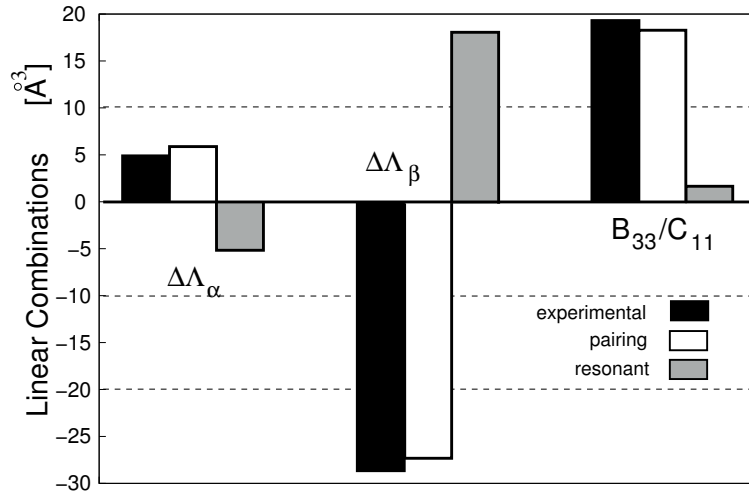


Figure 2.3: LDA results and comparison to experiment of $\Delta\Lambda_\alpha$, $\Delta\Lambda_\beta$ and B_{33} . For each data set the black bar corresponds to the experimental data, the white bar to our LDA results for the pairing configuration and the gray to those for the resonant configuration. B_{33} has been scaled by C_{11} for display purposes.

2.3.2 Q^{-1} and prediction of defect concentration

Since the defect axes do not thermalize under typical experimental conditions, each choice of defect axis must be treated as a separate *type* of defect s in Equation (2.16). Under normal sample preparation, all four distinct choices of $\langle 111 \rangle$ defect axes will occur with equal probabilities, $n_s = n/4$, resulting in an L^{tot} with cubic symmetry. The thermalizing reconstruction axes then constitute the orientations m within each type and have sufficient symmetry to ensure the result (2.15). Table 2.1 gives the three unique values of the resulting cubic anelastic four-tensor in contracted notation. This is the first *ab initio* prediction for the components of the anelastic tensor for a defect, a quantity of current research interest, particularly in the optimization of micro- and nano- electromechanical devices. (See, for example [12, 20].)

Determination of Q^{-1} from first principles presents a new way of estimating the defect concentration. To illustrate this point we give the following estimate: for a silicon device whose symmetry axes are oriented along the cartesian axes and for a purely torsional stress, our L^{tot} indicates through 2.15 that $\max(TQ^{-1})/n \approx 7.5 \times 10^{-19}$. As an example of how to use this universal quantity, we consider [38] where it was found that the maximum of Q^{-1} for a torsional Si oscillator occurs at $T \approx 48K$ due to divacancies and has a value of $Q^{-1} \approx 10^{-4}$. From this value, we estimate the defect concentration to be about $2 \times 10^{15}/\text{cm}^3$.

Conversely, if the defect concentration is well-known, we can estimate $\max(Q^{-1})$ assuming that the activation temperature for the defect orientation is known.

2.4 Conclusion

This chapter introduces *ab initio* study of the full activation-volume tensor of crystalline defects as a quantity which current approximate density-functionals give accurately and which is of direct use in making contact with mechanical response experiments, including both stress-alignment studies and measurements of macroscopic internal friction. Illustrating the power of the approach, this chapter gives the first unambiguous *ab initio* verification of the nature of the ground state of the singly negatively charged divacancy in silicon and the first parameter-free theoretical calculation of the peak internal friction associated with a point defect. This latter quantity then forms the basis for a straightforward method for determining defect concentrations via *ab initio* interpretation of macroscopic mechanical response experiments.

Bibliography

- [1] S. K. Shaikhutdinov *et al.*, Phys. Rev. Lett. **91**, 076102 (2003).
- [2] W. E. McMahon, I. G. Batyrev, J. M. Olson, and S. B. Zhang, Phys. Rev. Lett. **89**, 076103 (2002).
- [3] D. L. Carroll *et al.*, Phys. Rev. Lett. **81**, 2332 (1998).
- [4] G. Csányi, S. Ismail-Beigi, and T. A. Arias, Phys. Rev. Lett. **80**, 3984 (1998).
- [5] J. P. Goss *et al.*, Phys. Rev. B **67**, 045206 (2003).
- [6] S. Ögüt and J. Chelikowsky, Phys. Rev. B **64**, 245206 (2001).
- [7] H. Overhof and U. Gerstmann, Phys. Rev. Lett. **92**, 087602 (2004).
- [8] H. Wehrich and H. Overhof, Phys. Rev. B **54**, 4680 (1996).
- [9] F. Mauri, B. G. Pfrommer, and S. G. Louie, Phys. Rev. Lett. **79**, 2340 (1997).
- [10] Q.-M. Zhang, J.-Y. Yi, and J. Bernholc, Phys. Rev. Lett. **66**, 2633 (1991).
- [11] F. Mauri, N. Vast, and C. J. Pickard, Phys. Rev. Lett. **87**, 085506 (2001).
- [12] X. Liu, R. O. Pohl, R. S. Crandall, and K. Jones, in *Defects and Diffusion in Silicon Processing*, MRS Symposia Proceedings, edited by S. C. et al. (Materials Research Society, Pittsburgh, 1997), No. 469, p. 419.
- [13] G. Cannelli, R. Cantelli, and F. Cordero, Phys. Rev. B **38**, 7200 (1988).
- [14] C. L. Snead, Jr. and J. Bethin, Phys. Rev. B **32**, 4254 (1985).
- [15] X. Liu *et al.*, Phys. Rev. Lett. **78**, 4418 (1997).
- [16] D. Laszig, H. G. Brion, and P. Haasen, Phys. Rev. B **44**, 3695 (1991).
- [17] A. N. Cleland, M. Pophristic, and I. Ferguson, App. Phys. Lett. **79**, 2070 (2001).
- [18] R. Lifshitz, Physica B **316-317**, 397 (2002).
- [19] R. Lifshitz and M. L. Roukes, Phys. Rev. B **61**, 5600 (1999).
- [20] D. Carr *et al.*, App. Phys. Lett **75**, 920 (1999).
- [21] S. Evoy *et al.*, App. Phys. Lett. **77**, 2397 (2000).
- [22] A. B. Hutchinson *et al.*, App. Phys. Lett. **84**, (72 (2004).
- [23] G. D. Watkins and J. W. Corbett, Phys. Rev. **138**, A543 (1965).

- [24] M. Saito and A. Oshiyama, Phys. Rev. Lett. **73**, 866 (1994).
- [25] G. D. Watkins, Phys. Rev. Lett. **74**, 4353 (1995).
- [26] M. Saito and A. Oshiyama, Phys. Rev. Lett. **74**, 4354 (1995).
- [27] A. S. Nowick and B. S. Berry, *Anelastic Relaxation in Crystalline Solids* (Academic Press, New York, 1972), p. 190.
- [28] E. G. Song, E. Kim, Y. H. Lee, and Y. G. Hwang, Phys. Rev. B **48**, 1486 (1993).
- [29] M. Pesola, J. von Boehm, S. Pöykkö, and R. M. Nieminen, Phys. Rev. B **58**, 1106 (1998).
- [30] L. J. Cheng, J. C. Corelli, and G. D. W. J. W. Corbett, Phys. Rev. **152**, 761 (1966).
- [31] J. H. Svensson, B. G. Svensson, and B. Monemar, Phys. Rev. B **38**, 4192 (1988).
- [32] A. Hallén, N. Kestikalo, F. Masszi, and V. NágI, J. Appl. Phys. **79**, 3913 (1996).
- [33] L. Cheng, J. C. Corelli, J. Corbett, and G. D. Watkins, Phys. Rev. **152**, 761 (1966).
- [34] M. C. Payne *et al.*, Rev. Mod. Phys. **64**, 1045 (1992).
- [35] L. Kleinman and D. M. Bylander, Phys. Rev. Lett. **48**, 1425 (1982).
- [36] T. A. Arias, M. C. Payne, and J. D. Joannopoulos, Phys. Rev. Lett. **69**, 1077 (1992).
- [37] J. F. Justo *et al.*, Phys. Rev. B **58**, 2539 (1998).
- [38] X. Liu *et al.*, Phys. Rev. Lett. **81**, 3171 (1998).

Chapter 3

Electron-Phonon Interactions in Metallic Carbon Nanotubes

3.1 Introduction

Ever since nanotubes were discovered in 1991 [1], numerous possibilities of utilizing their conduction properties have been extensively researched [2, 3, 4, 5, 6]. In order to make use of these properties, it is necessary to have a good understanding of the behavior of the mean-free path, ℓ_e , of electrons in nanotubes, in relation to different parameters such as temperature [7]. In particular, a number of studies were recently conducted with the goal of determining the behavior of electron mean-free path as a function of the bias voltage across the nanotube [8, 9]. These studies indicate that at both high and low bias voltages, the interaction between electrons and phonons play an important role in determining the electron mean-free path in nanotubes.

In [9], electron-phonon scattering in metallic single-walled carbon nanotubes was studied experimentally in both the low and high bias regime. The corresponding mean-free paths are reported to be $\ell_{\text{low}} \approx 1.6\mu$ and $\ell_{\text{high}} \approx 10$ nm in the low and high bias regimes respectively. The theoretical treatment accompanying the experimental results in [9] points out that the only processes that contribute to scattering involve acoustic or optic phonons near the zone center and zone-edge phonons. We can see this by the following argument: At room temperature, the electrons that contribute the most to conduction reside in the states near the Fermi points and as a result scattering between Fermi points plays the most important

role in determining the electron mean-free path. As explained below in Section 3.2, there are six Fermi points in the reciprocal space of graphene. There are, however, only two *distinct* sets of such points due to the geometry of the triangular lattice. Conduction electrons can undergo scattering events with phonons that occur either within an equivalent set or between the two distinct sets. Because Fermi points within a set are equivalent, it is sufficient to study a single representative example for each of these scattering scenarios. For the case of scattering within the same subset, it is sufficient to study scattering in the vicinity of a given Fermi point. By conservation of momentum, the phonon mode involved in such a scattering event carries approximately zero momentum. Conservation of energy, on the other hand, dictates that the phonon mode be *acoustic* or *optic* depending on the energy transfer in the scattering event [10]. For the case involving two distinct subsets, we can study scattering between any two Fermi points belonging to different subsets as a representative. The momentum transfer in such an event is either \vec{k}_F or equivalently $2\vec{k}_F = \vec{k}_F + \vec{G}$, where \vec{G} is a reciprocal lattice vector. In both cases, the transferred momentum corresponds to a zone-edge phonon as seen in Figure 3.3.

Acoustic phonons are low in energy and can easily be emitted or absorbed at room temperature. They, therefore, constitute the main mechanism for scattering of electrons at low bias voltages. At high biases, electrons acquire enough energy to produce higher energy phonons. Even though these high energy phonon modes are thermally unpopulated at room temperature, the high-bias mean-free path, ℓ_{high} is determined by electron scattering from optic and zone-edge phonons through emission.

The parameters necessary for the lifetime due to acoustic phonons are well-known and have been calculated elsewhere (see references in [9]). In this chapter,

we describe the calculation of the electronic mean free path due to optic and zone-edge phonons, which are relevant in the high-bias regime. Because this and the following two chapters are deal with various nanotube properties, we give briefly review the nanotube structure in Section 3.2. Due to differences in normalization conventions between our work and [10], we repeat derivation of the electronic lifetime corresponding to optic and zone-edge phonons in Section 3.3 for the sake of completeness. In Section 3.4, we establish the background necessary to link the theory to computational results. We present our results in Section 3.5, followed by a brief set of conclusions in Section 3.6.

3.2 Electronic structure of nanotubes

A nanotube is constructed by rolling up a graphene sheet, which consists of a hexagonal network of carbon atoms, into a cylinder. There are infinitely many ways of rolling the sheet, determined by the relative angle between the hexagons and the cylinder axis. This *chiral angle* defines two indices, n and m and a nanotube with these indices is referred to as an (n, m) nanotube.

Due to the newly introduced periodicity around the circumference of the nanotube, only certain wavevectors, \vec{k} , are allowed. The component of the \vec{k} vectors along the long axis of the nanotube remains continuous, whereas the component along the circumference becomes discrete. As a result, the allowed \vec{k} 's form a set of evenly spaced lines running along the direction of the nanotube axis in the reciprocal space. The location of these lines depends on the indices of the nanotubes.

As long as the radius of the nanotube is large enough, the electronic structure can be obtained from the electronic structure of graphene together with the selection rules explained in the previous paragraph. In graphene, the valence and

conduction bands form cones whose apexes meet at the corners of the Brillouin zone. Therefore, instead of the Fermi surface, graphene has six *Fermi points* at the corners of its Brillouin zone, forming two sets of *distinct* sets. For nanotubes with indices satisfying the relation

$$n - m = 3s, \quad (3.1)$$

where s is an integer, the lines intersect all the Fermi points in the graphene reciprocal lattice, as shown in Figure 3.1(a). In this case, the nanotube is metallic and there is a crossing between the bands at the Fermi crossing in the band structure plot in Figure 3.1(a). single-walled carbon nanotubes whose indices do not satisfy Equation (3.1) are semiconductors, since the allowed \vec{k} lines fail to intersect the Fermi points. This case is illustrated in Figure 3.1(b). In this chapter, we deal only with metallic nanotubes.

For metallic nanotubes, the allowed \vec{k} lines go through the apexes of the cones thus forming two intersecting lines, $v_F|\vec{k}|$ and $-v_F|\vec{k}|$ at each Fermi point. In room temperature calculations involving conduction electrons, it is these bands that are usually considered and we shall also write our tight-binding Hamiltonian below in Section 3.4 in this two-band description.

3.3 Fermi's Golden Rule

For a general system with electron-phonon interaction, many-body Hamiltonian is

$$H = H_0 + H_{el-ph}, \quad (3.2)$$

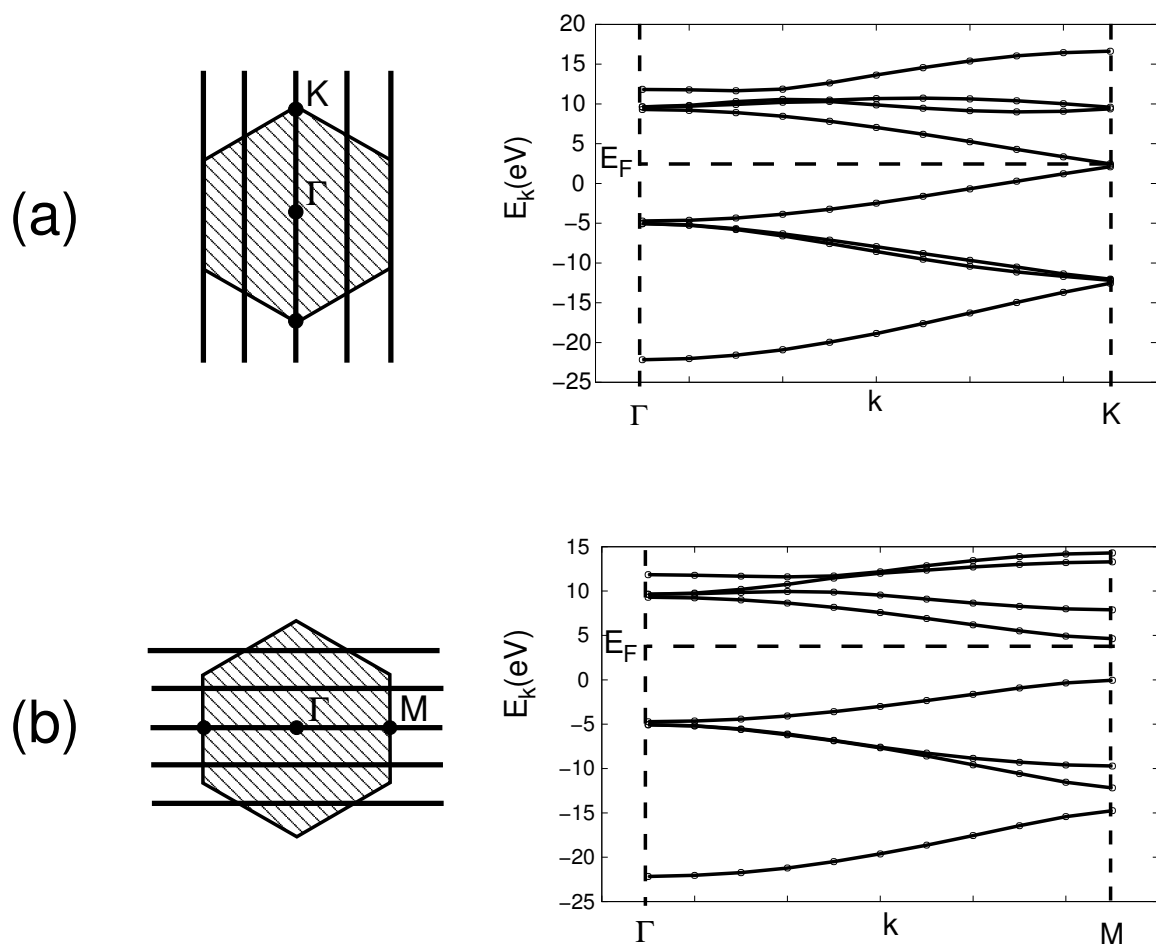


Figure 3.1: Wavevector selection rules and tight-binding band structure of (a) a metallic single-walled nanotube and (b) a semiconducting single-walled nanotube

where

$$H_0 = \sum_k \varepsilon_k c_k^\dagger c_k \quad \text{and} \quad (3.3)$$

$$H_{el-ph} = \sum_{kq} \frac{M_{kq}}{\sqrt{N_{cell}}} u_q c_{k+q}^\dagger c_k. \quad (3.4)$$

Above ε_k is the electronic energies, M_{kq} is the matrix element of the interaction, c and c^\dagger are the annihilation and creation operators that act on electronic states and u_q is the amplitude in the phonon mode labeled by wavevector q , which are related to the standard boson creation and annihilation operators through

$$u_q = \sqrt{\frac{\hbar}{2m_C\omega_q}} (a_{-q}^\dagger + a_q). \quad (3.5)$$

Note that the factor of $N_{cell}^{-1/2}$, which refers to the number of primitive unit cells in the system is included for convenience so that M_{kq} does not scale with the size of the system. Above, the phonon and electron indices q and k are understood to contain the branch and band indices respectively as well as wavevectors, \vec{q} and \vec{k} . The convention $-q$ just refers to the same branch as q but with the wavevector inverted.

Because the scattering events discussed in this chapter occur near the Fermi points, we only include in our scattering calculations, the two bands crossing at the Fermi point considered. The scattering rate can be calculated using Fermi's Golden Rule describing emission of either an optic phonon with $\vec{q} \approx 0$ or a zone-edge phonon by

$$\begin{aligned} \frac{1}{\tau} &= \frac{2\pi}{\hbar} \sum_q |\langle k, N_q = 1 | H_{el-ph} | k + q, N_q = 0 \rangle|^2 \delta(\hbar v_F(k + q) - \hbar\omega_q + \hbar v_F k) \\ &= \frac{2\pi}{\hbar} \int \frac{Ldq}{2\pi} \frac{1}{\hbar v_F} |\langle k, N_q = 1 | H_{el-ph} | k + q, N_q = 0 \rangle|^2 \delta(2\hbar v_F k + \hbar v_F q - \hbar\omega_q), \end{aligned} \quad (3.6)$$

where all wavevectors are written as scalars due to the one-dimensional nature of the nanotube. The initial state $|k + q, N_q = 0\rangle$ represents a single electron with wavevector $k + q$ and no phonons whereas the state after emission $|k, N_q = 1\rangle$ represents an electron with wavevector k and a phonon with wavevector q .

From Equation (3.2), we insert the electron-phonon Hamiltonian into Equation (3.6) to obtain

$$\frac{1}{\tau_{op,ze}} = \frac{1}{\hbar v_F \rho \omega_q^{op,ze}} |M_{kq}^{op,ze}|^2, \quad (3.7)$$

where the linear mass density in a nanotube with N_{cell} two-atom unit cells and length L is $\rho = 2m_C N_{cell}/L$. Here and throughout this chapter, we use the normalization convention where the phonon modes are normalized to the unit cell.

3.4 Calculation of matrix elements

As mentioned in Section 3.1, even though in principle phonons of all frequencies and wavevectors can interact with electrons, because of the restriction on the wavevectors in nanotubes (see Section 3.2) combined with energy and momentum conservation, the only phonons that contribute to scattering come from optic phonons with $\vec{q} = 0$ and zone-edge phonons with $\vec{q} = \vec{k}_F$ (or $\vec{q} = 2\vec{k}_F$) in the dispersion relation of graphene. While presenting our method, we shall first deal with optic phonons.

3.4.1 Optic phonons

In this section, we consider scattering processes involving optic phonons with $\vec{q} \approx 0$. Due to conservation of momentum, such an interaction can only involve initial and final electronic states that are located near the same Fermi point. We can

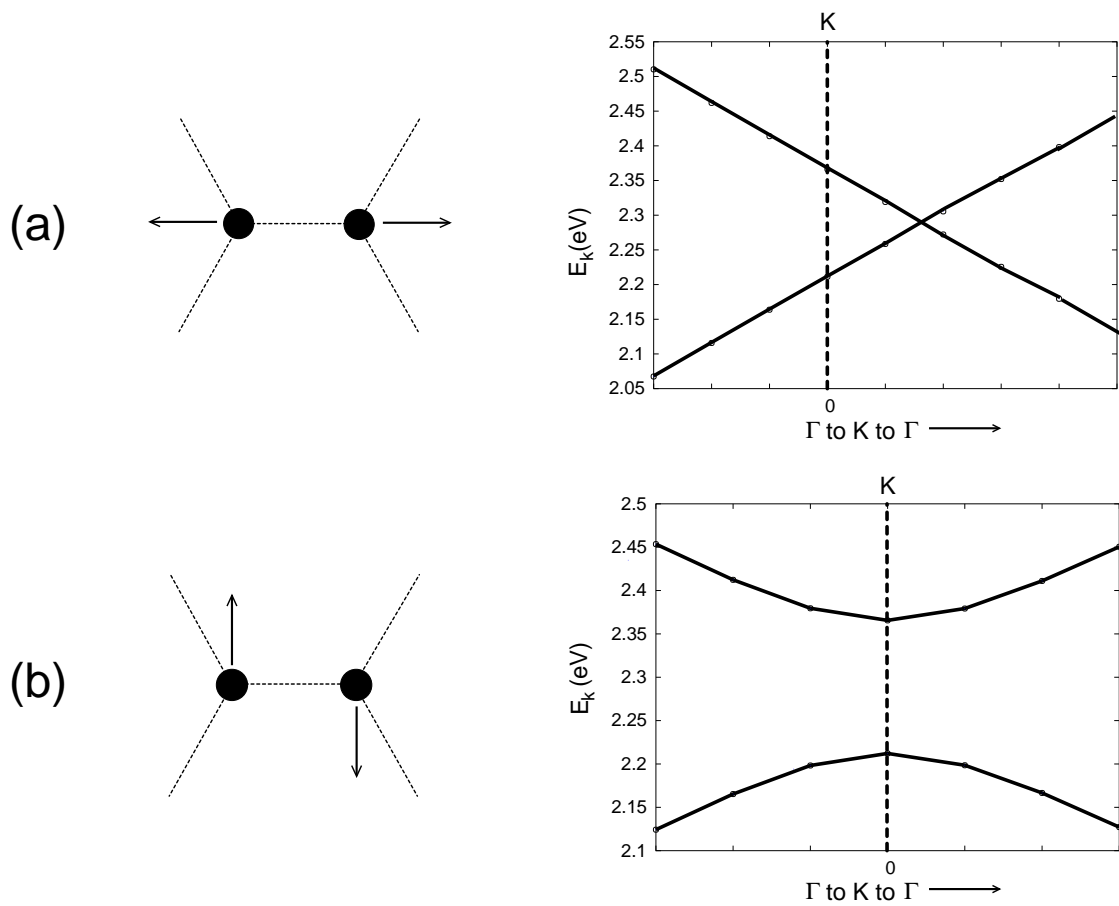


Figure 3.2: Band gap in the presence of (a) a longitudinal optic phonon and (b) a transverse optic phonon.

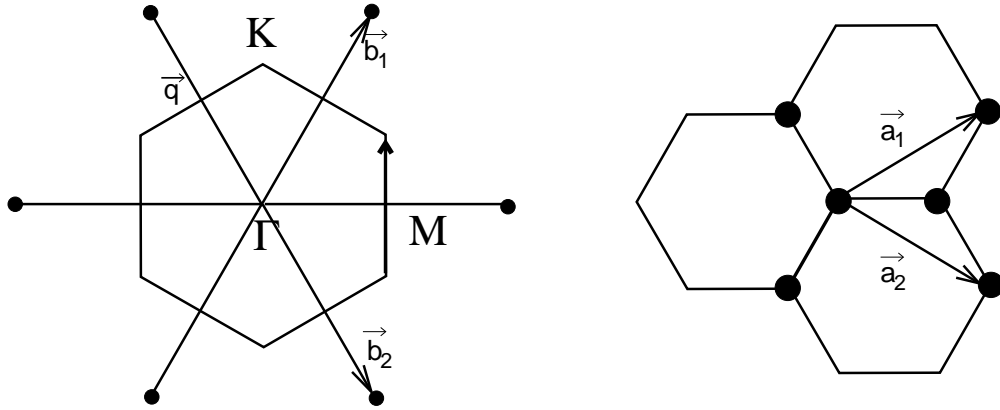


Figure 3.3: Electron momentum transfer upon emission of a zone-edge phonon(left). The transition takes place between two distinct Fermi points, with a phonon momentum of $\vec{q} = \vec{k}_F$. The reciprocal vectors are labeled \vec{b}_1 and \vec{b}_2 and the hexagonal area is the first Brillouin zone. For reference, the real space orientation corresponding to the reciprocal space picture on the left is also shown (right) with lattice vectors labeled \vec{a}_1 and \vec{a}_2 .

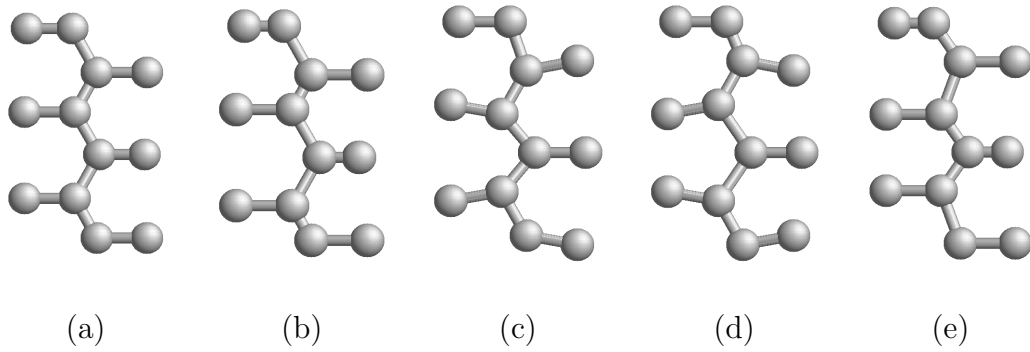


Figure 3.4: The unperturbed 12-atom graphene supercell (a) and the four in-plane zone-edge modes in the supercell (b)-(e). The displacements in the phonon modes are magnified for ease of vision.

then use the linear approximation to the bands, which causes the single-electron Hamiltonian relevant to our computations to take the form of a simple 2×2 matrix,

$$H = \begin{pmatrix} H_{kk} & H_{k,k+q} \\ H_{k+q,k} & H_{k+q,k+q} \end{pmatrix} = \begin{pmatrix} -\hbar v_F \Delta k + u_0 \epsilon - u_0 \Delta & u_0 M_{kq} \\ u_0 M_{kq}^* & \hbar v_F \Delta k + u_0 \epsilon + u_0 \Delta \end{pmatrix}, \quad (3.8)$$

where $\Delta k = k - k_F$ is the distance from the Fermi wavevector, u_0 is the phonon amplitude, $u_0 \epsilon$ is the average shift of the bands, $2u_0 \Delta$ is the difference in the shift of the bands and $u_0 M_{kq}$ is the coupling between the bands.

Above, the Fermi energy is also taken to be at zero. In Equation (3.8), the eigenenergies can be found by diagonalizing H in Equation (3.8), giving

$$E(k) = u_0 \epsilon \mp \sqrt{(\hbar v_F k + u_0 \Delta)^2 + u_0^2 |M_{kq}|^2}. \quad (3.9)$$

According to Equation (3.9), two important changes take place at each of the Fermi points: the band extrema shift by $\frac{u_0 \Delta}{\hbar v_F}$ along the allowed wavevector direction and a gap opens in the band structure, whose minimum occurs at the new Fermi point locations with magnitude $2u_0 |M_{kq}|$. This result provides a convenient way of finding the magnitude of coupling, $|M_{kq}|$,

$$|M_{kq}| = \frac{\min \Delta E}{2u_0} = \frac{1}{2} \frac{\partial(\min \Delta E)}{\partial u_0}, \quad (3.10)$$

where $\min \Delta E$ is the minimum band separation at any k near k_F . The second equality holds as long as u_0 remains small.

In order to evaluate this derivative, we use a finite-difference derivative scheme. We first identify the displacement pattern that is relevant to a given phonon mode and displace the atoms following the distortion pattern using

$$\vec{R}(\alpha) = \vec{R}_0 + \alpha \vec{\eta}_k, \quad (3.11)$$

where $\vec{R}(\alpha)$ is a $3N$ -dimensional vector containing the new locations of the atoms and α is the small parameter that multiplies the displacement pattern $\vec{\eta}_k$ of mode k . Finally, we calculate the derivative using

$$\frac{\partial \min \Delta E}{\partial u_0} \approx \frac{\min \Delta E \Big|_{\alpha} - \min \Delta E \Big|_{\alpha=0}}{\alpha}. \quad (3.12)$$

For the optic phonon modes, we conduct our calculations by constructing a two-atom, periodic unit cell representing graphene with appropriate lattice vectors (See Figure 3.3). Optic phonons are defined as those phonon modes where every atom moves 180° out of phase from its three neighbors. Here and in the rest of this chapter, we restrict ourselves to in-plane modes because out-of-plane modes do not couple with electrons traversing the length of the nanotube.

In the two-atom unit cell of graphene, there are two distinct in-plane optic modes. These modes are illustrated in Figure 3.2 on the left. In the top panel, we show a *longitudinal* optic mode, where the two atoms move in opposite direction *along* the C-C bond. In the bottom panel, we show a *transverse* optic phonon mode, where the two atoms move *perpendicular* to this bond. We observe very diverse results for these two modes, as Section 3.5 discusses.

While calculating the finite-difference derivative in Equation (3.12), care must be taken regarding the normalization of the phonon mode, $\vec{\eta}_k$. The results that we present in Section 3.5 were calculated for the following displacements:

$$\eta_0^{long} = \frac{1}{\sqrt{2}} \begin{pmatrix} 1 \\ 0 \\ -1 \\ 0 \end{pmatrix} \quad \text{and} \quad \eta_0^{trans} = \frac{1}{\sqrt{2}} \begin{pmatrix} 0 \\ 1 \\ 0 \\ -1 \end{pmatrix} \quad (3.13)$$

where the vectors are arranged so that the first entry corresponds to the displacement of the first atom along the bonds, the second entry corresponds to the

displacement of the first atom perpendicular to the bonds and the third and fourth entries give the corresponding information for the second atom.

After definition of the displacement patterns for the two modes, we choose a value of 0.006 \AA for α and calculate the finite-difference derivative. To check that the derivative is independent of the value of α , the calculations were repeated for an α of 0.002 \AA and was found to differ only by about 1%.

3.4.2 Zone-edge phonons

The treatment of zone-edge phonons is very similar to the optic phonons. In this case, however, there are four bands involved in the interaction because due to conservation of momentum, the phonon exchange occurs between two distinct Fermi points. As a result, the Hamiltonian we need to consider takes the form of the following 4×4 matrix,

$$H = \begin{pmatrix} H_1 & 0 \\ 0 & H_2 \end{pmatrix}, \quad (3.14)$$

where H_1 and H_2 are

$$H_1 = \begin{pmatrix} -\hbar v_F \Delta k_1 + u_0 \epsilon - u_0 \Delta & u_0 M_{kq} \\ u_0 M_{kq}^* & \hbar v_F \Delta k_2 + u_0 \epsilon + u_0 \Delta \end{pmatrix} \quad (3.15)$$

and

$$H_2 = \begin{pmatrix} -\hbar v_F \Delta k_2 + u_0 \epsilon - u_0 \Delta & u_0 M_{kq} \\ u_0 M_{kq}^* & \hbar v_F \Delta k_1 + u_0 \epsilon + u_0 \Delta \end{pmatrix}. \quad (3.16)$$

In Equation (3.15) and Equation (3.16), Δk_1 and Δk_2 are measured from Fermi points and, due to conservation of momentum, satisfy $\Delta k_1 = \Delta k_2 = \Delta k$. All the other symbols have the same meaning as in Equation (3.14). Note that above, energy and momentum conservation dictate that, in contrast to the optic and

acoustic phonon case, there is no interaction within the same Fermi point and the Hamiltonian thus takes a block-diagonal form.

Each block in Equation (3.14) is diagonalized separately in the same way as the matrix in Equation (3.8) and yields the same result for the coupling as in Equation (3.10) for each of the Fermi points separately. We therefore proceed using the same method as described above for the optic phonons.

Unlike the optic and acoustic modes, zone-edge phonons have a non-zero wavevector. As a result, the displacement patterns associated with these modes are more complicated and have larger periodicity than the two-atom unit cell. We must therefore use a *supercell* in our calculations that is large enough to accommodate these longer wavelength phonon modes. We find that a 12-atom supercell, shown in Figure 3.4(a), is sufficient to accommodate the zone-edge phonons. Following the same logic as for the optic modes, although there are six branches in the dispersion relation of graphene, we restrict our calculations to only the four in-plane modes. We diagonalize the supercell *force constant matrix*, K_{ij} , in the space of the eigenmodes that is invariant under the translation operation affected by the wavevector, \vec{q} . The eigenmodes obtained in this way for the zone-edge modes are given in the Bloch representation as

$$\eta_{qin} = \frac{1}{\sqrt{N_{cell}}} e^{i\vec{q}\cdot\vec{R}_n} \tilde{\eta}_{qi}, \quad (3.17)$$

where η_{qin} is the i th element of the eigenmode in the n th unit cell, \vec{R}_n are the unit cell lattice vectors, that run over the entire system that fit in our supercell, N_{cell} is the number of unit cells in the system and $\tilde{\eta}_{qi}$ is the i th element of the cell-periodic part of the Bloch modes normalized to unity in the unit cell. We found these to

be

$$\tilde{\eta}_1 = \frac{1}{2} \begin{pmatrix} 1 \\ i \\ -1 \\ i \end{pmatrix}, \quad \tilde{\eta}_2 = \frac{1}{2} \begin{pmatrix} 1 \\ i \\ 1 \\ -i \end{pmatrix}, \quad \tilde{\eta}_3 = \frac{1}{2} \begin{pmatrix} 1 \\ -i \\ 1 \\ i \end{pmatrix} \quad \text{and} \quad \tilde{\eta}_4 = \frac{1}{2} \begin{pmatrix} 1 \\ -i \\ -1 \\ -i \end{pmatrix} \quad (3.18)$$

Note that the above choices of normalization, particularly the factor of N_{cell} , are ultimately set by the canonical commutation relations for the operators in Equation (3.5).

Even though the complex $\vec{\eta}_q$ are valid eigenstates of K_{ij} , when performing computations, the atoms can only be displaced by real distances. In order to handle this issue, we note that from the definition of matrix element m in Equation (3.15) and Equation (3.16) with η_{in} given in Equation (3.17), the matrix element, M_{kq} , in Equations (3.15)

$$M_{kq} = \frac{\partial H_{kq}}{\partial u_q}, \quad (3.19)$$

where from Equation (3.8), $H_{kq} = \langle k, N_q = 1 | H_{el-ph}^{supercell} | k + q, N_q = 0 \rangle$ is calculated in the supercell. Since the electron operators and the wavefunctions are normalized in the same way to produce a single electron over the entire system, there are no normalization issues to be considered for the electronic part of the calculation.

In order to see the effect of having a complex eigenmode, we switch to a representation of the derivative with respect to $\tilde{\eta}_q$ by means of a chain rule:

$$M_{kq} = \sum_i \eta_{qi} \frac{\partial H_{kq}}{\partial x_i} = \sum_i \left\{ \text{Re}(\tilde{\eta}_{qi} e^{iqR_i}) \frac{\partial H_{kq}}{\partial x_i} + i \text{Im}(\tilde{\eta}_{qi} e^{iqR_i}) \frac{\partial H_{kq}}{\partial x_i} \right\}, \quad (3.20)$$

where i runs over the atoms and R_i over the unit cells in the crystal.

Due to the translational symmetry of the crystal, the second term in Equation (3.20), which contains the imaginary part of the phonon mode turns out to

be $(-i)$ times the term that contains the real part. We thus have

$$M_{kq} = 2 \sum_i \text{Re}(\eta_{qi}) \frac{\partial H_{kq}}{\partial x_i}, \quad (3.21)$$

This result implies that we may construct the displacement in our supercell by just taking the real part of the eigenmodes given in Equation (3.17) and multiplying the result by a factor of 2. Figure 3.4(b)-(e) illustrates the displacements that we construct by taking the real parts of the four modes corresponding to $\vec{q} = \vec{k}_F$. We also show the unperturbed supercell configuration on the left hand side for comparison in Figure 3.4(a).

3.5 Results

Figure 3.2 shows the displacement pattern in an optic mode on the left-hand side and the two bands crossing at the Fermi level in the absence of the perturbing mode on the right hand side. For the longitudinal mode, displayed on top, we observe only a shift of the Fermi point to the right. According to Equation (3.9), this result indicates that $M_{kq} = 0$. In other words, the longitudinal optic phonon mode does not mix the two bands at the Fermi point.

The transverse mode, on the other hand, unmistakably causes a band gap as is shown in Figure 3.2, with a gap opening of $\Delta E = 1.08 \times 10^{-1}$ eV for $\alpha = 0.006 \text{ \AA}$. We also observe that the transverse mode does not cause the Fermi point to shift. For this mode, then, $\Delta = 0$ and $M_{kq}^{op} = \frac{\min \Delta E}{2\alpha} = 9.02 \text{ eV/\AA}$. The longitudinal and transverse modes depicted in Figure 3.2 constitute two extreme cases. Any mode that is a linear combination of these two modes will necessarily exhibit both a shift and a gap. This interesting result was also independently observed and explained in [11].

Table 3.1: Results from tight binding calculations. We present band gaps and coupling matrix element, M_{kq} corresponding to each of the two optic and four zone-edge phonons.

Phonon mode	E_{gap} ($\times 10^{-1}$ eV)	M_{kq} (eV/Å)
Longitudinal optic	0	0
Transverse optic	1.08	9.02
Zone-edge (mode 1)	0.77	12.07
Zone-edge (mode 2)	≈ 0	0
Zone-edge (mode 3)	≈ 0	0
Zone-edge (mode 4)	≈ 0	0

Only one of the four modes that have been identified as the zone-edge phonon modes causes a significant band gap opening of $\min \Delta E = 7.70 \times 10^{-2}$ eV for $\alpha = 0.006$ Å so that $M_{kq}^{op} = \frac{\min \Delta E}{\alpha} = 12.07$ eV/Å. The results for the band gap, $E_{gap} = \min \Delta E$ and the coupling M_{kq} at the Fermi point for all phonon modes are summarized in Table 3.1.

Using our results for $D_{kq}^{ze,op}$ from Table 3.1 together with Equation (3.7), we calculate the lifetime of optic and zone-edge phonons as $\tau^{op} = 5.42 \times 10^{-13}$ sec and $\tau^{ze} = 2.55 \times 10^{-13}$ sec, which give mean-free paths of $\ell^{ze} \approx 204$ nm and $\ell^{op} \approx 434$ nm respectively. The total mean-free path at high voltage bias is then

$$\ell = \left(\frac{1}{\ell^{op}} + \frac{1}{\ell^{ze}} \right)^{-1} \approx 139 \text{ nm} \quad (3.22)$$

3.6 Conclusion

In conclusion, we calculated the coupling parameter for electron-phonon interaction in metallic carbon nanotubes within the tight-binding framework (see Chapter 1) using the parameterization in [12]. Our results show that among the phonon modes involved in the scattering, only the transverse optic mode and one of the four zone-edge phonon modes ($\tilde{\eta}_1$) are found to cause a band gap at the Fermi point. Using our band gap results for the atomic displacements in the relevant phonon modes described in Section 3.4, the low-bias electronic mean-free path, ℓ_{low} , was calculated to be ≈ 139 nm. This value is considerably large in comparison to the experimental value of ≈ 10 nm, however being much smaller than the low bias mean-free path involving of only $\approx 2.4 \mu\text{m}$ calculated in [10], it indicates that optic and zone-edge phonons play an important role in determining the mean free path for high bias voltages, reducing it considerably in comparison to the acoustic phonons.

The results presented in this chapter are also different from the published results in [9]. The discrepancy stems from two sources. The first is an error in [9] in calculating the mass density, ρ . The second is a mismatch between the phonon mode used in our computational work and the theoretical work in [9]. As a result, the total mean-free path that we quote in our work should be about $\frac{1}{3}$ of the mean-free in [9]. With this discrepancy accounted for, there is still a difference of approximately 35% between the final total ℓ_e in [9] and this work. The most likely cause of this discrepancy is a difference in the constants used in the two works such as the frequencies of the modes involved.

Bibliography

- [1] S. Iijima, Nature **354**, 56 (1991).
- [2] A. Bachtold *et al.*, Phys. Rev. Lett. **84**, 6082 (2000).
- [3] P. G. Collins *et al.*, Phys. Rev. Lett. **86**, 3128 (2001).
- [4] A. K. Sood and S. Ghosh, Phys. Rev. Lett. **93**, 086601 (2004).
- [5] R. D. Antonov and A. T. Johnson, Phys. Rev. Lett. **83**, 3274 (1999).
- [6] M. Menon, A. N. Andriotis, and D. Srivastava, Phys. Rev. Lett. **91**, 145501 (2003).
- [7] C. Berger, Y. Yi, Z. L. Wang, and W. A. de Heer, Appl. Phys. A **74**, 363 (2002).
- [8] Z. Yao, C. L. Kane, and C. Dekker, Phys. Rev. Lett. **84**, 2941 (2000).
- [9] J.-Y. Park *et al.*, Nano Lett **4**, 517 (2004).
- [10] S. Braig, Ph.D. thesis, Cornell University, 2005.
- [11] O. Dubay and G. Kresse, Phys Rev B **67**, 035401 (2003).
- [12] L. Goodwin, J. Phys. Condens. Matter **3**, 3869 (1991).

Chapter 4

Mechanical loss due to phonon-phonon interactions in suspended carbon nanotubes

4.1 Introduction

Mechanical dissipation can be a result of either *intrinsic* or *extrinsic* sources of loss. Mechanisms such as air friction, imperfections in clamping, extra material such as photoresist left over from device fabrication, point defects, and dislocations are *extrinsic* and can be reduced by employing techniques such as annealing, improving contacts or placing the device in vacuum. In contrast, loss mechanisms such as electron-electron, electron-phonon and phonon-phonon interactions are *intrinsic* and their presence in any system is unavoidable. Intrinsic loss mechanisms thus place an upper bound to the value of the quality factor for a given material.

Recently, a considerable amount of experimental effort has gone into fabricating nano-electromechanical devices (NEMS) using carbon nanotubes, whose small size and extraordinary electrical and mechanical properties offer many possibilities in device technology. One recent experimental work reports the excitation and detection of oscillations in a suspended carbon nanotube which is capacitatively excited [1]. In this work and others [2, 3], the quality factors of carbon nanotube devices have consistently been reported to be lower than 1000, in stark contrast with large quality factors that have been observed in other NEMS and MEMS devices [4], which can be as high as 10^7 [5]. In order to determine the cause of

the relatively low quality factor observed in nanotube oscillators, it is important to understand the contribution of the intrinsic loss mechanisms since they place an upper bound on the quality factor. In this chapter, we explore one of these loss mechanisms, namely phonon-phonon interactions with application to the suspended nanotubes described in [1], although our results can also be applied to nanotube cantilevers as well.

In a nanotube that is excited at one of its resonant frequencies, that resonance can be described as a mode that has been athermally populated with a large number of phonons. Due to anharmonicity, the phonons in the main phonon mode interact with the thermally excited phonons and lose energy. The description of the mechanism through which energy is lost out of the main vibration mode depends on how the mean-free path of the thermal phonons, ℓ_{th} compare with the wavelength, λ of the driven mode. The treatment of the case when $\ell_{th} \ll \lambda$ was first considered by Akhieser in 1939 in the context of solids [6] and is discussed in Section 4.2.

In the case of large thermal wavelength with $\ell_{th} \sim \lambda$, the thermal phonons cause the driven mode to lose energy through ballistic scattering processes. This limit was first studied by Landau and R umer in 1937 in the context of solids [7]. In Section 4.3, we derive the Q^{-1} for a nanotube using linear response theory. We consider three-phonon processes in a nanotube with *slack*, a common occurrence in the fabrication of suspended nanotubes, and also four-phonon processes, which are the lowest order scattering events allowed in a straight nanotube due to symmetry.

In Section 4.4, we explain our computational methods and present our results in Section 4.5. We conclude this chapter with a discussion briefly exploring the classical limit of our quantum mechanical results.

4.2 Akhieser Limit ($\lambda \gg \ell_{ph}$)

If the wavelength λ of the perturbing phonon mode is much longer than the mean free path ℓ_{ph} of the thermal phonons, the thermal phonons see an essentially uniform strain during their lifetime. Due to anharmonic effects, this strain modifies the thermal phonon frequencies, disturbing the local equilibrium phonon distribution. Thermal phonons then redistribute through a relaxation process, readjusting to the new equilibrium distribution, causing dissipation of heat. Phonon lifetimes in this limit were first studied by Akhieser in 1939 [6]. Here, we derive Q^{-1} in this limit for a nanotube that has a built-in slack and is driven by a long-wavelength excitation.

In the Akhieser limit, the derivation involves the time evolution of the thermal phonon distribution. The energy lost per cycle to all phonon modes q is

$$\Delta E = \oint dt \int_0^L dx \int \frac{dq}{2\pi} \hbar \omega_q(x, t) \frac{d}{dt} (N_q(x, t) - N_q^{eq}(x, t)), \quad (4.1)$$

where q is the combined wavevector and branch index and $\int dq$ is understood as integral over the wavevector and a sum over the phonon branches. In Equation (4.1), $N_q(x, t)$ is the local, instantaneous distribution of phonons of wavevector and branch q and $N_q^{eq}(x, t)$ is the local *equilibrium* distribution *in the presence* of the driven phonon, and $\omega_q(x, t)$ is the frequency of the thermal phonon at point x along the tube with wavevector q at time t . Note that because the mean-free path of mode q is small compared to the wavelength q of the driven mode, the thermal modes q experience the driven mode as just a local radius of curvature, $\rho(x, t)$. Thus, we may write $N_q^{eq}(x, t) = N_q^{eq}(\rho(x, t))$.

Expanding $\omega_q(x, t)$ around its value in a straight tube, we find

$$\omega_q(x, t) = \bar{\omega}_q + \gamma_q \rho^2(x, t) \quad (4.2)$$

where the expansion parameter $\rho(x, t)$ is the local curvature at time t and γ_q is a q -dependent expansion coefficient that behaves like a Grüneisen constant. By symmetry of the nanotube, the term that is linear in $\rho(x, t)$ is absent from the above equation (Section 4.3.4).

The time dependent local curvature $\rho(x, t)$ can be decomposed into the static part, which is the curvature due to the original shape of the nanotube and a time-dependent part curvature imposed by the driven oscillation. Then

$$\begin{aligned}\rho^2(x, t) &= \left\{ \text{Re} \left[\rho_0(x) + \tilde{\rho}(x)e^{i\omega t} \right] \right\}^2 \\ &\approx \rho_0^2(x) \left[1 + \frac{2}{\rho_0(x)} \text{Re} \left(\tilde{\rho}(x)e^{i\omega t} \right) \right],\end{aligned}\quad (4.3)$$

where the last line is an approximation in the limit where the amplitude of the time-dependent part of the curvature, $\tilde{\rho}(x)$ is smaller than $\rho_0(x)$.

Assuming a constant relaxation rate ν , the instantaneous phonon distribution $N_q(x, t)$ obeys

$$\frac{dN_q(x, t)}{dt} = -\nu \left[N_q(x, t) - N_q^{eq}(x, t) \right], \quad (4.4)$$

where ν will be determined later.

Expanding also $N_q^{eq}(x, t)$ for small $\rho(x, t)$, we have

$$N_q^{eq}(x, t) = \frac{1}{e^{\beta\hbar\omega_q(x, t)} - 1} \approx \bar{N}_q^{eq} - (\bar{N}_q^{eq})^2 e^{\beta\hbar\bar{\omega}_q^{eq}} \beta\hbar\gamma_q \rho^2(x, t), \quad (4.5)$$

where \bar{N}_q^{eq} and $\bar{\omega}_q^{eq}$ are the equilibrium distribution and equilibrium frequency of phonon mode q in the absence of both the slack profile and the driving force.

On the other hand, within the linear response framework, we expect $N_q(x, t)$ to have the following form

$$\begin{aligned}N_q(x, t) &= N_q^{eq}(x) + \text{Re} \left[\tilde{N}_q(x, t)e^{i\omega t} \right] \\ &\approx \bar{N}_q^{eq} - (\bar{N}_q^{eq})^2 e^{\beta\hbar\bar{\omega}_q^{eq}} \beta\hbar\gamma_q \rho_0^m(x) + \text{Re} \left[\tilde{N}_q(x, t)e^{i\omega t} \right]\end{aligned}\quad (4.6)$$

where $N_q^{eq}(x)$ is the equilibrium distribution when the nanotube is in the slack profile. The time derivative of $N_q(x, t)$ is then

$$\frac{d}{dt} \text{Re} \left[N_q^{eq}(x) + \tilde{N}_q(x) e^{i\omega t} \right] = \text{Re} \left[i\omega \tilde{N}_q(x) e^{i\omega t} \right]. \quad (4.7)$$

Substituting Equations (4.3), (4.5), (4.7) and (4.17) into Equation (4.4) yields

$$\text{Re} \left[(i\omega + \nu) \tilde{N}_q(x) e^{i\omega t} \right] = 2\nu\beta\hbar\gamma_q\rho_0(x) e^{\beta\hbar\bar{\omega}_q^{eq}} (\bar{N}_q^{eq})^2 \text{Re} \left[\tilde{\rho}(x) e^{i\omega t} \right]. \quad (4.8)$$

Since the complex representation of time dependence carries an arbitrary phase, we can choose not only the real parts but also the imaginary parts the two sides to be equal. We then have

$$\tilde{N}_q(x) = 2 \frac{\nu}{i\omega + \nu} (\bar{n}_q^{eq})^2 e^{\beta\hbar\bar{\omega}_q^{eq}} \beta\hbar\gamma_q\rho_0(x) \tilde{\rho}(x) \quad (4.9)$$

Substituting all of the information we have gained so far into Equation (4.1), we obtain

$$\begin{aligned} \Delta E = -\hbar\omega \oint dt \int dx \int \frac{dq}{2\pi} \left[\bar{\omega}_q + \gamma_q \rho_0^2(x) \left(1 + \frac{2}{\rho_0(x)} \text{Re} \left[\tilde{\rho}(x) e^{i\omega t} \right] \right) \right] \\ \times \cos \omega t \text{Im} \tilde{N}_q \end{aligned} \quad (4.10)$$

Upon performing the time integration, first and second terms then disappear and we are left with

$$\begin{aligned} \Delta E &= -2\hbar\pi \int dx \int \frac{dq}{2\pi} \gamma_q \rho_0(x) \tilde{\rho}(x) \text{Im}(\tilde{N}_q(x)) \\ &= \frac{\hbar^2 \pi m^2 \nu \beta \omega}{\nu^2 + \omega^2} \int dx \rho_0^2(x) \tilde{\rho}^2(x) \int \frac{dq}{2\pi} (\gamma_q \bar{N}_q^{eq})^2. \end{aligned} \quad (4.11)$$

The total energy in the nanotube during a cycle of oscillation associated with the curvature due to the phonon mode is,

$$\begin{aligned} \Delta U_{\text{bend}} &= \frac{F}{2} \int_0^L [(\rho_0(x) + \tilde{\rho}(x))^2 - \rho_0^2(x)] dx \\ &= \frac{F}{2} \int_0^L [\tilde{\rho}^2(x) + 2\tilde{\rho}(x)\rho_0(x)] dx, \end{aligned} \quad (4.12)$$

where F is the bending rigidity of the nanotube.

Finally, using Equation (4.11) and Equation (4.12), we arrive at Q^{-1} for a nanotube with slack in the Akhieser limit:

$$Q^{-1} = 2\beta \frac{\nu\omega}{\nu^2 + \omega^2} \frac{\int dx \rho_0^2(x) \tilde{\rho}^2(x)}{\frac{F}{2} \int dx \tilde{\rho}^2(x)} \int \frac{dq}{2\pi} (\hbar\gamma_q N^{\text{eq}}(\bar{\omega}_q))^2 e^{\beta\hbar\bar{\omega}_q} \quad (4.13)$$

where F is the bending rigidity of the nanotube. The Lorentzian in Equation (4.13) leads to the result that the maximum loss is achieved when the thermal phonon relaxation rate ν is equal to acoustic phonon frequency ω . Even though, ν cannot be determined *a priori*, setting $\nu = \omega$ places an upper bound on the loss. The third term is a geometric factor involving the curvature of the acoustic phonon mode $\tilde{\rho}(x)$ and the curvature of the equilibrium slack profile $\rho_0(x)$.

The final term in Equation (4.13) involves the ‘‘Grüneisen constant’’ γ_q and the thermal phonon population $N^{\text{eq}}(\bar{\omega}_q)$. This term plays an important part in determining the magnitude of the loss. Most notably, the factor of thermal occupation exponentially damps out contributions to loss from high frequency phonon modes. The calculation of γ_q is explained in Section 4.4.

According to [8] and [9] the phonon mean-free path across a range of temperatures in nanotubes is estimated to be very large, around 100nm to $1\mu\text{m}$, which is comparable to the typical size of devices used in the present day experiments. The Akhieser limit, therefore, is not suitable. Although we do not present results for this limit, we include the derivation in this chapter for possible future applications involving larger nanotubes. For the present devices, a more appropriate limit is the Landau-Rümer limit, where the mean free path is much smaller than the system size.

4.3 Landau-Rümer Limit ($\lambda \ll \ell_{ph}$)

In the limit in which the mean free path of the thermal phonons is much longer than the wavelength of the acoustic phonon mode, we view the thermal phonons as undergoing ballistic scattering from the acoustic phonon mode thereby decreasing the energy in the acoustic mode. In this limit, we describe the scattering by an interaction Hamiltonian that involves three-, four- or higher order phonon processes. We then derive the Feynman rules for calculating Q^{-1} in the linear response framework.

4.3.1 Phonon Green's functions

In calculating the linear response of a nanotube under the action of a driving force we employ the Green's function technique. To facilitate derivation of expressions in later sections, we give a brief review of this technique in this section.

In the presence of phonon-phonon interactions, the well-known harmonic approximation for a crystal needs to be extended to include higher order terms. The energy expansion in terms of atomic displacements from their equilibrium positions is

$$\mathcal{U} = \mathcal{U}_0 + \frac{1}{2!} \frac{\partial^2 \mathcal{U}}{\partial x_i \partial x_j} x_i x_j + \frac{1}{3!} \frac{\partial^3 \mathcal{U}}{\partial x_i \partial x_j \partial x_k} x_i x_j x_k + \frac{1}{4!} \frac{\partial^4 \mathcal{U}}{\partial x_i \partial x_j \partial x_k \partial x_l} x_i x_j x_k x_l + \dots, \quad (4.14)$$

where indices i include both the atom index going over the N atoms in the crystal and the Cartesian coordinate index for each atom, so that $i = 1, 2, \dots, 3N$. The derivatives are evaluated at the equilibrium positions of the atoms and the first-order term is zero since the equilibrium configuration is a minimum of energy. In this equation and in the rest of this chapter, we employ the repeated-index summa-

tion convention unless the sum is explicitly written for clarity. The displacements, x_i , in Equation (4.14) can be written in terms of amplitudes in phonon modes as

$$x_i = \eta_{iq} u_q \quad (4.15)$$

where η_{iq} is the displacement in the coordinate i in phonon mode q with amplitude u_q , and by our convention, there is an implicit sum over q . Here, q as in the previous section, refers to both the wavevector and the branch index of the phonon. Using Equation (4.15), we make a change of variables and the n th order term in Equation (4.14) becomes

$$\frac{1}{\sigma!} \frac{\partial^\sigma \mathcal{U}}{\partial x_{i_1} \dots \partial x_{i_\sigma}} x_{i_1} \dots x_{i_\sigma} = \frac{1}{\sigma!} \frac{\partial^\sigma \mathcal{U}}{\partial u_{q_1} \dots \partial u_{q_\sigma}} u_{q_1} \dots u_{q_\sigma}. \quad (4.16)$$

Next, the retarded Green's function $D_q(t, t')$ is defined so that the response in a mode due to a generalized force $f_q(t)$ on that mode coordinate is,

$$u_q(t) = \int D_q(t, t') f_q(t') dt', \quad (4.17)$$

where by the first-order time-dependent perturbation theory, the Green's function $D_q(t, t')$ is

$$D_q(t - t') = \frac{-i}{\hbar} \theta(t - t') \langle [u_q(t), u_{-q}(t')] \rangle_{\beta H}, \quad (4.18)$$

the so-called *retarded Green's function*, where $\langle \dots \rangle_{\beta H}$ refers to a thermodynamic average over the eigenstates of the full time-independent Hamiltonian, H , and $\theta(t - t')$ is the standard theta or *step* function ensuring that $t > t'$.

Defining Fourier transforms as

$$\hat{g}(\omega) = \int_{-\infty}^{\infty} e^{i\omega t} g(t) dt \quad (4.19)$$

so that a real periodic signal is written

$$f(t) = \text{Re} \hat{f} e^{-i\omega t}, \quad (4.20)$$

for any function $g(t)$, Equation (4.17) takes the familiar form

$$\hat{u}_q(\omega) = \hat{D}_q(\omega)\hat{f}_q(\omega). \quad (4.21)$$

in the frequency domain. At finite temperature, the Green's function can be computed by using the well-known mathematical convention of imaginary time, $\tau = it/\hbar$:

$$\mathcal{D}_q(\tau) \equiv \langle T_\tau u_q(\tau) u_{-q}(0) \rangle_{\beta H}, \quad (4.22)$$

where T_τ is the imaginary time-ordering operator. In the imaginary time description, we use a causal Green's function since in the frequency domain, the real-time retarded Green's function is related to the imaginary-time causal Green's function by a simple analytic continuation.

Because imaginary time boson functions are periodic with period β , we can define the Fourier transform of any such function as

$$\hat{\mathcal{D}}_q(\omega_n) = \int_0^\beta d\tau e^{i\hbar\omega_n\tau} \mathcal{D}_q(\tau), \quad (4.23)$$

for the discrete set $\omega_n = \frac{2n\pi}{\hbar\beta}$, known as the *Matsubara frequencies*[10]. The inverse transform is then given by a sum over these frequencies as

$$\mathcal{D}_q(\tau) = \frac{1}{\beta} \sum_n e^{-i\hbar\omega_n\tau} \hat{\mathcal{D}}_q(\omega_n). \quad (4.24)$$

Inserting complete sets of states into the definitions (4.18), (4.19), and (4.21), (4.22) respectively, we obtain the spectral representations

$$\hat{D}(\omega) = \sum_{n,m} \frac{1}{Z} |\langle n | \hat{u}_q | m \rangle|^2 \frac{e^{-\beta E_n} - e^{-\beta E_m}}{E_m - E_n - \hbar\omega - i\hbar\eta} \quad (4.25)$$

$$\hat{\mathcal{D}}(\omega_p) = \sum_{n,m} \frac{1}{Z} |\langle n | \hat{u}_q | m \rangle|^2 \frac{e^{-\beta E_n} - e^{-\beta E_m}}{E_m - E_n - i\hbar\omega_p}, \quad (4.26)$$

where Z is the partition function calculated in the basis set $\{|n\rangle\}$. Thus, we see that, with our choices of normalization and sign conventions, the analytic continuation between the real-time and imaginary-time description holds with

$$\hat{D}_q(\omega) = \hat{D}_q(-i\omega + \eta). \quad (4.27)$$

4.3.2 Feynman rules

Parameter-free numerical work, which has as its goal the calculation of quantities which can be compared directly to experiment demands that all prefactors be accounted carefully. We thus review here briefly the standard many-body treatment with particular focus on all normalizations.

For the present problem of interacting phonons, we can divide the many-body Hamiltonian of the phonon system into an unperturbed part, H_0 , that describes a non-interacting collection of oscillators and a second part, H_1 , that describes phonon-phonon interaction. Partitioning the Hamiltonian in this way allows us to use many-body perturbation theory to evaluate $\mathcal{D}_q(\tau)$ as

$$\mathcal{D}_q(\tau) = \frac{\langle T [u_q(\tau)u_{-q}(0)S(\beta)] \rangle_{\beta H_0}}{\langle S(\beta) \rangle_{\beta H_0}}, \quad (4.28)$$

where $\langle \dots \rangle_{\beta H_0}$ represents the thermal average computed within the Boltzmann distribution of the noninteracting Hamiltonian H_0 , and $S(\beta)$ is the imaginary time evolution operator, given by

$$S(\beta) = \sum_n \frac{(-1)^n}{n!} \int_0^\beta d\tau_1 \dots \int_0^\beta d\tau_n H_1(\tau_1) \dots H_1(\tau_n). \quad (4.29)$$

From Equation (4.14), we see that, for a system of interacting phonons, $H_1(\tau_n)$ for any order is essentially a product of $u_q(\tau_n)$ operators, in which case we have a particularly simple form for the expressions inside the expectation values. We

need, then, to compute the ground state expectation of a time-ordered sequence of annihilation and creation operators. This task, although straightforward, becomes cumbersome as the order of the terms in the sum in Equation (4.29) increases.

The diagrammatic approach first proposed by Feynman exploits the fact that by Wick's theorem, a time-ordered bracket such as in Equation (4.28) can be evaluated by forming all permutations of paired, time-ordered products. Then to simplify the task of keeping track of these products the method assigns to each of them a diagram. In these diagrams, each of the products, which is a free Green's function in the expansion is represented by a line, and each *vertex*, which is defined by an interaction term, is represented by a dot, connected by the Green's function lines. Such a diagram is discussed below and some examples appear in Figure 4.2. Applying Wick's theorem is, then, just a matter of constructing *distinct* diagrams (This takes care of the factor of $\frac{1}{n!}$ from Equation (4.29) in the usual way.) and adding them up.

Similar to the numerator, we can also use Wick's theorem and Feynman diagrams to expand the denominator of Equation (4.28). After performing the assignment of diagrams to the terms in the expansion of $\langle S(\beta) \rangle_{\beta H_0}$, the resulting expansion cancels, in the usual way, the so-called *unlinked* diagrams in the expansion of the numerator. As a result of this simplification, the phonon Green's function becomes

$$D_q(\tau) = \sum \langle T [u_q(\tau)u_{-q}(0)S(\beta)] \rangle_{\beta H_0}^{\text{linked}}, \quad (4.30)$$

where the only Feynman diagrams we need consider in calculating the expectation value are the linked ones.

Any given order, σ , of interaction may be represented in terms of Feynman diagrams. We are now prepared to derive a set of rules for use in converting Feynman

diagrams into mathematical expressions with proper normalization. Once these rules are established with the correct normalization factors, we can immediately write down the expressions corresponding to any given diagram.

1. For a process of order σ , each vertex has σ free-propagation lines connected to it. The free-propagation lines are pictorial representations of *bare* phonon Green's functions given in the Matsubara representation by

$$\hat{\mathcal{D}}_q^{(0)}(\omega_p) = \frac{1}{m} \frac{1}{\omega_p^2 + \omega_q^2}. \quad (4.31)$$

2. Each of these free-propagation lines connect two vertices. In a diagram with n vertices, there are $l = \frac{n\sigma}{2} + 1$ free-propagation lines. We can see this through a simple counting argument: If we assume for the time being that the first and last lines are interconnected, there are σ lines connected to each vertex. However, since for each vertex that creates a free-propagation line, there must exist a vertex that annihilates that line, we only have $n\sigma/2$ lines. The final additional line in l then results from the fact that the last line is in fact distinct from the first.

3. From Equation (4.29), each vertex n comes with an integral over the relevant imaginary time variable, τ_n . Let's consider one of these vertices for a process of order σ . As mentioned above, the number of bare Green's function lines that emerge from such a vertex is σ . The time integrals related to such a vertex can be evaluated by

$$\int_0^\beta d\tau_n D_{q_1}(\tau_n - \tau_1) \dots D_{q_\sigma}(\tau_n - \tau_\sigma) = \left(\frac{1}{m\beta}\right)^\sigma e^{i(\omega_{p_1}\tau_1 + \dots + \omega_{p_\sigma}\tau_\sigma)} \sum_{p_1 \dots p_\sigma} \frac{1}{\omega_{p_1}^2 + \omega_{q_1}^2} \dots \frac{1}{\omega_{p_\sigma}^2 + \omega_{q_\sigma}^2} \underbrace{\int_0^\beta d\tau e^{-i(\omega_{p_1} + \dots + \omega_{p_\sigma})\tau}}_{\beta \delta_{\omega_{p_1} + \dots + \omega_{p_\sigma}, 0}}. \quad (4.32)$$

The Kronecker- δ , which results from performing the imaginary time integration, dictates that there is a conservation of discrete frequencies at each vertex. In addition to the Kronecker- δ s, the integration over τ_n for each vertex also contributes a factor of β .

4. For each vertex in the diagram, we have a factor of

$$\frac{-1}{N_{cell}^{\sigma/2-1}} \sum_{q_1 \dots q_\sigma} V_{q_1 \dots q_\sigma}, \quad (4.33)$$

where $V_{q_1 \dots q_\sigma}$ is the *coupling strength* at order σ . The factor of $\frac{1}{N_{cell}^{\sigma/2-1}}$, on the other hand, is an arbitrary constant that simplifies the expressions introduced below. In the first order that we consider below, the factor of $(-1)^\sigma$ in Equation (4.33) can be ignored because there are always an even number of vertices.

5. Equation (4.32) evaluates the time integration of all but the last one of the bare Green's functions, which must be considered separately. This last integration leaves an exponential factor, which results in the following form for the Green's function

$$\mathcal{D}_q(\tau) = \frac{1}{\beta} \sum_{\omega_p} (\text{line})^{n\sigma/2+1} \times (\text{vertex})^n e^{-i\hbar\omega_p\tau}, \quad (4.34)$$

where “line” and “vertex” are simply shorthands for line and vertex contributions. From Equation (4.24), we identify the Fourier transform of $\mathcal{D}(\tau)$ as

$$\hat{\mathcal{D}}_q(\omega_p) = (\text{line})^{n\sigma/2+1} \times (\text{vertex})^n. \quad (4.35)$$

6. Due to the translational symmetry of the crystal, the matrix element $V_{q_1 \dots q_\sigma}$ imposes momentum conservation. As a result, there are only $\sigma - 1$ inde-

Table 4.1: Feynman rules. Representations, numbers and contributions of the different elements constituting a Feynman diagram.

Object	Number	Contribution
Interaction vertex	n	$\frac{\beta}{N_{cell}^{\sigma/2-1}} V_{q_1 \dots q_\sigma}$
Free propagator	$l = \frac{n\sigma}{2} + 1$	$\frac{1}{m\beta} \frac{1}{\omega_p^2 + \omega(q)^2}$
Independent internal momentum (q_i)	$n \left(\frac{\sigma}{2} - 1 \right)$	$\sum_i = N_{cell}^{n(\sigma/2-1)} \int \prod_i \frac{adq_i}{2\pi}$
Internal Matsubara frequency (ω_p)	$n \left(\frac{\sigma}{2} - 1 \right)$	$\sum_{\{\omega_p\}}$

pendent q_i at each vertex, where the remaining one is determined from the independent q_i . The total number of independent q_i is then $n \left(\frac{\sigma}{2} - 1 \right)$.

7. The counting of the independent Matsubara frequencies works in exactly the same way since for each q , there is an ω_n , whose conservation rule is identical.

Before we proceed with the evaluation of the Green's function for a particular interaction, we summarize the rules derived above in Table 4.1. Once these rules are enumerated in the form of a look-up table, we have a recipe for writing an arbitrary diagram by just consulting it.

For a one-dimensional system such as a nanotube, whose length is much larger than its interatomic distance, the sum over the k vectors may be converted to an integral using

$$\sum_q \rightarrow \int \frac{Ldq}{2\pi} \quad (4.36)$$

where $L = aN_{cell}$ is the total length with N_{cell} being the total number of unit cells and a is the length of a single unit cell. Since there are as many such integrals as there are independent q values, the factor of N_{cell} coming from the integral picks up an exponent of $n(\sigma/2 - 1)$ canceling the factors of $1/N_{cell}^{\sigma/2-1}$ included earlier in

the definition of the vertex contribution.

4.3.3 Renormalization, polarization and quality factor

Even though Feynman rules simplify enormously the task of dealing with chains of time-ordered products from Wick's theorem, the resulting diagrams are often rather complicated. However, in most diagrams there exists a repeating term and the Feynman diagram has the form in Figure 4.1. Each shaded circle represents a set of vertices connected by free propagation lines. In converting to mathematical expressions, these shaded circles become the *polarization* terms and are themselves connected by free lines. The mathematical representation corresponding to the diagram in Figure 4.1 is

$$\begin{aligned}\hat{\mathcal{D}}_q(\omega_n) &= \hat{\mathcal{D}}_q^{(0)}(\omega_n) + \hat{\mathcal{D}}_q^{(0)}(\omega_n)P_q(\omega_n)\hat{\mathcal{D}}_q^{(0)}(\omega_n) + \dots \\ &= \hat{\mathcal{D}}^{(0)} + \hat{\mathcal{D}}^{(0)}P\hat{\mathcal{D}}^{(0)} + \hat{\mathcal{D}}^{(0)}P\hat{\mathcal{D}}^{(0)} + \hat{\mathcal{D}}^{(0)}P\hat{\mathcal{D}}^{(0)}P\hat{\mathcal{D}}^{(0)} + \dots,\end{aligned}\quad (4.37)$$

where $P_q(\omega_n)$ is the polarization. Due to its repetitive nature, the sum of this series of diagrams assumes a particularly simple form,

$$\hat{\mathcal{D}}_q(\omega_n) = \hat{\mathcal{D}}_q^{(0)}(\omega_n) + \hat{\mathcal{D}}_q^{(0)}(\omega_n)P_q(\omega_n)\hat{\mathcal{D}}_q(\omega_n).\quad (4.38)$$

From Equation (4.38) it is straightforward to obtain $\hat{\mathcal{D}}_q(\omega_n)$:

$$\hat{\mathcal{D}}_q(\omega_n) = \frac{1}{(\hat{\mathcal{D}}_q^{(0)}(\omega_n))^{-1} - P_q(\omega_n)}.\quad (4.39)$$

which is referred to as the *renormalized Green's function* of the phonon system. The presence of $P_q(\omega_n)$ in the denominator results in two important changes in the energy spectrum of the phonon system. The first change is a shift in the frequencies of the phonon modes and is given by $\text{Re}P_q(\omega_n)$. The second is the introduction of a finite width to the otherwise infinitely sharp resonances, which decreases the

sensitivity of the oscillator as discussed in Chapter 1 and is also an indicator of energy loss in the system.

The quality factor, which is the measure of energy loss in the system is given by

$$Q^{-1} = \frac{1}{2\pi} \frac{\Delta E}{E}, \quad (4.40)$$

where as noted previously in Equation (2.15), ΔE is the energy lost per unit cycle of the oscillator and E is the total energy in the absence of mechanical loss. For a periodic force $f(t) = \text{Re}f_0 e^{-i\omega t}$ on the amplitude in a phonon mode $u(t) = \text{Re}u_0 e^{-i\omega t}$, ΔE can be written as

$$\Delta E = \oint f(t) \cdot \dot{u}(t) dt = \frac{1}{2} \oint \text{Re}(-i\omega f_0^* u_0) dt = \pi \text{Im}(f_0^* u_0). \quad (4.41)$$

From Equation (4.21), $u_0 = Df_0$, which upon substitution into Equation (4.41) gives

$$\Delta E = \pi \text{Im}(f_0^* Df_0) = \pi |f_0|^2 \text{Im} \frac{|D|^2}{D^*} = \pi |f_0|^2 |D|^2 \text{Im}(D^{-1})^* = \pi |f_0|^2 |D|^2 \text{Im}P, \quad (4.42)$$

where we obtain the second equality in Equation (4.42) with the help of the analytically continued version of Equation (4.39) and the fact that $D^{(0)}$ has only an infinitesimal imaginary part $i\hbar\eta$. Finally, substituting the total energy $E = \frac{1}{2}m\omega^2|u_0|^2$ into Equation (4.40), we obtain the inverse quality factor in terms of the polarization P as

$$Q^{-1} = \frac{1}{m\omega^2} \text{Im}P(\omega), \quad (4.43)$$

where $P(\omega)$ is the polarization corresponding to the real-time Green's function.

$$\mathcal{D}_q(\omega_n) = \text{---} \underset{q, \omega_n}{\text{---}} + \text{---} \underset{q, \omega_n}{\text{---}} \underset{q, \omega_n}{\text{---}} + \text{---} \underset{q, \omega_n}{\text{---}} \underset{q, \omega_n}{\text{---}} \underset{q, \omega_n}{\text{---}} + \dots$$

Figure 4.1: Feynman diagram for a general interaction. The shaded bubbles denote a repeating subset of diagrams.

4.3.4 Experimental conditions, impact of symmetry

In experiments involving suspended nanotubes [1], the nanotube emerges from the series of fabrication steps leading to the suspension with a certain amount of slack, defined in Chapter 5 as the fractional excess length in the tube. Since the slack is usually small compared to the total length of the nanotube ($\approx 2\%$), one would intuitively predict that the mechanical loss due to phonon-phonon interactions would be the same for a slack tube as they are for a straight tube. However, the presence of slack breaks the symmetry of the straight nanotube, allowing certain processes forbidden by the selection rules.

The lowest order nonlinear processes that satisfy energy and momentum conservation are three-phonon processes. We find, however, that for a straight nanotube these third order processes are forbidden by symmetry. Because long wavelength transverse modes of vibration are those of interest in the experiments, the third order coupling is the derivative of the total energy with respect to two phonon modes and the curvature,

$$\frac{\partial M_{ij}}{\partial \rho} = \frac{\partial^3 U}{\partial \rho \partial \eta_i \partial \eta_j}, \quad (4.44)$$

where we have written the derivative with respect to the long-wavelength phonon modes as a derivative with respect to the curvature of a nanotube. (A more rigorous justification will be given later in Section 4.3.5.)

Achiral nanotubes have planes of mirror symmetry that contain the axis of

the nanotube. While chiral nanotubes lack mirror planes, they do have symmetry operations which combine a two-fold rotation around the tube axis with an axial translation. For simplicity, we will consider the case of an achiral nanotube. The argument for the chiral nanotube is analogous.

The third derivative in Equation (4.44) can be written as

$$\frac{\partial^3 U}{\partial \rho \partial u_i \partial u_j} = \frac{1}{ab\rho}$$

$$\lim_{a \rightarrow 0} \lim_{b \rightarrow 0} \lim_{\rho \rightarrow 0} (U_{+\rho}(a\eta_i + b\eta_j) - U_{-\rho}(a\eta_i + b\eta_j) + U_{+\rho}(-a\eta_i - b\eta_j) - U_{-\rho}(-a\eta_i - b\eta_j) \\ - U_{+\rho}(a\eta_i - b\eta_j) - U_{-\rho}(a\eta_i - b\eta_j) - U_{+\rho}(-a\eta_i + b\eta_j) - U_{-\rho}(-a\eta_i + b\eta_j))$$
(4.45)

where the $+\rho$ and $-\rho$ subscripts indicate positive or negative radius of curvature respectively and a and b are infinitesimal amounts by which the atoms are displaced in the directions of the modes η_i and η_j . When we apply the mirror inversion, the curvature changes from $+\rho$ to $-\rho$. For an eigenmode that has odd symmetry under inversion, $\eta \rightarrow -\eta$ and for a mode with an even symmetry $\eta \rightarrow \eta$.

Let's take as an example the case where both phonons are even. In this case, applying the mirror inversion to all the terms on the right hand side of Equation (4.45) simply changes all the $+$ subscripts to $-$ subscripts, with the net result that the third derivative is equal to its negative, and thus must be zero. The same result holds true for all even/odd combinations. Thus there is no third order coupling between the radius of curvature and two phonons in achiral nanotubes. This result applies to the radius curvature in any direction, since achiral nanotubes have several axial mirror planes among their symmetry operations.

As a result, in a straight nanotube, the lowest order allowed processes are four-phonon processes. In a slack tube on the other hand, since the inversion symmetry

is broken, the discussion of the preceding two paragraphs no longer holds and three-phonon processes are also permitted. In Section 4.3.5 and Section 4.3.6, we study three-phonon processes in the presence of a slack and four phonon processes in a straight tube in order to assess their relative importance, which is not known *a priori*.

4.3.5 Three-phonon processes

Three-phonon processes in a nanotube with slack are described by the third order term in the energy expansion, which is formally identical to the corresponding term for a straight nanotube. The perturbing interaction Hamiltonian is, thus, given as,

$$H_1 = \frac{1}{3!} \frac{\partial^3 \mathcal{U}}{\partial u_{q_i} \partial u_{q_j} \partial u_{q_k}} \Big|_{u_{q_i} u_{q_j} u_{q_k}} \quad (4.46)$$

where the third derivative is evaluated in a bent nanotube. The interaction Hamiltonian in Equation (4.64) is written in terms of amplitudes in normal modes as was done previously in Equation (4.16). The full Green's function for this interaction corresponds to Feynman diagrams composed of three-phonon vertices connected to each other by free phonon Green's functions as shown in Figure 4.2. We consider only the lowest order Feynman diagrams corresponding to a polarization diagram with only two vertices and two lines, shown in Figure 4.3, which according to the rules in Table 4.1 becomes

$$P_q(\omega_q) = \frac{1}{\beta m^2} \int_{-\infty}^{\infty} \frac{a dq_1}{2\pi} \sum_n \frac{1}{\omega_n^2 + \omega_1^2} \frac{1}{(\omega_q - \omega_n)^2 + \omega_2^2} \left(\frac{\partial^3 \mathcal{U}}{\partial u_q \partial u_{q_1} \partial u_{q_2}} \right)^2, \quad (4.47)$$

where q_1 is the intermediate momentum, a is the unit cell length and arises from the conversation of the sum over q values into an integral as discussed in Section 4.3.5.

We perform the summation over the discrete frequencies using the Matsubara



Figure 4.2: Feynman diagrams corresponding to three-phonon processes

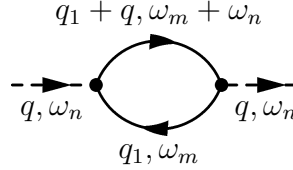


Figure 4.3: Polarization diagram for the three-phonon Dyson sum.

summation formula [10]:

$$\sum_m F(\omega_m) = (-i\beta\hbar) \sum_\alpha \frac{1}{e^{\beta\hbar\omega_\alpha} - 1} \text{Res}(\omega_\alpha), \quad (4.48)$$

where $F(\omega_n)$ is an arbitrary function of ω_n with poles at $\{\omega_\alpha\}$ and $\text{Res}(\omega_\alpha)$ are the residues of $F(\omega_n)$ at its poles.

For the three-phonon case, we have a product of two simple functions, each of which gives two poles, resulting in four terms. Of these terms only the one conserving frequency satisfies the δ -function below to give a non-zero contribution to $\text{Im}P$. Writing this term only, we find

$$\sum_m \frac{1}{\omega_m^2 + \omega_1^2} \frac{1}{(\omega_n + \omega_m)^2 + \omega_2^2} = \frac{\beta\hbar}{4} \frac{1}{-i\omega_q + (\omega_1 - \omega_2)} (N_1 - N_2) + \dots, \quad (4.49)$$

where N_i refer to Bose-Einstein distribution functions, $(e^{\beta\hbar\omega_i} - 1)$ for the relevant frequency, ω_i . For ease of notation, we employ the definitions $\omega_1 \equiv \omega(q_1)$ and $\omega_2 \equiv \omega(q + q_1)$.

Making the analytic continuation 4.27 and taking the limit $\eta \rightarrow 0$, the frequency denominator in Equation (4.49) becomes

$$\frac{1}{-i\omega_q + (\omega_1 - \omega_2)} \frac{-1}{\omega - (\omega_1 - \omega_2) + i\eta} = P \frac{-1}{\omega - (\omega_1 - \omega_2)} + i\pi\delta(\omega - (\omega_1 - \omega_2)), \quad (4.50)$$

where P stands for the principal part. Substituting the δ -function in Equation (4.50) into $\text{Im}P$ in Equation (4.47), and evaluating the resulting simple integral, we arrive at the final equation for Q^{-1}

$$Q^{-1} = \frac{1}{8} \frac{1}{\omega^2} \frac{\hbar}{m^3} \int \frac{adq_1}{2\pi} \delta(\omega_2 - \omega_1 - \omega) \frac{N_1 - N_2}{\omega_1 \omega_2} \left(\frac{\partial^3 U}{\partial u_q \partial u_{q_1} \partial u_{q_2}} \right)^2, \quad (4.51)$$

where by momentum conservation, $q_2 = q_1 + q$.

Because of the Dirac- δ in Equation (4.51), the integral can be readily evaluated and reduced to a sum over wavevectors for which the argument of the δ -function is equal to zero (energy conservation). Assuming $\omega \approx 0$, this condition is satisfied only at branch crossings in the dispersion relation. In Figure 4.4, the dispersion for (12,0) and (18,0) nanotubes are shown. At low temperatures, the crossing marked with a dot becomes one of the most dominant crossings due to its low frequency.

After the δ -function imposes energy conservation, Equation (4.51) becomes

$$Q^{-1} = \frac{1}{8} \frac{1}{\omega^2} \frac{a\hbar}{m^3} \sum_x \frac{1}{|v_1 - v_2|} \frac{1}{\omega_1 \omega_2} (N_1 - N_2) \left(\frac{\partial^3 U}{\partial u_q \partial u_{q_1} \partial u_{q_2}} \right)^2, \quad (4.52)$$

where the sum \sum_x indicates a sum over crossings in the nanotube dispersion and $v_1 - v_2$ is the group velocity difference between the branches involved at the crossing point and is related to the density of states that arises while evaluating the q_1 integral. The third derivative in Equation (4.52) should of course be evaluated at the crossings.

When calculating the third derivative with respect to normal mode amplitudes in the bent configuration, we utilize the fact that both the slack profile and the perturbing mode can be considered as long wavelength phonon modes. Assuming that the slack is small, we expand the third derivative around the straight nanotube, which then becomes a fourth derivative,

$$\frac{\partial^3 U(\{x_i + s_i\})}{\partial u_q \partial u_{q_1} \partial u_{q_2}} = \sum_i \frac{\partial^4 U(\{x_i\})}{\partial u_q \partial u_{q_1} \partial u_{q_2} \partial x_i} s_i, \quad (4.53)$$

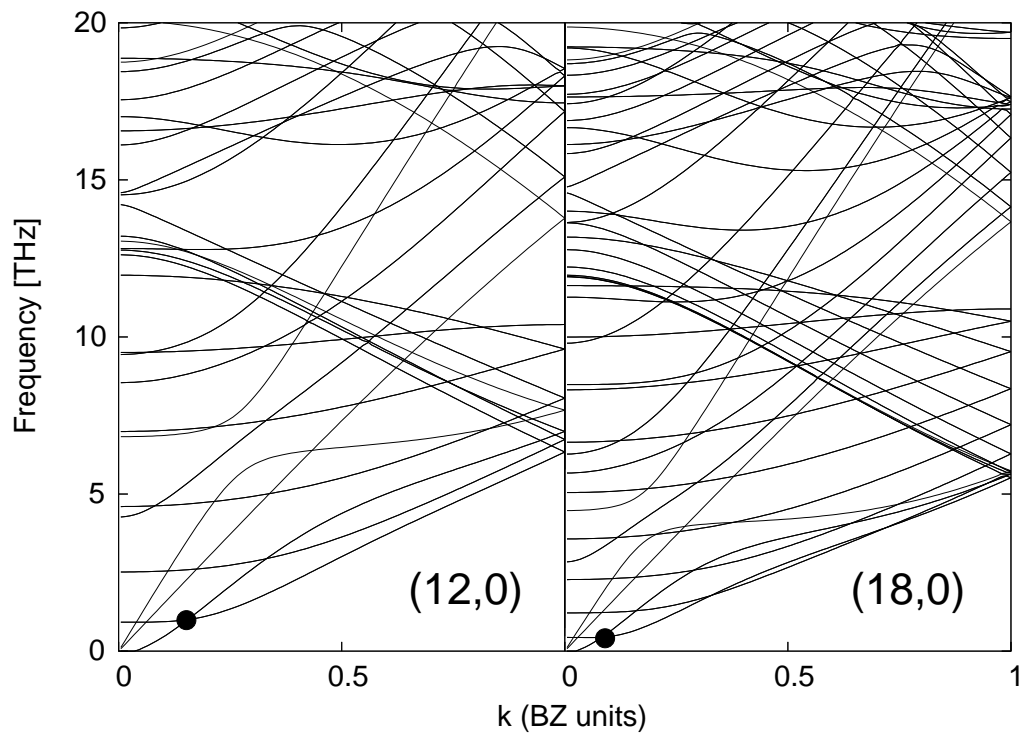


Figure 4.4: Dispersion relation for (12,0) and (18,0) nanotubes

where s_i is the displacement of the i th coordinate in the slack configuration. For ease of notation, we make the following definition,

$$\frac{\partial^2 U}{\partial u_{q_1} \partial u_{q_2}} = M_{q_1 q_2}. \quad (4.54)$$

To exploit the long wavelength character of the slack profile, we decompose it into its Fourier components,

$$s_i = \sum_{q'} \hat{s}(q') e^{iq'R_i} \hat{e}_i, \quad (4.55)$$

where $\hat{s}(q')$ is the Fourier component and \hat{e}_i is the i th component of the $3N$ dimensional unit vector representing unit motion of each atom along a coordinate of the direction perpendicular to the tube and express the space dependence of mode q explicitly. Equation (4.53) then becomes

$$\sum_i \frac{\partial^2 M_{q_1 q_2}}{\partial u_q \partial x_i} s_i = \frac{1}{\sqrt{N_{cell}}} \sum_{ij} \sum_{q'} \frac{\partial^2 M_{q_1 q_2}}{\partial x_j \partial x_i} \tilde{\eta}_{qj} e^{iqR_j} \hat{s}(q') e^{iq'R_i} \hat{e}_i, \quad (4.56)$$

where $\tilde{\eta}_{qj}$ is the displacement of the j th coordinate of mode q normalized to the unit cell and R_i and R_j run over the unit cells in the nanotube. In a long-wavelength phonon mode, atoms in the same unit cell approximately have the same displacement. Applying this approximation to the driven mode q , Equation (4.56), becomes

$$\frac{\partial^2 M_{q_1 q_2}}{\partial u_q \partial x_i} s_i = \frac{1}{\sqrt{N_{cell} N_{at}}} \sum_{ij} \sum_{q'} \frac{\partial^2 M_{q_1 q_2}}{\partial x_i \partial x_j} e^{iqR_j} \hat{e}_j e^{iq'R_i} \hat{e}_i, \quad (4.57)$$

where N_{at} is the number of atoms in a unit cell and is a result of the normalization convention we have chosen for $\eta_{q'}$. For small q and q' , we may expand the exponentials in Equation (4.57) as a polynomial series. The zeroth and first order terms give zero when the sum is performed since they correspond to a uniform translation and tilting of the whole nanotube and therefore do not cause any change in energy.

This then leaves $e^{iqR_i} \rightarrow -\frac{1}{2}q^2R_i^2$. We note that the same affect can be generated by imposing a uniform curvature of radius $r = \frac{1}{\rho}$ because then

$$x_i = \hat{e}_i \sqrt{(1/\rho)^2 - R_i^2} \approx \hat{e}_i \left(\frac{1}{\rho} - \frac{\rho R_i^2}{2} \right), \quad (4.58)$$

so that if we take $\rho = q^2$, the curvature corresponds precisely to the factor $e^{iqR}\hat{e}_i$

Differentiating x_i with respect to ρ , we have

$$\frac{\partial x_i}{\partial \rho} = - \left(\frac{1}{\rho^2} - \frac{q^2 R_i^2}{2} \right) \hat{e}_i. \quad (4.59)$$

Thus,

$$\sum_i \frac{\partial^2 M_{q_1 q_2}}{\partial u_q \partial x_i} s_i = \frac{1}{\sqrt{N_{cell} N_{at}}} \frac{\partial^2 M_{q_1 q_2}}{\partial \rho^2} q^2 \sum_{q'} q'^2 \hat{s}(q'), \quad (4.60)$$

When squaring Equation (4.60) in Equation (4.51), we must take special care since what is being squared is not the operator itself but its expectation value between states dictated by momentum and energy conservation rules. The summation is applied after the expectation value is calculated. The factor $1/N_{cell}$ that we obtain when we square Equation (4.60) combines with the N_{cell} that results from converting the sum $\sum_{q'}$ into an integral performed below and yields a size-independent result. The final expression for Q^{-1} is then

$$Q^{-1} = \frac{1}{8N_{at}} \frac{1}{\omega^2} \frac{aq^4 \hbar}{m^3} \sum_{\times} \frac{1}{|v_1 - v_2|} \frac{1}{\omega_1 \omega_2} (N_1 - N_2) \left(\frac{\partial^2 M_{\times}}{\partial \rho^2} \right)^2 \langle C^2(x) \rangle, \quad (4.61)$$

where M_{\times} is a short-hand notation for $M_{q_1 q_2}$ defined in Equation (4.54) evaluated at the crossings and $\langle C^2(x) \rangle$ is the average square curvature of the slack profile of the nanotube, given by

$$\langle C^2(x) \rangle = \int \frac{du}{L} \left| \frac{\partial^2 s(u)}{\partial u^2} \right|^2, \quad (4.62)$$

where u is the coordinate that runs along the tube. Approximating a slack profile for a slack of $s = \frac{L-W}{L}$ as defined in Chapter 5, by the simplest model shape

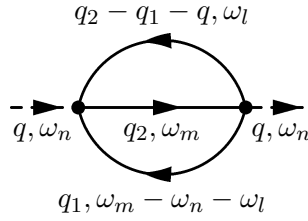


Figure 4.5: Polarization diagram for the four-phonon Dyson sum.

consistent with the boundary conditions of straight clamping,

$$s(u) = A \cos(2\pi u/L), \quad (4.63)$$

we obtain the estimate $\langle C^2(x) \rangle = 2 \left(\frac{2\pi}{L}\right)^2 s$.

4.3.6 Four-phonon processes

The lowest order processes allowed in a straight nanotube are those that involve four phonons. The perturbing Hamiltonian for such processes is given by

$$H_1 = \frac{1}{4!} \frac{\partial^4 \mathcal{U}}{\partial u_{q_1} \partial u_{q_2} \partial u_{q_3} \partial u_{q_4}} \Big|_{\text{straight}} u_{q_1} u_{q_2} u_{q_3} u_{q_4}, \quad (4.64)$$

where once again the Hamiltonian is written in terms of the amplitudes in the normal modes.

The calculation of Q^{-1} proceeds in a similar way to the three-phonon case of Section 4.3.5. In the four-phonon case, four free phonon lines intersect at each vertex resulting in a $P(\omega_q)$ that can be represented by the diagram shown in Figure 4.5, with the corresponding conservation rules..

The additional line in Figure 4.5 brings another free phonon propagator as well as another integration over an intermediate q . Because there are still two vertices, the vertex contributions do not change except, of course, the matrix element, which we discuss below. Using Table 4.1, we collect the appropriate contributions of the lines and vertices and perform the Matsubara sums to arrive at the following

expression for Q^{-1}

$$Q^{-1} = \frac{\pi}{2} \left(\frac{\hbar}{m^2\omega} \right)^2 \iint \frac{a dq_1}{2\pi} \frac{a dq_2}{2\pi} \delta(\omega_2 - \omega_1 - \omega_3 - \omega) \times \frac{N_1 N_3 - N_2(N_1 + N_3 + 1)}{\omega_1 \omega_2 \omega_3} \left| \frac{\partial^4 \mathcal{U}}{\partial u_{q_1} \partial u_{q_2} \partial u_{q_3} u_q} \right|^2 \quad (4.65)$$

where here again, by momentum conservation $q_3 = q_2 - q_1 - q$. In Equation (4.65), q_3 has been designated to be the long-wavelength mode whereas q_1 and q_2 are the remaining two modes. Here we once again use the definitions $\omega_1 \equiv \omega(q_1)$, $\omega_2 \equiv \omega(q_2)$ and $\omega_3 \equiv \omega(q_2 - q_1 - q)$

For the calculation of the fourth derivative of energy in Equation (4.65), we follow a procedure that is very similar to yet slightly simpler than the three-phonon case. In the four-phonon case, both of the long-wavelength disturbances are phonon modes, which can then be treated on equal footing. Proceeding in the same way with identical assumptions and taking q_3 to be the long-wavelength phonon mode, we arrive at

$$\left| \frac{\partial^4 \mathcal{U}}{\partial u_{q_1} \partial u_{q_2} \partial u_{q_3} u_q} \right|^2 = \frac{1}{N_{cell}^2 N_{at}^2} \left(\frac{\partial^2 M_{q_1 q_2}}{\partial \rho^2} \right)^2 q^4 q_3^4. \quad (4.66)$$

The greatest contribution to Q^{-1} comes from terms where one of the three intermediate states is a long wavelength transverse acoustic mode, because both the inverse frequency and the Bose factor favor low frequency modes. Therefore, we compute only these contributions, which are also somewhat simpler to compute. Note that this restriction still allows us to place an *upper* bound on the quality factor.

In evaluating Equation (4.65), we restrict q_1 and q_2 to pairs of branches in the dispersion relation that have crossing since for ω_3 with a large wavelength, they give the largest contribution. To make the calculations possible, we make the further assumption that for a given pair q_1 and q_2 , the fourth derivative is the

same at each wavevector as it is at a crossing. This is justified by the Bloch-like nature of the normal modes, which dictates that the *distortion character* of the modes remain the same throughout the Brillouin zone, differing principally only by a phase that drops out of the matrix element when squared.

We perform one of the integrals in Equation (4.65) by means of a geometric construction to find sets of (q_1, ω_1) , (q_2, ω_2) and (q_3, ω_3) that satisfy the argument of the δ -function [11]. This geometric construction involves the translation of the origin of the ω_3 branch onto the point (q_2, ω_2) and finding q_1 such that the translated ω_3 intersects ω_1 . The evaluation of the δ -function brings a density of states contribution of $|v_1 - v_2|$, where v_1 and v_2 are the group velocities of the branches at the crossing points. After performing the first integral, we are left with a second integral,

$$Q^{-1} = \frac{\pi}{2} \left(\frac{\hbar a q^2}{2\pi N_{at} \omega m^2} \right)^2 \sum_{\times} \left| \frac{\partial^2 M_{\times}}{\partial \rho^2} \right|^2 \times \int dq_1 \frac{q_3^4}{|v_1 - v_2|} \frac{N_2 N_3 - N_1 (N_2 + N_3 + 1)}{\omega_1 \omega_2 \omega_3}, \quad (4.67)$$

which we evaluate numerically using a simple trapezoid rule. Here, as in Equation (4.61), the sum \sum_x denotes a sum over branch crossings and M_{\times} is $M_{q_1 q_2}$ evaluated at the crossings.

In keeping with the assumption that ω_3 has a long wavelength we impose an upper cutoff on q_3 and discard those (q_3, ω_3) that are above this cutoff. We test our results for a variety of such cutoffs and conclude that for the range of cutoffs ranging between $\frac{0.3\pi}{a}$ to the Brillouin zone edge, the Q^{-1} changes by a factor of only approximately 3. Since our interest here is to determine an order of magnitude estimate for a lower bound on loss, we use the lowest value in this range. The results that we present in Section 4.5 is then for a limit of $k_{upper} = 0.3\frac{\pi}{a}$.

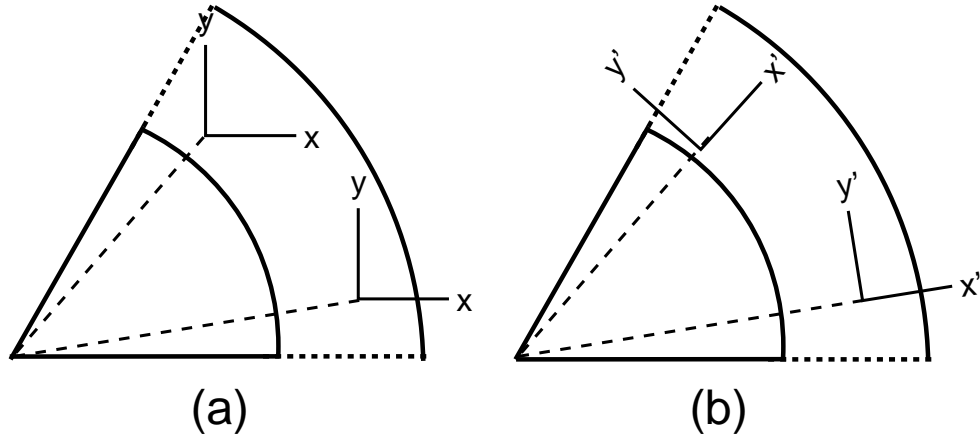


Figure 4.6: Coordinate transform in nanotori. (a) Before transform. Bloch's theorem does not apply due to lack of symmetry. (b) After transform. Each point on the nanotube has a set of coordinate axes that are aligned with the radius. Bloch's theorem can be used.

4.4 Methods

4.4.1 Calculation of γ_q and $\frac{\partial^2 M_x}{\partial \rho^2}$

Calculation of γ_q in Equation (4.2) and $\frac{\partial^2 M_x}{\partial \rho^2}$ in Equation (4.67) and Equation (4.61) both involve the evaluation of the second derivative with respect to the curvature ρ of the matrix elements of the dynamical matrix $M_{q_1 q_2}(\rho)$ between two phonon branches, α and β . Once the dependence of $M_{q_1 q_2}(\rho)$ on ρ is known, $\frac{\partial^2 M_x}{\partial \rho^2}$ can easily be calculated by evaluating the second derivative at the crossing labeled by \times . Calculation of γ_q on the other hand is a slightly more indirect procedure since γ_q is not related to the second curvature derivative of the matrix element, M_x , but rather to the second curvature derivative of the frequency ω_q . Using an approach analogous to the Hellman-Feynman theorem for derivatives of expectation values

in electronic systems, we find that the Grüneisen constant is related to $M_{q_1q_2}(\rho)$ by

$$\gamma_q = \frac{\partial^2 \omega_q}{\partial \rho^2} = \frac{1}{2m\omega_q} \frac{\partial^2}{\partial \rho^2} \langle \eta_q(0) | M_{q_1q_2}(\rho) | \eta_q(0) \rangle = \frac{1}{2m\omega_q} \frac{\partial^2}{\partial \rho^2} M_q(\rho) \Big|_{\rho=0} \quad (4.68)$$

where $\eta_q(0)$ is a mode in the straight nanotube, for which $\rho = 0$. The second derivative in Equation (4.68) can easily be evaluated once $M_q(\rho)$ is known for several values of ρ .

We carry out the computational determination of $\frac{\partial^2 M_\times}{\partial \rho^2}$ in Equation (4.61) and Equation (4.67) and $\frac{\partial^2 M_q(\rho)}{\partial \rho^2}$ in Equation (4.68) using a *nanotorus* which is a nanotube that closes on itself in a circle (see Figure 4.7). A nanotorus with radius R has a uniform curvature of $\rho = 1/R^2$. We compute energies and forces using the second generation bond-order potential developed by Brenner and coworkers [12]. After forming the nanotori from straight nanotubes, we relax them using a conjugate gradients algorithm.

Once $M_q(\rho)$ and $M_\times(\rho)$ are calculated for different radii, it is straightforward to evaluate the dependence on ρ . In Figure 4.8, we present an example from a crossing in a (12,0) nanotube. In Figure 4.8(a), we see that $M_\times(\rho)$ has quadratic dependence on ρ and extrapolates to zero for large radius. In Figure 4.8(b), we show a close-up of Figure 4.8(a).

4.4.2 Bloch's theorem and calculations in nanotori

At first glance, a nanotorus seems inconvenient as a computational system. The nanotori appropriate for calculating $M_\times(\rho)$ and $M_q(\rho)$ should be large enough to prevent cross-sectional collapse due to compression and approximate a large wavelength phonon mode. For a (12,0) nanotube, for example, the number of

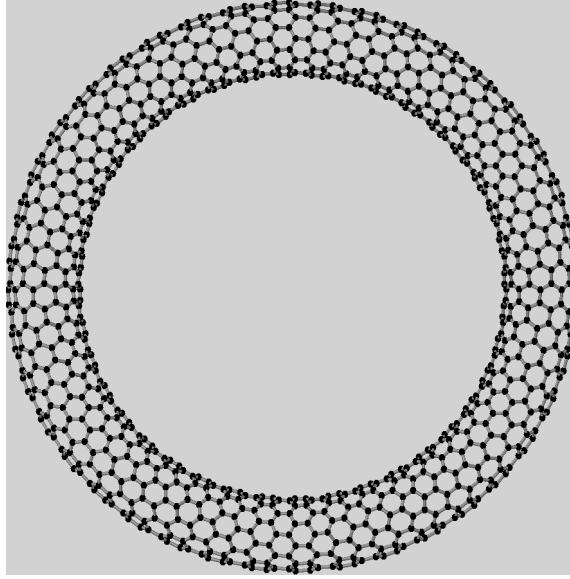


Figure 4.7: Nanotorus. We use nanotori in our calculations of γ_q and $\frac{\partial^2 M_x}{\rho^2}$ because it provides an approximation to a nanotube with a large wavelength disturbance.

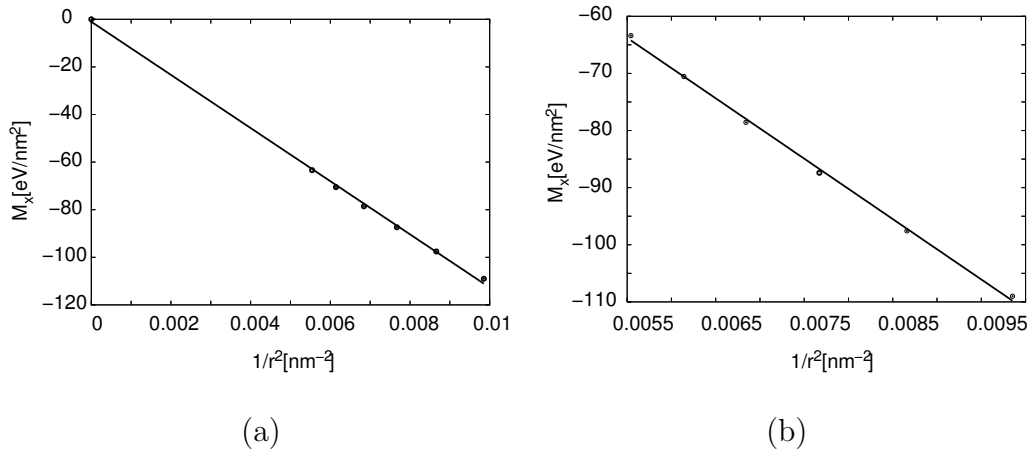


Figure 4.8: Dependence of M_x on ρ . (a) extrapolated to zero (b) close-up

atoms necessary for a minimally large nanotube is approximately 10^5 . The size of the calculations thus becomes prohibitively large even for moderate-sized nanotori.

Unfortunately, the lack of translational symmetry in a nanotorus reflects itself in the dynamical matrix. The nanotorus cannot be broken down into smaller pieces whose dynamical matrices are identical and therefore cannot be used in the application of Bloch's theorem. We can, however, make use of the rotational symmetry of the nanotorus if we can define a new coordinate system that makes the dynamical matrix rotationally symmetric. Such a coordinate system is one in which the axis is always tangent to the rim of the nanotorus as shown in Figure 4.6. With this transform, each point on the nanotorus has a local coordinate system which is aligned with the radius. Since these new coordinate axes reflect the rotational symmetry with respect to their orientation, the dynamical matrices in each unit cell now become identical and Bloch's theorem can be applied.

Our procedure for calculating $\frac{\partial^2 M_\times}{\partial \rho^2}$ and $\frac{\partial^2 M_q}{\partial \rho^2}$ using nanotori involves constructing nanotori of varying radii by rolling straight nanotubes of appropriate length in a circle. We then relax the atomic coordinates using a conjugate-gradients algorithm and calculate M_\times and M_q for all the nanotori using a representative unit cell and making use of Bloch's theorem. Note that except for the initial relaxation of the nanotori, our calculations take place entirely in a unit cell and therefore require only very small computational effort. To make full use of the rotational symmetry during the relaxation phase is in progress at the time of this writing.

4.5 Results

Figure 4.9 displays Q^{-1} and Q versus temperature for a (12,0) nanotube(a) and a (18,0) nanotube(b) in the Landau-Rümer limit for three-phonon interactions. In

both cases, the frequency ω of the excited vibration mode has been calculated from the basic formula for the lowest vibration frequency of a beam

$$\omega = \frac{22.4}{L^2} \sqrt{\frac{Yr^2}{\lambda}} \quad (4.69)$$

where L is the length of the nanotube, Y is the extensional modulus, r is the radius and λ is the linear mass density. The slack in both the (12,0) nanotube and the (18,0) nanotube are taken to be 2%.

Figure 4.9 shows Q^{-1} and Q versus temperature for a (12,0) nanotube(a) and a (18,0) nanotube(b).

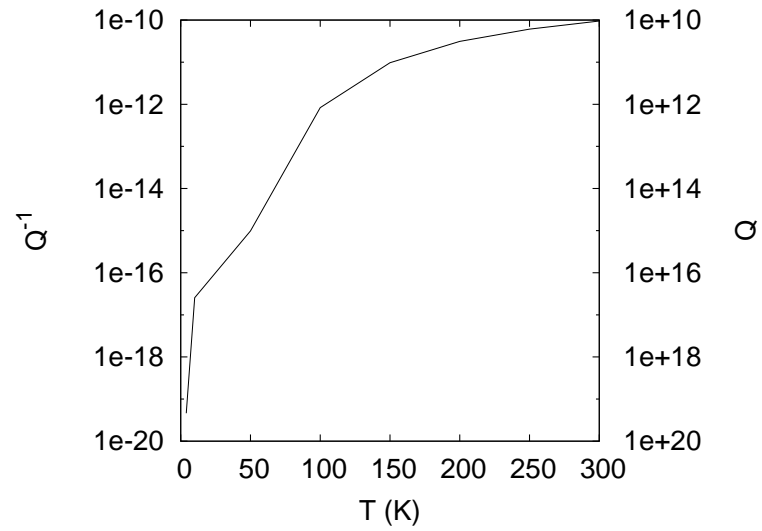
4.6 Conclusion

In this chapter, we studied the contribution of phonon-phonon processes to mechanical loss in the Landau-Rümer limit, which treats the thermal phonons as being ballistically scattered by the acoustic phonon. We considered three-phonon interactions in a nanotube with slack and a four-phonon interaction in a straight nanotube.

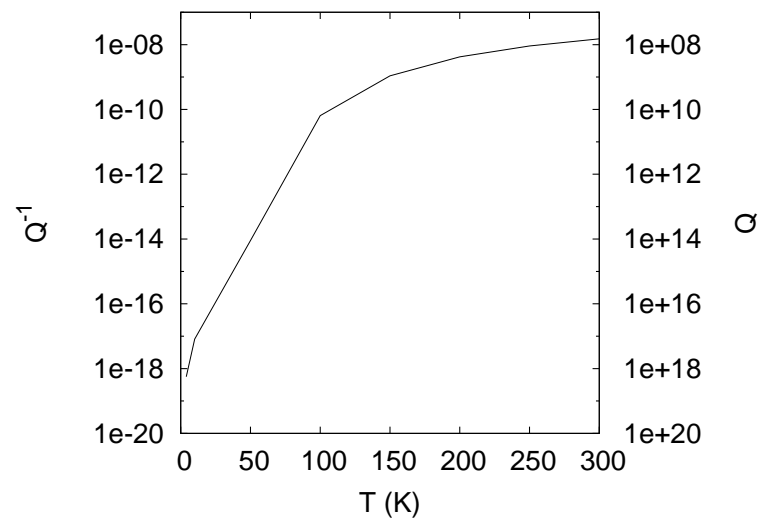
From the results presented in Section 3.5, we conclude that for the three-phonon case at room temperature, the quality factor varies by a about 2 orders of magnitude going from a (12,0) nanotube to an (18,0) nanotube, whereas for the four-phonon case, the quality factor is very similar.

For typical slacks of around 2%, we find that the four-phonon processes are dominant, which indicates that for these slacks, we can consider the tube as being straight.

Our calculations place an upper limit of around 10^8 on the quality factor for intrinsic mechanical loss due to phonon-phonon interactions for tube diameters in



(a)



(b)

Figure 4.9: Q^{-1} and Q versus temperature for three-phonon processes in the Landau-Rümer limit for (a) a (12,0) nanotube and (b) an (18,0) nanotube.

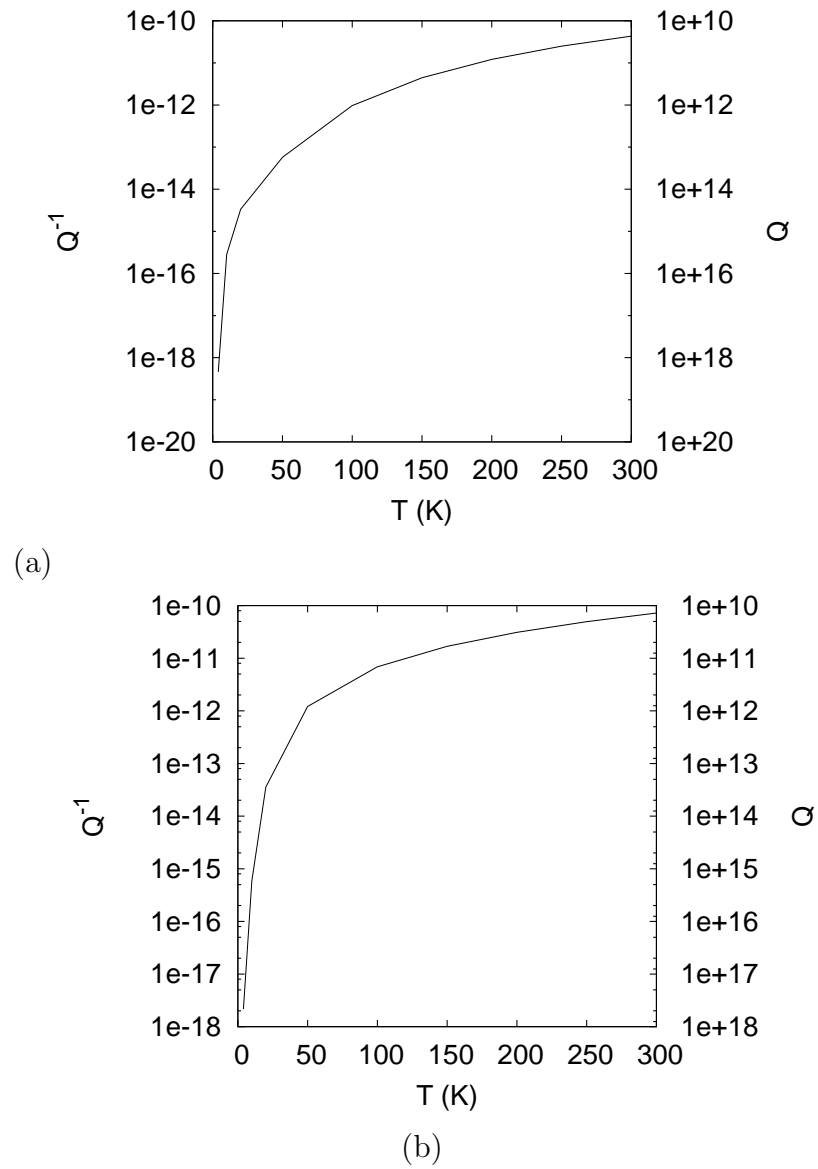


Figure 4.10: Q^{-1} and Q versus temperature for four-phonon processes in the Landau-Rümer limit for (a) a (12,0) nanotube and (b) an (18,0) nanotube.

the range 0.9 – 1.4 nm.

A previous study by Jiang *et al.* reports Q -factors of around 1000 at room temperature [13]. Because the results quoted in that work were obtained by a molecular dynamics simulation with the same interatomic potential, only phonon-phonon processes were possible and our results should be directly comparable. Although our results are an upper bound for the quality factor, the large discrepancy between this work and our results suggests the possibility of errors in the molecular dynamics simulation. One of the errors is that quantum mechanical effects are important at the temperatures considered in the study even though molecular dynamics calculations only simulate classical effects. This effect at the temperatures considered however only makes a difference of at most an order of magnitude. Other sources of this discrepancy may be due to possible errors in the molecular dynamics calculation such as the use of an unrealistically short nanotube of 3 nm and questions regarding the use of numerical thermostats. Further studies is required to resolve these issues.

Bibliography

- [1] V. Sazonova *et al.*, Nature **431**, 284 (2004).
- [2] P. Poncharal, Z. L. Wang, D. Ugarte, and W. A. de Heer, Science **283**, 1513 (1999).
- [3] S. T. Purcell, P. Vincent, C. Journet, and V. T. Binh, Phys. Rev. Lett. **89**, 276103 (2002).
- [4] A. Husain *et al.*, Appl. Phys. Lett. **83**, 1240 (2003).
- [5] X. Liu *et al.*, Physica B **316-317**, 393 (2002).
- [6] A. Akhiezer, J. Phys. USSR **21**, 1 (1939).
- [7] A. Landau and R. J., Sov. Phys. **11**, 18 (1937).
- [8] J. Hone, M. Whitney, C. Piskoti, and A. Zettl, Phys. Rev. B **59**, R2514 (1999).
- [9] Z. Yao, J.-S. Wang, B. Li, and G.-R. Liu, Phys. Rev. B **71**, 085417 (2005).
- [10] G. D. Mahan, *Many-Particle Physics* (Kluwer Academic/Plenum Publishers, New York, 2000).
- [11] J. M. Ziman, *Electrons and Phonons* (Oxford University Press, London, 1960), p. 145.
- [12] D. W. Brenner *et al.*, J. Phys.: Condens. Matter **14**, 783 (2002).
- [13] H. Jiang, M.-F. Yu, B. Liu, and Y. Huang, Phys. Rev. Lett. **93**, 185501 (2004).

Chapter 5

Modelling a Suspended Nanotube

5.1 Introduction

Vibrations of *one-dimensional* systems (i.e. systems with cross-sectional dimension much smaller than their length) suspended under the influence of a downward force have long been of interest in the context of such applications as beams, cables supporting suspension bridges and ship moorings [1, 2, 3]. Such systems display a wide range of behavior, depending on the amount of slack present in the system, the downward force, and the aspect ratio. Previous studies, which have largely been analytical, have been restricted to certain limiting cases of these parameters. Recently work on oscillating nanoscale systems, such as carbon nanotubes[4] and silicon nanowires[5], has opened the possibility of experimentally exploring such vibrations in entirely new regimes. In this chapter, we study numerically the oscillations of a one dimensional elastic system over an extensive range of both the slack and force parameters, providing insight into the physics which separates this parameter space into three distinct regimes of behavior.

The treatment below is entirely general with illustrative examples taken from parameters relevant to carbon nanotubes. Since their discovery in 1991 [6], nanotubes have found many applications in device technology due to their small size, robust structure and superior elastic properties [7, 8, 9, 10]. Many of these applications involve the use of nanotubes as mechanical oscillators, making theoretical understanding of the vibrational properties of nanotubes in various geometries of current interest[4, 11]. Recent experiments [12] have studied the behavior of the transverse vibrations of a suspended nanotube clamped at both ends, under the

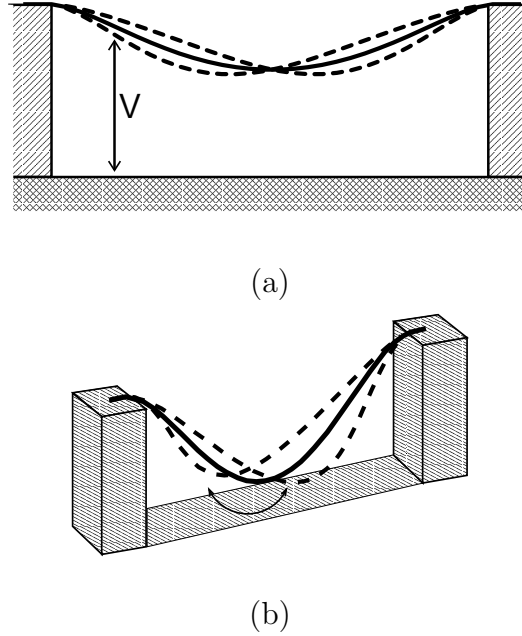


Figure 5.1: (a) suspended nanotube under the action of a gate voltage V , (b) *jump-rope* mode

action of a downward force, as sketched in Figure 5.1. These suspended nanotubes generally have around 1% *slack*, denoted in this chapter by s , which we define to be the ratio of the excess length of the tube to the distance between clamping points.

In Section 5.2, we introduce our methods for studying the frequencies of a general, one-dimensional system in the continuum description. In Section 5.3, we present a convenient set of dimensionless parameters that renders all of our discussions easily adaptable to any one-dimensional system. In Section 5.4, we present our numerical results and develop simple classical mechanical arguments that provides a better grasp of the physics involved. Section 5.5 is a comparison of our results against experimental data. Section 5.6 concludes this chapter with a summary.

5.2 Analytic model and computational techniques

The potential energy of a one-dimensional elastic continuum under a uniform downward force is

$$\mathcal{U} = \frac{1}{2} \int_0^L \left[Eu^2(l) + \frac{F}{R^2(l)} + fz(l) \right] dl \quad (5.1)$$

Here, l represents distance along the system of unstretched length L ; $u(l)$, $R(l)$ and $z(l)$ represent the local strain, radius of curvature and vertical displacement, respectively; E and F are the extensional and flexural rigidities; and f is the downward force per unit length. Equation (5.1) is accurate provided the strain u is small enough that the material is in its linear-response regime and the radius of curvature R is large compared with the diameter d . In addition, the length L must also be much greater than the diameter.

For single-walled nanotubes with diameters $d > 1$ nm, the rigidities we obtain using the second generation of the potential developed by Brenner *et al* [13] are, to within 0.5%,

$$\begin{aligned} E &= 1.09 \cdot d && (\text{TPa} \cdot \text{nm}^2) \\ F &= Ed^2/8 = 0.14 \cdot d^3 && (\text{TPa} \cdot \text{nm}^4), \end{aligned} \quad (5.2)$$

regardless of the chirality of the tube. (This insensitivity to chirality was found previously in Ref. [14] for E). In general, the deviations from these relations depend upon chirality. We note that essentially the same values of E and F can be obtained using the in-plane elastic modulus of graphite. For nanotubes, the linear response approximation used in Equation (5.1) for stretching is accurate to around 1% for strains less than 5%. The linear approximation for bending also breaks down as the nanotube approaches the local buckling (kink formation) instability [15], which for a 2 nm diameter tube happens at a radius of curvature

of about 0.03μ [15].

To evaluate the potential energy (Equation (5.1)), we begin with $\mathbf{r}(l)$, the *vector* location of the segment at position l from the end of the tube. The local strain is, then,

$$u(l) \equiv |\mathbf{r}'| - 1 \quad (5.3)$$

and inverse radius of curvature is

$$\frac{1}{R} \equiv \frac{|(1 - \hat{t}\hat{t}\cdot)\mathbf{r}''|}{|\mathbf{r}'|^2}, \quad (5.4)$$

where prime indicates differentiation with respect to l , and the unit tangent vector $\hat{t} \equiv \mathbf{r}' / |\mathbf{r}'|$.

For a given force and slack, we discretize $\mathbf{r}(l)$ along l with a number of points (typically 30) sufficient to render all plots shown below visually indistinguishable under increasing resolution. This discretization scheme is illustrated in Figure 5.2. The extensional and flexural terms of the energy in this discretized form are

$$\mathcal{U}_{\text{extension}} = \frac{1}{2} E \sum_{i=1}^N \frac{|\vec{r}_{i+1} - \vec{r}_i|^2}{\Delta l} \quad (5.5)$$

$$\mathcal{U}_{\text{flexure}} = \frac{1}{2} F \sum_{i=2}^{N-1} \frac{(|\vec{t}_i|^2 - \vec{t}_i \vec{t}_i \cdot) |\vec{d}_i|^2}{|\vec{t}_i|^2} \Delta l \quad (5.6)$$

where \vec{r}_i is the location of the i th sample point, $\vec{d}_i = \vec{r}_{i+1} + \vec{r}_{i-1} - 2\vec{r}_i$ is the finite-difference second derivative, $\vec{t}_i = \vec{r}_{i+1} - \vec{r}_{i-1}$ is the tangent vector at i and Δl is the initial separation between the discretized units. To find the equilibrium configuration of the system under the action of the external force, we then relax the system using a conjugate gradients algorithm with forces computed using finite differences. Finally, we compute the force constant matrix $K_{ij} \equiv \frac{\partial^2 \mathcal{U}}{\partial x_i \partial x_j}$ and diagonalize it to obtain frequencies ν while assigning a mass $\mu \Delta l$ to each discretized point, where μ is the mass per unit length of the system.

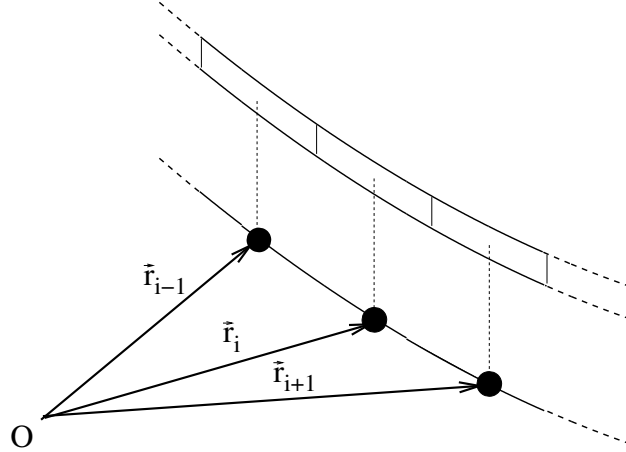


Figure 5.2: Discretization of the continuous nanotube into discrete *beads*. Each bead corresponds to one of the portions of equal length. The position, \vec{r}_i vectors of the beads, which the discrete form of the energy is written in terms of, are indicated with respect to a chosen origin, O .

5.3 Dimensionless parameters

For a one-dimensional system, slack s , length L and downward force per unit length f can be regarded as *external parameters* that can be changed independently. Mass density μ and rigidities E and F on the other hand, all depend on the cross-sectional geometry of the system and can therefore be considered *internal parameters*. To make our discussion applicable to a general one-dimensional system, we present our results in units scaled by appropriate combinations of these basic parameters. In addition, we give results in physical units for the concrete system of a nanotube of diameter 2 nm with length $L = 1.75 \mu\text{m}$. For frequency plots, we plot a dimensionless frequency $\tilde{\nu} \equiv \nu \sqrt{(\mu L^4 / F)}$ for a general case. In addition, we plot ν , specific to the nanotube example.

As a dimensionless measure of this force, we choose a *force control parameter* $\tilde{V} \equiv \sqrt{f L^3 / F}$, proportional to the square root of the force. In recent experiments

of our collaborators on suspended nanotubes[12], the external force was introduced via a gate voltage, as shown in Figure 5.4a. Such a voltage results in a force per unit length $f = \frac{1}{2} \frac{dc}{dz} V^2$. Here c is the capacitance per unit length of the nanotube taken to be that of a metallic cylinder,

$$c = \frac{4\pi\epsilon_0}{2\ln(z/d)}, \quad (5.7)$$

where ϵ_0 is the dielectric constant of vacuum and z is the distance between the wire and gate. For the concrete example of a $L=1.75\mu\text{m}$ nanotube with a diameter of 2nm, we take the tube to be suspended 500nm above the gate. In this case, a dimensionless parameter of $\tilde{V} = 10$ corresponds to a voltage of $\sim 4\text{V}$. As another example, a $100\mu\text{m}$ -long Si nanowire of 100nm diameter, with a z of $25\mu\text{m}$ would require a voltage of $\sim 60\text{V}$ to attain the same force control parameter \tilde{V} of ten. Moving to larger systems, a 0.6mm-diameter steel piano wire which is $\sim 2\text{m}$ long under the influence of gravity would have the same dimensionless parameter of $\tilde{V} = 10$.

5.4 Numerical results and discussion

Figures 5.3 and 5.4 display our primary results, both in dimensionless form and for the nanotube example, for the dependence of the vibrational frequency on slack and force.

Figure 5.3 shows the dependence of frequency on slack over the range of small slacks for zero force. The style of the curves indicate whether the mode is doubly-degenerate and odd (solid), out-of-plane and even (dashed) or in-plane and even (dotted). After the mode crossings shown with arrows in Figure 5.3, all curves remain flat up through a slack of 2%, the largest slack considered in this paper.

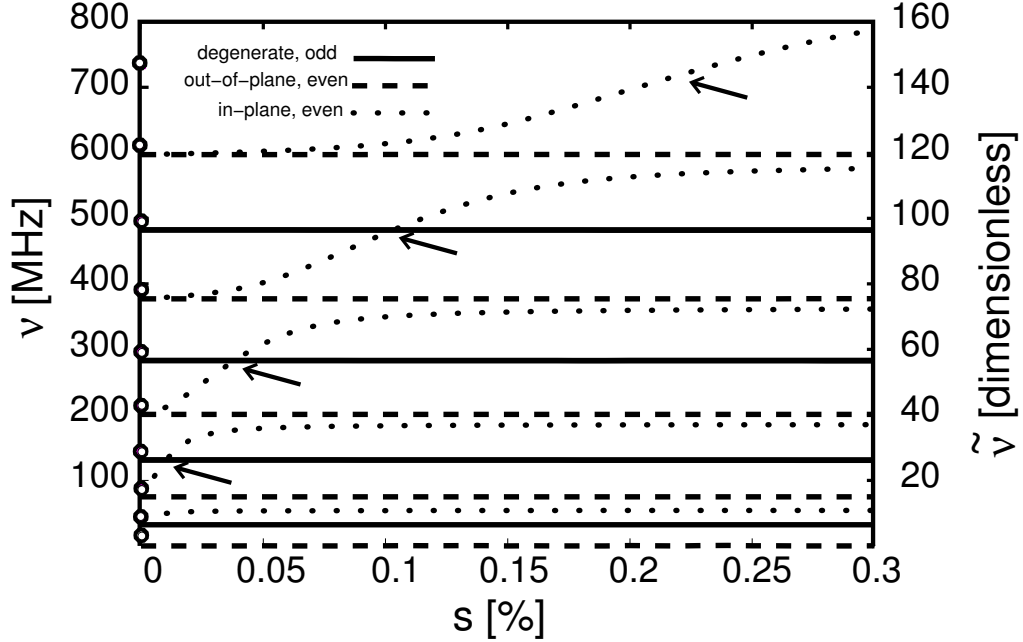
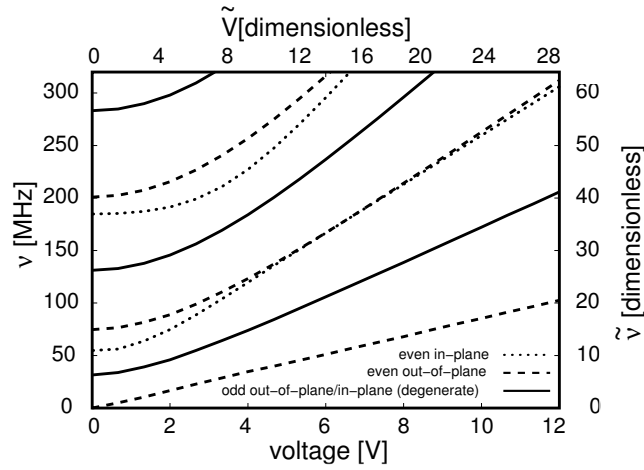


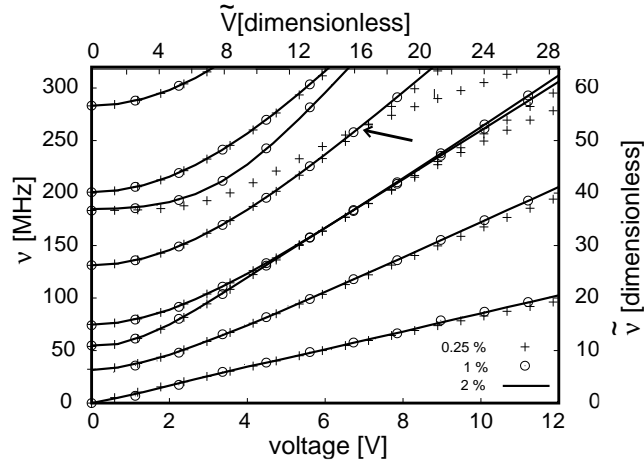
Figure 5.3: Frequency versus slack at zero force control parameter: classic solution for zero slack (points on vertical axis), numerical results for non-zero slack (curves). The dimensionless frequency $\tilde{\nu} = \nu \sqrt{\mu L^4 / F}$ applies to a general system. The modes are doubly-degenerate and odd (solid curves), out-of-plane and even (dashed curves) or in-plane and even (dotted curves). Arrows indicate mode crossings.

Figure 5.4 shows the dependence of the frequency on the force control parameter. Figure 5.4(a) shows the symmetry of the modes as in Figure 5.3 for a system of 1% slack. Figure 5.4(b) shows slacks of $s=0.25\%$, 1% and 2% with the horizontal axis scaled by $\sqrt[4]{s}$ which, for reasons described below, causes the curves to collapse upon each other for all but the smallest slack.

We find three simplifying limits for the physical behavior of the system as a function of slack s and force control parameter ν . In each such limit, a different term in the potential energy (Equation (5.1)) dominates with the other terms either being negligible or acting to enforce a constraint. Figure 5.5 shows these



(a)



(b)

Figure 5.4: (a) Dimensionless frequency versus force control parameter: in-plane modes (dashed curves), out-of-plane modes (dotted curves), degeneracy of in- and out-of- plane modes (solid curves). (b) Dimensionless frequency versus force control parameter scaled by fourth-root of slack ($\nu/\sqrt[4]{s/1\%}$) for three values of slack s : 0.25% ('+'), 1% (curves), 2% ('⊙'). Frequency in MHz and voltage in V refer to the nanotube example described in the text. The scaled frequency $\tilde{\nu} = \nu\sqrt{\mu L^4/F}$ and the force control parameter $\tilde{V} = \sqrt{fL^3/F}$ apply to a general system.

three regimes, which we term *buckled beam*, *hanging chain* and *hanging spring*.

5.4.1 Small V regime

For small external forces, the extensional rigidity acts as a constraint which keeps the tube length fixed. If the force is sufficiently small, the bending term in Equation (5.1) dominates the dynamics and the system acts like an *Euler-buckled beam*. This is a global buckling to relieve the strain, which can be described by a linear theory. It should not to be confused with local buckling that occurs at larger strains and causes the cross section of the material to collapse, such as kink formation in a nanotube [15].

The *in-plane* vibrations of buckled beams have been studied analytically, but only in the absence of an applied force and only under conditions of very small slack (under $\sim 0.07\%$ [2]). Our results extend this treatment to three dimensions and larger values of slack, probing at the same time the dependence on the downward force. In the absence of applied force all modes are doubly degenerate at zero slack with the frequencies of the classic unbuckled clamped beam [16], shown as circles on the vertical axis of Figure 5.3.

5.4.2 Intermediate V regime

When the force is large enough to overcome the bending term in Equation (5.1) but still too small to stretch the nanotube, the tube behaves as a *hanging chain* clamped at both ends, whose equilibrium profile forms the well-known *catenary*. In the small slack limit, the shape of the tube is parabolic as seen in Figure 5.8. with the equation

$$y(x) = \frac{4H}{W^2}x^2 - H \quad (5.8)$$

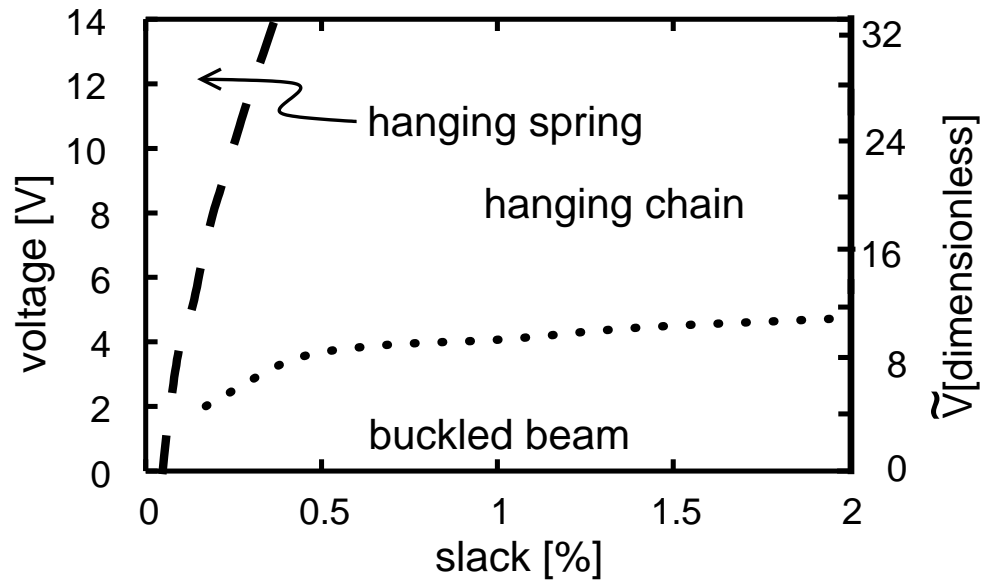


Figure 5.5: The three regimes in which nanotube behavior simplifies, as a function of voltage and slack. The dashed line between the “hanging spring” and “hanging chain” regimes is the crossing between the second even in-plane mode and the second odd in-plane mode. The dotted line separating the “buckled beam” regime from the “hanging chain” regime is the contour on which the derivative $\frac{d \log \omega}{d \log s}$ has a value of $-1/8$. The axis on the right shows the force control parameter, $\tilde{V} = \sqrt{fL^3/F}$

where x is the coordinate that runs along the horizontal and the vertical displacement, y is given as a function of x . The length L of the nanotube can be written in terms of the distance W between the clamping points by integrating the infinitesimal arc length element ds throughout this distance,

$$L = \int_{-W/2}^{W/2} ds = \int_{-W/2}^{W/2} \sqrt{1 + (dy/dx)^2} dx. \quad (5.9)$$

Assuming a small downward displacement and a large L , and using Equation (5.8) to obtain the derivative, we calculate Equation (5.9) to be

$$L \approx \int_{-W/2}^{W/2} \left[1 + \frac{1}{2} (dy/dx)^2 \right] dx = W + \frac{8H^2}{3W}. \quad (5.10)$$

With this result, slack s can be written as

$$s = \frac{L - W}{L} = \frac{8H^2}{3L^2}, \quad (5.11)$$

where we take $L \approx W$, which is a valid approximation for large L . Equation (5.11) allows us to eliminate H and write our results in terms of the fundamental parameters of the problem with

$$H = L\sqrt{3s/8}. \quad (5.12)$$

On the other hand, the magnitude T of the tension \vec{T} can be linked to the magnitude fL of the total downward force \vec{F} with

$$fL = 2T \sin \theta = \left. \frac{dy}{dx} \right|_{W/2} = \frac{4H}{L}, \quad (5.13)$$

where θ is the angle that \vec{T} makes with the clamps as shown in Figure 5.8. Combining Equation (5.12) and Equation (5.13), we arrive at the simple expression

$$T = \frac{fL}{\sqrt{24s}}. \quad (5.14)$$

The angular frequencies of transverse vibrations for a string under tension T is given by the well-known formula

$$\omega_n = \frac{n\pi}{L} \sqrt{T/\mu}, \quad (5.15)$$

where μ is the mass per unit length and n is an integer denoting mode index. Substituting Equation (5.14) and Equation (5.12) into Equation (5.15), we obtain the final result for the vibration frequencies of the nanotube in this regime.

$$\omega_n = n\pi \sqrt{\frac{f}{\mu L \sqrt{24s}}} \quad (5.16)$$

Since in this equation the frequency is proportional to $s^{-1/4}$, we scale the horizontal axis in Figure 5.4(b) by $\sqrt[4]{s}$, causing the curves for each slack value to collapse for small forces, although for 0.25% slack there is deviation in the higher modes, in particular in the mode indicated by the arrow. This simple result also explains the linear dependence of the frequencies on the voltage in this intermediate regime in Figure 5.3 as f is proportional to V^2 .

With the introduction of slack, the lowest out-of-plane mode, which we term “jump rope”, corresponds to rotation of the relaxed system about the clamping points, as illustrated in Figure 5.1b. Rotational symmetry requires that this mode have zero frequency in the absence of an external force. It therefore appears as a dashed line overlaying the slack axis of Figure 5.3. No such symmetry applies to other out-of-plane modes, whose frequencies drop slightly, and then remain essentially independent of slack.

In contrast to the out-of-plane modes, the in-plane modes are affected by a length-conservation constraint which changes with the amount of slack. For reasonably small slack, the odd modes (shown as solid lines) are unaffected by this constraint, since they conserve length by symmetry, and thus remain degenerate

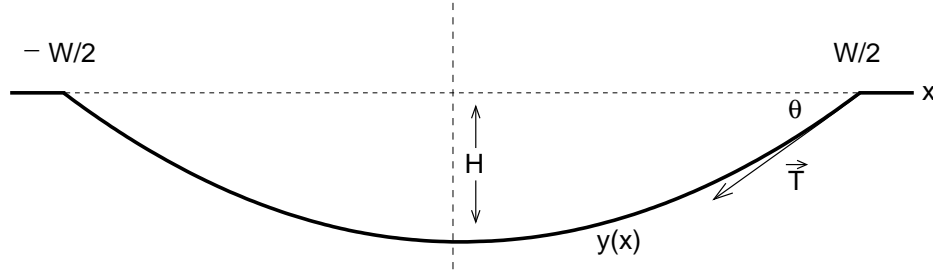


Figure 5.6: Nanotube in the *hanging chain* regime, forming a *catenary*. In this limit, it can be treated as a parabola with width W and depth H , with a tension T at angle θ

with their out-of-plane counterparts. The even modes (shown as dotted lines), in order to conserve the tube length, acquire two extra nodes as slack is introduced, leading to a mode crossing between the even and odd modes (shown with arrows in Figure 5.3).

5.4.3 Large V regime

For a given force, as the slack decreases, the tension increases and eventually the tube begins to stretch and departs from the hanging chain regime. This avoids the infinite frequency at very small slack which is Equation (5.16) predicts. This effect is responsible for the deviation from linear behavior of the tube with 0.25% slack in Figure 5.4, in contrast to the tubes with 1% and 2% slack.

In the large force, small slack regime, the extensional term in Equation (5.1) can no longer be treated as a constraint, as the tube begins to stretch. The nanotube then behaves as a *hanging spring* clamped at both ends. The frequency in this regime can be derived in a manner similar to that in the hanging chain regime; namely by taking the shape of the nanotube to be parabolic and the tension to

be constant throughout the tube. However, in the case of the hanging spring, the tension is proportional to the change in length of the tube.

In this limit, we again make the assumption that the nanotube profile is given by a parabola,

$$y = A [x^2 - (W/2)^2], \quad (5.17)$$

where this time the unknown amplitude A is a variational parameter. The symbols are the same as the treatment for the catenary and we still refer to Figure 5.8.

The total energy of the nanotube given this profile is

$$\mathcal{U} = \int_{-W/2}^{W/2} \left[\frac{1}{8} E \left(\frac{dy}{dx} \right)^4 + fy \right] dx = \frac{EA^4W^5}{40} - \frac{fAW^3}{6}, \quad (5.18)$$

where the bending energy is omitted since it is no longer significant in this limit. From Equation (5.18), we immediately see that the energy reaches a minimum for

$$A = \left(\frac{5f}{3EW^2} \right)^{1/3}. \quad (5.19)$$

In a stretched spring, the tension is proportional to the excess length ΔL . More precisely,

$$T = E\Delta L/L. \quad (5.20)$$

This excess length can be calculated by employing the same method of integrating the arc length element as in Equation (5.9),

$$\Delta L \approx \int_{-W/2}^{W/2} \left(\frac{dy}{dx} \right)^2 dx = \frac{W^3A^2}{6}, \quad (5.21)$$

where the last equality was obtained using the minimizing value of A from Equation (5.19). With Equation (5.21) and Equation (5.19) the tension in terms of the fundamental constants of the problem is

$$T = f^{2/3} \frac{W}{6} \left(\frac{25EW}{9} \right)^{1/3}. \quad (5.22)$$

Finally, we find the frequencies in this limit by substituting Equation (5.22) into Equation (5.15) to be

$$\omega_n = n\pi \left(\frac{5}{3}\right)^{1/3} \sqrt{\frac{(EL)^{1/3}}{6\mu L}} f^{1/3}. \quad (5.23)$$

We observe that the frequency is independent of slack, because as the tube is stretched the original amount of slack in the nanotube becomes insignificant. However, we expect the point of onset of the hanging spring regime to be independent of slack. Our results presented in Figure 5.3 indicates that within the experimentally accessible voltage range, the hanging spring regime appears only for very small slack.

In the buckled beam and hanging chain regimes, the length conservation constraint in a slack tube forces the first even in-plane mode to have two nodes. In contrast, in the hanging spring regime there is no length conservation constraint, and consequently, the lowest frequency in-plane mode has no nodes. As the transition between these regimes occurs, there is a mode crossing between the even and odd in-plane modes, shown with an arrow in Figure 5.4 in the curve for 0.25% slack. The crossing between the second even in-plane mode and the second odd in-plane mode is shown as the dashed curve in Figure 5.5 which separates the hanging spring regime from the hanging chain regime.

5.5 Comparison with experiment

In this section, we compare our results with experimental data provided in [12] and suggest a possible reason for the discrepancy that we observe at small frequencies.

The qualitative agreement between our results and experiment is evident from Figure 5.7. For all modes observed in the experiment, in the small f region, the

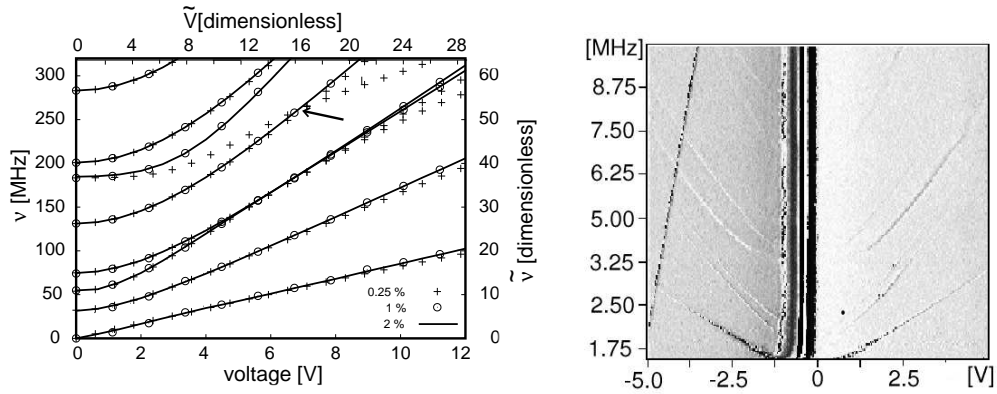


Figure 5.7: Comparison of numerical results to experimental data. We reproduce here the ν versus V plot (left) from Figure 5.4 for ease of comparison to experimental results from [12] (right)

frequencies go quadratically with V as predicted by our numerical results. The agreement also extends itself to the intermediate f region, where the frequencies are linear in V . The larger V region is beyond the scope of the experiment which is also a result that we predict in Figure 5.3 for all but the smallest slack.

Even though the qualitative agreement is good, we find that the numerical frequencies are significantly higher than the experimental frequencies. In particular, in the theoretical plot, there are no modes at $V = 0$ up to a frequency of ~ 33 MHz. However, in the experiment, we find several modes whose frequencies are between 0 and 10 MHz.

Among the several possible causes of this discrepancy, two examples would be excess mass on the nanotubes from other materials remaining from fabrication stages and also underestimation of the tube length, which would both lower the frequencies. However, simple scaling arguments show that these are not the likely causes of such a large decrease in frequencies. Another likely cause, whose effects are less controlled is a possible asymmetry in the clamping at the end of the

tubes. We have so far assumed the clamps to be exactly parallel to the plane of the nanotube and to each other, which is a very unlikely configuration in the experiments.

To study the effects of asymmetric clamps, we recalculate frequencies of the nanotube by preparing the tube in a configuration as shown in the left hand panel of Figure 5.5. We study two possible cases, one in which the two clamps both point down at angles θ_1 and θ_2 and one where one of the clamps point down while one points up. For each case, we study about one hundred $\{\theta_1, \theta_2\}$ pairs chosen randomly from a normal distribution of width 5° . Given such a pair, we relax the nanotube with the clamps fixed at their asymmetric angles and calculate the frequencies as described in Section 5.2.

We present results for the two cases in the form of histograms in Figure 5.5. On the top panel, we show the results for the case when the clamps both point along the external force and on the bottom panel, we show results for the case when the clamps point in the opposite directions. In both cases, we clearly see that the asymmetry does indeed introduce smaller frequencies into the gap between the first two modes of the symmetric case in an almost continuous range even for our relatively small sample set. We conclude, then, that asymmetry in the clamps can indeed be a likely cause for the discrepancy between our numerical results and the experiment.

5.6 Conclusion

We have studied numerically and analytically, as a function of both the amount of slack and applied force, the transverse vibration frequencies of one dimensional suspended systems clamped at both ends. Our results are applicable when the length

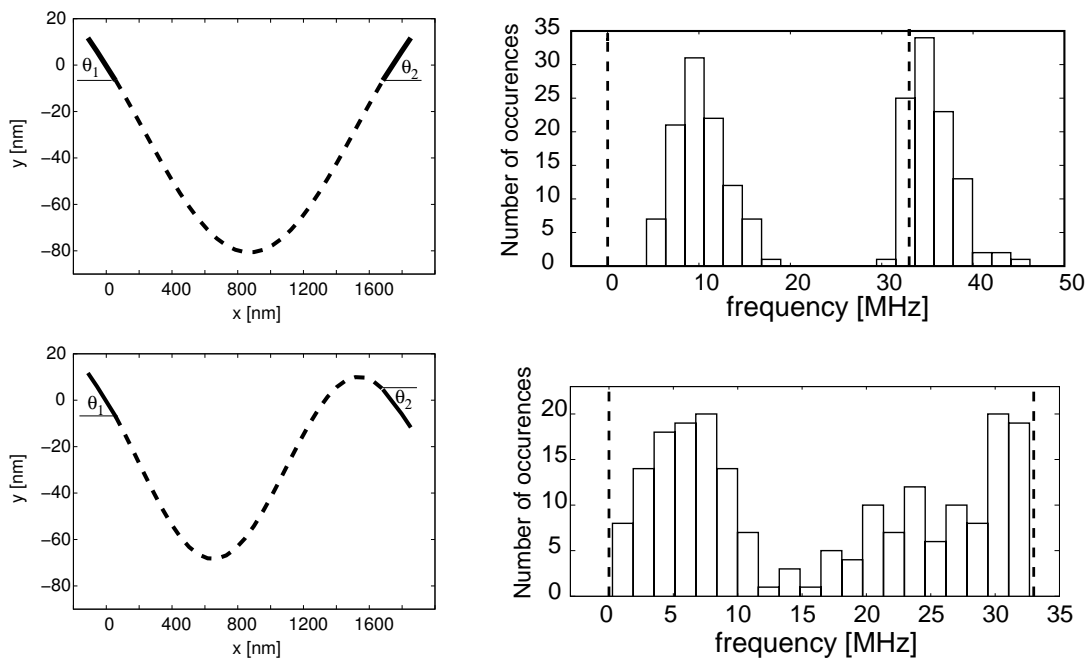


Figure 5.8: Histograms for the two lowest frequencies in the presence of asymmetry in clamping. The plots show distributions of the two lowest frequencies of the nanotube dispersion relation for ~ 100 calculations. The results in the top plot were obtained by constraining the clamps to point in the same direction, whereas the results in the bottom plot were obtained for clamps pointing in different directions. On the left hand of this figure, we show the relaxed profiles from two example runs corresponding to these situations. Note that the vertical coordinate of the profiles has a different scale than the horizontal coordinate for ease of vision.

and radius of curvature are both much larger than the cross-sectional diameter and the strain is small enough that nonlinear elastic effects may be ignored. We have chosen as a concrete application to focus on suspended nanotubes under the influence of a gate voltage which have recently been studied experimentally [12]. We find three regimes in which the behavior simplifies and can be understood using approximate analytic solutions. This understanding is important in characterizing and designing nanoresonators where it can prove difficult to control or measure parameters such as slack. The hanging chain regime is particularly suitable for tuning and characterizing nano-oscillators, since Equation (5.16), which governs the frequency in this regime, remains valid independently of imperfections affecting the boundary conditions at the clamps.

Comparison of our results with experiments indicate a discrepancy in the low-lying branches. As a possible explanation, we studied the effect of the asymmetry in the clamps and found that such asymmetry may indeed cause lowering of the frequencies.

Finally, we studied the possibility of energy loss due to transmission into clamps. Within the framework of the simple model studied, we find the clamps to cause no energy loss if the driven mode is the acoustic transverse mode.

Bibliography

- [1] H. M. Irvine and T. K. Caughey, Proc. R. Soc. London, Ser. A **341**, 299 (1974).
- [2] A. H. Nayfeh and W. Kreider, AIAA Journal **33**, 1121 (1995).
- [3] N. Kitney and D. T. Brown, Journal of Offshore Mechanics and Arctic Engineering **123**, 1 (2001).
- [4] S. Sapmaz, Y. M. Blanter, L. Gurevich, and H. S. J. van der Zant, PRB **67**, 235414 (2003).
- [5] D. W. Carr *et al.*, Appl. Phys. Lett. **75**, 920 (1999).
- [6] S. Iijima, Nature **354**, 56 (1991).
- [7] R. M. D. Stevens *et al.*, Nanotechnology **11**, 1 (2000).
- [8] K. Keren *et al.*, Science **302**, 1380 (2003).
- [9] T. Shimada *et al.*, Appl. Phys. Lett. **84**, 2412 (2004).
- [10] W. Yang *et al.*, Nature Materials **1**, 253 (2002).
- [11] M. Dequesnes, S. V. Rotkin, and N. R. Aluru, Nanotechnology **13**, 120 (2002).
- [12] V. Sazonova *et al.*, Nature **431**, 284 (2004).
- [13] D. W. Brenner *et al.*, J. Phys.: Condens. Matter **14**, 783 (2002).
- [14] J. P. Lu, Phys. Rev. Lett. **79**, 1297 (1997).
- [15] B. I. Yakobson, C. J. Brabec, and J. Bernholc, PRL **76**, 2511 (1996).
- [16] L. D. Landau and E. M. Lifshitz, *Theory of Elasticity* (Pergamon Press, New York, 1970), p. 116.